

UNIVERSITÉ DU QUÉBEC À MONTRÉAL

RELATIVE IMPORTANCE OF CONTACT NUCLEATION AND ITS ALTERATION
BY SULFURIC ACID IN THE MICROSTRUCTURE OF ARCTIC CLOUDS

THESIS
PRESENTED
AS PARTIAL REQUIERMENT
OF THE MASTERS OF ATMOSPHERE SCIENCE

BY
NILOOFAR SOKHANDAN ASL

AUGUST 2013

UNIVERSITÉ DU QUÉBEC À MONTRÉAL
Service des bibliothèques

Avertissement

La diffusion de ce mémoire se fait dans le respect des droits de son auteur, qui a signé le formulaire *Autorisation de reproduire et de diffuser un travail de recherche de cycles supérieurs* (SDU-522 – Rév.01-2006). Cette autorisation stipule que «conformément à l'article 11 du Règlement no 8 des études de cycles supérieurs, [l'auteur] concède à l'Université du Québec à Montréal une licence non exclusive d'utilisation et de publication de la totalité ou d'une partie importante de [son] travail de recherche pour des fins pédagogiques et non commerciales. Plus précisément, [l'auteur] autorise l'Université du Québec à Montréal à reproduire, diffuser, prêter, distribuer ou vendre des copies de [son] travail de recherche à des fins non commerciales sur quelque support que ce soit, y compris l'Internet. Cette licence et cette autorisation n'entraînent pas une renonciation de [la] part [de l'auteur] à [ses] droits moraux ni à [ses] droits de propriété intellectuelle. Sauf entente contraire, [l'auteur] conserve la liberté de diffuser et de commercialiser ou non ce travail dont [il] possède un exemplaire.»

UNIVERSITÉ DU QUÉBEC À MONTRÉAL

IMPORTANCE RELATIVE DE NUCLÉATION PAR CONTACT ET DE SON
ALTÉRATION PAR L'ACIDE SULFURIQUE DANS LA MICROSTRUCTURE DES
NUAGES ARCTIQUES

MÉMOIRE
PRÉSENTÉ
COMME EXIGENCE PARTIELLE
DE LA MAÎTRISE EN SCIENCE DE L'ATMOSPHÈRE

PAR
NILOOFAR SOKHANDAN ASL

AOÛT 2013

REMERCIEMENTS

Arrivée à la fin de la rédaction de ce mémoire, je voudrais témoigner toute ma reconnaissance et ma gratitude à tous ceux qui m'ont aidé à sa réalisation par leur enseignement, leur soutien et leurs conseils. Je tiens dans un premier temps à adresser mes remerciements à mon directeur de recherche, Professeur Eric Girard, pour m'avoir accueilli dans son équipe. Sa patience, sa disponibilité, son aide ainsi que son soutien constant tout au long de mon cheminement a grandement contribué à effectuer ce travail. Je suis également reconnaissante de l'appui financier qu'il m'a offert lors de ma maîtrise. Mes remerciements sont aussi adressés au Professeur René Laprise, directeur des programmes d'études en sciences de l'atmosphère, pour son aide, sa gentillesse et son soutien tout au long de ces années. J'adresse une pensée particulière à Katja Winger, agente de recherche et de planification, qui a su m'enseigner toute la complexité du modèle GEMCLIM avec patience et enthousiasme. Je tiens également à exprimer mes gratitudes sincères à Guillaume Dueymes, agent de recherches du centre ESCER, qui m'a apporté une aide précieuse durant ma démarche. De plus, je voudrais remercier la contribution de Dr. Ping Du pour m'avoir épaulé lors de la réalisation des simulations numériques. Sa patience et sa disponibilité ont été grandement appréciées. Je remercie pareillement à Nadjat Labassi, analyste informatique, et à George Huard, technicien en informatique, pour leur aide concernant les ressources informatiques. J'apprécie leur bonne volonté pour répondre patiemment à mes nombreuses questions. De chaleureux remerciements vont à ma famille notamment à ma sœur, Negin, qui m'ont toujours encouragé et donné leur soutien moral. Je souligne ma gratitude à mes grands amis, Hanif et Fatemeh, qui m'ont apporté leur support moral et intellectuel tout au long de ma démarche. Je tiens à remercier particulièrement Hanif dont ses conseils rigoureux et son sens critique m'ont permis d'aller jusqu'au bout de mes objectifs. Je voudrais exprimer ma reconnaissance envers mes collègues au bureau qui m'ont aidé à réaliser divers travaux pendant ma

recherche. Je remercie finalement tous ceux qui ont manifesté de la bonne volonté envers moi au cours de mon projet.

TABLE DES MATIÈRES

LISTE DES FIGURES	viii
LISTE DES TABLEAUX.....	xiv
LISTE DES ACRONYMES	xv
LISTE DES SYMBOLES.....	xvi
RÉSUMÉ	xix
ABSTRACT.....	xxi
CHAPTER I	
INTRODUCTION	1
CHAPTER II	
METHODOLOGY	7
2.1 Description of the model GEM-LAM	7
2.1.1 Correlated-k radiation Scheme.....	8
2.1.2 Microphysics scheme of Milbrandt and Yau	9
2.2 Experiment configuration	16
2.2.1 Simulation domain.....	16
2.2.2 Initial conditions at the boundaries	17
2.2.3 Ensemble techniques and statistical analysis.....	18
2.3 Statistical analysis of the results (Student's t-test).....	21
2.4 Sensitivity study	22
CHAPTER III	
RESULTS.....	24
3.1 Model validation	24
3.2 Comparison of the aerosol scenarios.....	28
3.2.1 Comparison of AC1 and NAT1 (Pair 1).....	28
3.2.2 Comparison of AC3 and NAT1 (Pair 2).....	37
3.2.3 Comparison of NAT1 and NAT2 (Pair 3)	47

3.2.4 Comparison of AC1 and AC2 (Pair 4).....	57
3.2.5 Comparison of AC2 and NAT2 (Pair 5).....	65
3.2.6 Comparison of AC3 and NAT3 (Pair 6).....	75
DISCUSSION AND CONCLUSIONS.....	85
APPENDIX A	
The difference of geopotential height at 500 hPa, MSLP and temperature at 850 hPa between the ECMWF analysis and the model output averaged over January 2007 for aerosol scenarios NAT2, NAT3, AC1, AC2 and AC3	93
APPENDIX B	
B.1 Student t-test.....	97
B.2 Hypothesis test and determining significant area.....	98
APPENDIX C	
Student t table	102
APPENDIX D	
Maps of significant zones for temperature anomaly, relative humidity with respect to ice anomaly, ice water content anomaly, liquid water content anomaly, ice crystal concentration anomaly, liquid drop concentration anomaly and cloud forcing at the TOA for all six pairs of study.....	103
RÉFÉRENCES	114

LISTE DES FIGURES

Figures	Page
2.1 Domain of integration by GEMCLIM model, including dominant sources of anthropogenic sulfate in winter.	17
3.1 The differences of (a) geopotential height at 500 hPa (dam), (b) MSLP (hPa), (c) temperature (°C) at 850 hPa between the observations from ECMWF and GEMCLIM simulations averaged over January 2007 for aerosol scenarios NAT1.	25
3.2 The MSLP from ECMWF analysis averaged over January 2007.....	28
3.3 Vertical profiles of cloud (a) ice water content ($\times 10^{-3}$ g/kg) and (b) ice crystal number concentration ($\times 10^4$ 1/m ³) for aerosol scenarios NAT1 and AC1 averaged over time and spatially averaged over a mask delimited by sea ice boundaries.....	29
3.4 Vertical profiles of cloud (a) liquid water content ($\times 10^{-3}$ g/kg) and (b) liquid drop number concentration ($\times 10^5$ 1/m ³) for aerosol scenarios NAT1 and AC1 averaged over time and spatially averaged over a mask delimited by sea ice boundaries.	30
3.5 January mean (a) liquid water path anomaly ($\times 10^{-2}$ mm) and (b) ice water path anomaly ($\times 10^{-2}$ mm) in the Arctic when the anomaly is defined as the difference between AC1 and NAT1 (AC1-NAT1).	31
3.6 January 2007 mean RH _i (%) (a) vertical profile averaged over a mask delimited by sea ice boundaries and (b) anomaly at 850 hPa for aerosol scenarios NAT1 and AC1 when the anomaly is defined as the difference between AC1 and NAT1 (AC1-NAT1).	32
3.7 Mean January 2007 cloud forcing anomaly ($\times 10$ W/m ²) at (a) the surface and at (b) the TOA over the Arctic when the anomaly is defined as the difference between AC1 and NAT1 (AC1-NAT1).	33
3.8 Pair 1 scatter plot of the daily mean cloud forcing anomaly (W/m ²) of January 2007 at TOA as a function of daily mean vertically integrated (a) liquid water path anomaly (Kg/m ²) and (b) ice water path anomaly (Kg/m ²) averaged over the sub-domain delimited by sea ice when the anomaly is defined as the difference between AC1 and NAT1 (AC1-NAT1).....	34
3.9 January 2007 mean temperature (°C) (a)vertical profiles (b) anomaly at 850 hPa averaged over a mask delimited by sea ice boundaries for aerosol scenarios NAT1 and AC1 when the anomaly is defined as the difference between AC1 and NAT1 (AC1-NAT1).	34

3.10 January daily mean of (a,c) ice crystal number concentration ($1/m^3$) and water drop concentration ($1/m^3$) anomalies as a function of RH_i (averaged over 5% intervals) and (b,d) temperature (averaged over 5 K intervals) anomalies spatially averaged over a mask delimited by sea ice boundaries when the anomaly is defined as the difference between AC1 and NAT1 (AC1-NAT1).....	39
3.11 Vertical profiles of cloud (a) ice water content ($\times 10^{-3}$ g/kg) and (b) ice crystal number concentration ($\times 10^4$ $1/m^3$) for aerosol scenarios NAT1 and AC3 averaged over time and spatially averaged over a mask delimited by sea ice boundaries.....	39
3.12 January a) daily mean of ice crystal number concentration ($\times 10^4$ $1/m^3$) and (b) mean vertical profiles of the mean RH_i (as a function of RH_i averaged over time and spatially averaged over a mask delimited by sea ice boundaries for NAT1 and AC3 while the horizontal bars show the RH_i standard deviation at each pressure level and vertical bars show the ice crystal number concentration standard deviation at related RH_i values in the troposphere.....	40
3.13 Vertical profiles of cloud (a) liquid water content ($\times 10^{-4}$ g/kg) and (b) liquid drop number concentration ($\times 10^4$ $1/m^3$) for aerosol scenarios NAT1 and AC3 averaged over time and spatially averaged over a mask delimited by sea ice boundaries.....	41
3.14 January mean (a) liquid water path anomaly ($\times 10^{-2}$ mm) and (b) ice water path anomaly ($\times 10^{-2}$ mm) in the Arctic when the anomaly is defined as the difference between AC3 and NAT1 (AC3-NAT1).....	42
3.15 January 2007 cloud forcing anomaly ($\times 10$ W/m^2) at (a) the TOA and (b) the surface for the pair 2 when the anomaly is defined as the difference between AC3 and NAT1 (AC3-NAT1).....	44
3.16 Pair 2 scatter plot of the daily mean cloud forcing anomaly (W/m^2) of January 2007 at TOA as a function of daily mean vertically integrated (a) liquid water path anomaly ($\times 10^{-4}$ Kg/m^2) and (b) ice water path anomaly ($\times 10^{-3}$ Kg/m^2) averaged over the sub-domain delimited by sea ice when the anomaly is defined as the difference between AC3 and NAT1 (AC3-NAT1).....	45
3.17 Mean January temperature anomaly over the Arctic at 850 hPa when the anomaly is defined as the difference between AC3 and NAT1 (AC3- NAT1).....	46
3.18 January 2007 mean temperature ($^{\circ}C$) vertical profiles averaged over a mask delimited by sea ice boundaries for aerosol scenarios NAT1 and AC3.....	46
3.19 Vertical profiles of cloud (a) ice water content ($\times 10^{-3}$ g/kg) and (b) ice crystal number concentration ($\times 10^4$ $1/m^3$) for aerosol scenarios NAT1	

and NAT2 averaged over time and spatially averaged over a mask delimited by sea ice boundaries.....	48
3.20 Vertical profiles of the mean relative humidity with respect to ice (%) with associated standard deviations (horizontal bars) for aerosol scenarios NAT1 and NAT2 averaged over time and spatially averaged over a mask delimited by sea ice boundaries.	48
3.21 Vertical profiles of (a) cloud liquid water content ($\times 10^{-4}$ g/kg) and (b) liquid drop number concentration ($\times 10^4$ 1/m ³) for aerosol scenarios NAT2 and NAT1 averaged over time and spatially averaged over a mask delimited by sea ice boundaries.	49
3.22 January mean (a) liquid water path anomaly ($\times 10^{-2}$ mm) and (b) ice water path anomaly ($\times 10^{-2}$ mm) in the Arctic when the anomaly is defined as the difference between NAT1 and NAT2 (NAT1- NAT2).....	51
3.23 January daily mean (a) relative humidity with respect to ice (%) (b) ice crystal number concentration ($\times 10^4$ 1/m ³) (c) liquid water drop concentration ($\times 10^5$ 1/m ³) with temperature averaged over 5 K intervals for aerosol scenarios NAT1 and NAT2 averaged over time and spatially averaged over a mask delimited by sea ice boundaries.	52
3.24 Mean January 2007 cloud forcing anomaly (W/m ²) at (a) the surface and at (b) the TOA over the Arctic when the anomaly is defined as the difference between NAT1 and NAT2 (NAT1- NAT2).....	54
3.25 Pair 3 scatter plot of the daily mean cloud forcing anomaly of January 2007 at TOA and at the surface (W/m ²) as a function of daily mean vertically integrated (a,c) liquid water path anomaly ($\times 10^{-4}$ Kg/m ²) and (b,d) ice water path anomaly (Kg/m ²) averaged over the sub-domain delimited by sea ice when the anomaly is defined as the difference between NAT1 and NAT2 (NAT1- NAT2).	55
3.26 mean January temperature anomaly over the Arctic at 850 hPa when the anomaly is defined as the difference between NAT1 and NAT2 (NAT1- NAT2).	56
3.27 January 2007 mean temperature (°C) vertical profiles averaged over a mask delimited by sea ice boundaries for aerosol scenarios NAT1 and NAT2.....	57
3.28 Vertical profiles of cloud ice water (a) content ($\times 10^{-3}$ g/kg) and (b) ice crystal number concentration ($\times 10^3$ 1/m ³) for aerosol scenarios AC1 and AC2 averaged over time and spatially averaged over a mask delimited by sea ice boundaries.....	58
3.29 Vertical profile of the mean relative humidity with respect to ice (%) for aerosol scenarios AC1 and AC2 averaged over time and spatially averaged over a mask delimited by sea ice boundaries.....	59

3.30 Vertical profiles of cloud liquid water (a) content ($\times 10^{-3}$ g/kg) and (b) liquid drop number concentration ($\times 10^5$ $1/m^3$) for aerosol scenarios AC1 and AC2 averaged over time and spatially averaged over a mask delimited by sea ice boundaries.....	60
3.31 January mean (a) liquid water path anomaly ($\times 10^{-2}$ mm) and (b) ice water path anomaly ($\times 10^{-2}$ mm) in the Arctic when the anomaly is defined as the difference between AC1 and AC2 (AC1-AC2).	61
3.32 Mean January 2007 cloud forcing anomaly ($\times 10$ W/m ²) at (a) the surface and at (b) TOA over the Arctic when the anomaly is defined as the difference between AC1 and AC2 (AC1-AC2).....	62
3.33 Mean January temperature anomaly over the Arctic at 850 hPa when the anomaly is defined as the difference between AC1 and AC2 (AC1- AC2).....	63
3.34 Daily mean CRF anomaly at the TOA as a function of the daily mean temperature anomaly for each grid point inside the mask delimited by sea ice boundaries for the (a) pair 4 and (b) pair 3 when the anomaly is defined as the difference between AC1 and AC2 (AC1- AC2).	63
3.35 Pair 4 scatter plot of the daily mean cloud forcing anomaly of January 2007 at TOA and at the surface (W/m ²) as a function of daily mean vertically integrated (a,c) liquid water path anomaly ($\times 10^{-3}$ Kg/m ²) and (b,d) ice water path anomaly ($\times 10^{-3}$ Kg/m ²) averaged over the sub-domain delimited by sea ice when the anomaly is defined as the difference between AC1 and AC2 (AC1-AC2).	64
3.36 January 2007 mean temperature ($^{\circ}$ C) vertical averaged over a mask delimited by sea ice boundaries for aerosol scenarios AC2 and AC1.	65
3.37 Vertical profiles of cloud (a) ice water content ($\times 10^{-3}$ g/kg) and (b) ice crystal number concentration ($\times 10^4$ $1/m^3$) for aerosol scenarios NAT2, AC2 (solid lines), and NAT1, AC1 (dotted lines) averaged over time and spatially averaged over a mask delimited by sea ice boundaries. ...	66
3.38 Vertical profiles of cloud (a) liquid water content ($\times 10^{-3}$ g/kg) and (b) liquid drop number concentration ($\times 10^5$ $1/m^3$) for aerosol scenarios NAT2, AC2 (solid lines), and NAT1, AC1 (dotted lines) averaged over time and spatially averaged over a mask delimited by sea ice boundaries.....	68
3.39 Vertical profile of the mean relative humidity with respect to ice (%) for aerosol scenarios NAT2 and AC2 averaged over time and spatially averaged over a mask delimited by sea ice boundaries.	69
3.40 January mean (a) liquid water path anomaly ($\times 10^{-2}$ mm) and (b) ice water path anomaly ($\times 10^{-2}$ mm) in the Arctic when the anomaly is defined as the difference between AC2 and NAT2 (AC2-NAT2).	70

3.41 Mean January 2007 cloud forcing anomaly ($\times 10 \text{ W/m}^2$) at (a) the surface and at (b) TOA over the Arctic when the anomaly is defined as the difference between AC2 and NAT2 (AC2-NAT2).	72
3.42 Pair 5 scatter plot of the daily mean cloud forcing anomaly of January 2007 at TOA as a function of daily mean (a) liquid water path anomaly (Kg/m^2) and (b) ice water path anomaly ($\times 10^{-3} \text{ Kg/m}^2$) averaged over the sub-domain delimited by sea ice when the anomaly is defined as the difference between AC2 and NAT2 (AC2-NAT2).	73
3.43 Mean January temperature anomaly over the Arctic at 850 hPa when the anomaly is defined as the difference between AC2 and NAT2 (AC2- NAT2).	74
3.44 Vertical profile of the mean temperature ($^{\circ}\text{C}$) for aerosol scenarios NAT2 and AC2 averaged over time and spatially averaged over a mask delimited by sea ice boundaries.	74
3.45 Vertical profiles of cloud ice (a) content ($\times 10^{-3} \text{ g/kg}$) and (b) ice crystal number concentration ($\times 10^4 \text{ 1/m}^3$) for aerosol scenarios AC3, NAT3 averaged over time and spatially averaged over a mask delimited by sea ice boundaries.	76
3.46 Vertical profile of the mean relative humidity with respect to ice (%) for aerosol scenarios NAT3 and AC3 averaged over time and spatially averaged over a mask delimited by sea ice boundaries.	77
3.47 January daily mean of ice crystal number concentration (1/m^3) anomaly as a function of RH_i (averaged over 5% intervals) and spatially averaged over the sea-ice mask with the related standard deviation (vertical bars) when the anomaly is defined as the difference between AC3 and NAT3 (AC3-NAT3).	77
3.48 Vertical profiles of cloud liquid water (a) content ($\times 10^{-5} \text{ g/kg}$) and (b) liquid drop number concentration ($\times 10^4 \text{ 1/m}^3$) for AC3 and NAT3 aerosol scenarios averaged over time and spatially averaged over a mask delimited by sea ice boundaries.	78
3.49 January mean (a) liquid water path anomaly ($\times 10^{-2} \text{ mm}$) and (b) ice water path anomaly ($\times 10^{-2} \text{ mm}$) in the Arctic when the anomaly is defined as the difference between AC3 and NAT3 (AC3-NAT3).	80
3.50 Mean January 2007 cloud forcing anomaly ($\times 10 \text{ W/m}^2$) at (a) the surface and at (b) the TOA over the Arctic when the anomaly is defined as the difference between AC3 and NAT3 (AC3-NAT3).	82
3.51 Pair 6 scatter plot of the daily mean cloud forcing anomaly of January 2007 at TOA as a function of daily mean vertically integrated (a) liquid water path anomaly ($\times 10^{-4} \text{ Kg/m}^2$) and (b) ice water path anomaly ($\times 10^{-3} \text{ Kg/m}^2$) averaged over the sub-domain delimited by sea ice when the anomaly is defined as the difference between AC3 and NAT3 (AC3-NAT3).	83

3.52 Mean January temperature anomaly over the Arctic at 850 hPa when the anomaly is defined as the difference between AC3 and NAT3 (AC3- NAT3).....	84
3.53 January 2007 mean temperature ($^{\circ}\text{C}$) vertical profiles averaged over a mask delimited by sea ice boundaries for aerosol scenarios NAT3 and AC3.	84
A.1 The difference of geopotential height at 500 hPa between the ECMWF analysis and the model output averaged over January 2007 for aerosol scenarios (a) NAT2, (b) NAT3, (c) AC1, (d) AC2 and (e) AC3 averaged on January 2007.....	94
A.2 The difference of MSLP between the observations from ECMWF and the model output for scenarios (a) NAT2, (b) NAT3, (c) AC1, (d) AC2 and (e) AC3 averaged on January 2007.	95
A.3 The difference of temperature at 850 hPa between the observations from ECMWF and the model output averaged over January 2007 for aerosol scenarios (a) NAT2, (b) NAT3, (c) AC1, (d) AC2 and (e) AC3 averaged on January 2007.	96
B.1 Statistically significant area (gray) for RH_i at 850 hPa for January 2007 for aerosol scenario NAT1 and AC1 where results are valid with a confidence level of 95%.....	100
D.1 Significant area for temperature anomaly for January 2007 for all six pairs calculated using the Student t-test. The gray areas indicate significant zone with a confidence level of 95%.	104
D.2 Significant area for anomaly of relative humidity with respect to ice for January 2007 for all six pairs calculated using the Student t-test. The gray areas indicate significant zone with a confidence level of 95%.....	105
D.3 Significant area for anomaly of ice water content for January 2007 for all six pairs calculated using the Student t-test. The gray areas indicate significant zone with a confidence level of 95%.	106
D.4 Significant area for anomaly of liquid water content for January 2007 for all six pairs calculated using the Student t-test. The gray areas indicate significant zone with a confidence level of 95%.	107
D.5 Significant area for anomaly of ice crystal concentration for January 2007 for all six pairs calculated using the Student t-test. The gray areas indicate significant zone with a confidence level of 95%.	108
D.6 Significant area for anomaly of liquid drop concentration for January 2007 for all six pairs calculated using the Student t-test. The gray areas indicate significant zone with a confidence level of 95%.	109
D.7 Significant area for anomaly of cloud forcing at the surface for January 2007 for all six pairs calculated using the Student t-test. The gray areas indicate significant zone with a confidence level of 95%.	110

D.8 Significant area for anomaly of cloud forcing at the top of the atmosphere for January 2007 for all six pairs calculated using the Student t-test. The gray areas indicate significant zone with a confidence level of 95%.....	111
D.9 Significant area for anomaly of liquid water path for January 2007 for all six pairs calculated using the Student t-test. The gray areas indicate significant zone with a confidence level of 95%.	112
D.10 Significant area for anomaly of ice water path for January 2007 for all six pairs calculated using the Student t-test. The gray areas indicate significant zone with a confidence level of 95%.	113

LISTE DES TABLEAUX

Tableau	Page
2.1 Periods of integration for all simulations. Mentioned are the beginning and end of each simulation, spin-up duration and the analysis period considered for all simulations	19
2.2 Introduction of six aerosol scenarios to check the Arctic climate sensitivity	22
2.3 Introduction of the components of six pairs to check the Arctic climate sensitivity	23
3.1 The mean January differences of geopotential height at 500 hPa, the MSLP and the temperature at 850 hPa with the ECMWF analysis averaged over the Arctic for aerosol scenario NAT1	26
3.2 Pair 1 temperature anomaly at 1000, 850 and 500 hPa and cloud forcing anomaly at TOA and surface at the surface averaged over the sub-domain delimited by sea-ice boundaries	35
3.3 Pair 5 temperature anomaly at 1000, 850 and 500 hPa and cloud forcing anomaly at TOA and surface at the surface averaged over the sub-domain delimited by sea-ice boundaries	75
C.1 Student t table	102

LISTE DES ACRONYMES

3D	Three dimension
AMIP	Atmospheric Model Intercomparison Project
CKD	Correlated-K Distribution
CNT	Classical Nucleation Theory
CRCM	Canadian Regional Climate Model
CRF	Cloud Radiative Forcing
DGF	Dehydration-greenhouse feedback
ECMWF	European Center of Medium-Range Weather Forecast
IN	Ice-forming nuclei
IR	Infrared
ISBA	Interactions Soil-Biosphere-Atmosphere
IWP	Ice Water Path
LWP	Liquid Water Path
MSLP	Mean Sea Level Pressure
ptb	perurbed
PDF	Probability Density Function
rad	Radian
ref	reference
RH _i	Relative Humidity with respect to ice
S _{ice}	Saturation ratio with respect to ice
SIC	Sea Ice Cover
SST	Sea Surface Temperature
t	Observation time
TOA	Top of the Atmosphere
UTC	Coordinated Universal Time

LISTE DES SYMBOLES

α	Contact angle
σ	Standard deviation
$\sigma_{i/v}$	Ice-vapor interfacial energy
$\sigma_{w/v}$	Liquid water-water vapor interfacial energy
$\sigma_{v/s}$	Water vapor-IN substrate interfacial energy
$\sigma_{w/s}$	Liquid water-IN substrate interfacial energy
β	Spectral shape parameter
ρ	Liquid water density
ρ_a	Air density
μ	Mean contact angle
μ_{ref}	Real population mean in original case
μ_{ptb}	Real population mean in perturbed case
A	Pre-exponential factor
A_k	Area of a single Kaolinite particle
AC1	Bertram parameterization of acid ($\alpha = 27^\circ$) with contact
AC2	Bertram parameterization of acid ($\alpha = 27^\circ$) without contact
AC3	Bertram parameterization (α -PDF) with contact
$Al_2Si_2O_5(OH)_4$	Kaolinite
B	Normalization constant
$^\circ C$	Degree Celsius
CFC ₁₁₋₁₄	Freon 11-14
CH ₄	Methane
CO ₂	Carbon dioxide
C _p	Heat capacity at constant pressure
dRH _i	Anomaly of relative humidity with respect to ice
Δg_{diff}	Energy per bond in water

ΔF_{het}	Free energy of formation of critical embryo in heterogeneous nucleation process
Δt	Time step
$f(\alpha)$	Probability distribution function
$f_{\text{het}}(m_{i/v}, X)$	Compatibility function
h	Planck's constant
H^+	Cation of hydrogen
GEM-LAM	Area version of the Global Environmental Multi-scale model
GEMCLIM	GEM-LAM in climate mode
H_a	Alternative hypothesis
H_0	Null hypothesis
H_2O	Water
H_2SO_4	Sulfuric acid
J_{het}	Heterogeneous ice nucleation rate per unit particle surface area
J_{hom}	Homogeneous ice nucleation rate per unit particle surface area
k	Boltzmann constant
N_{conB}	Brownian diffusion contact IN number concentration
N_{conD}	Diffusiomorphosis contact IN number concentration
N_{conT}	Thermophoresis contact IN number concentration
L_{iv}	Evaporation latent heat
L_s	Latent heat of sublimation
m_{i0}	Initial mass of an ice crystal
$m_{i/v}$	Cosine of the contact angle
N_{contact}	Contact ice crystal concentration
$N_{\text{deposition}}$	Deposition ice crystal concentration
N_{max}	Maximum deposition ice crystal concentration
N_{total}	Total primary ice nucleation concentration
NAT1	Bertram parameterization ($\alpha = 12^\circ$) with contact
NAT2	Bertram parameterization ($\alpha = 12^\circ$) without contact
N_x/N_y	Number of grid points in x and y direction

NAT3	Bertram parameterization with contact
N_c	Total concentration of each hydrometeor category
N_i	Molecular concentration of ice
N_f/N_o	Nucleated fraction in heterogeneous nucleation process
N_2O	Nitrous oxide
NH_4^+	Ammonium cation
$(NH_4)_2SO_4$	Ammonium sulfate
N_f/N_o	Frozen fraction of ice nucleus
N_{max}	Maximum nucleation rate for primary nucleation
n_s	Number density of water molecules at the IN-water interface
n_v	Number density of water molecules
O_3	Ozone
q	Saturation mixing ratio
q_s	Ice saturation mixing ratio
r	Correlation coefficient
r_a	Kaolinite radius
r_g	Critical embryo radius
R_v	Gas constant for water vapor
SO_4^{-2}	Sulfate anion
SO_2	Sulfure dioxide
s_{ptb}^2	Variances of the ensemble of n_{ptb} elements
s_{ref}^2	variances of the ensemble of n_{ref} elements
T	Environment temperature
$T_{n_{ref}+n_{ptb}-2;\gamma}$	Critical Student distribution value
x	Substrate radius to spherical ice germ radius ratio
$X_{i,j}$	Variable at the grid point (i,j) from the k^{th} run of ensemble of n simulations
$\overline{X}_{i,j}$	Mean value of variable X

RÉSUMÉ

La présence d'un intense système de basse pression sur l'Islande et d'un anticyclone centré sur la Sibérie pendant l'hiver favorise le transport à grande échelle des émissions anthropiques tel que l'acide sulfurique (H_2SO_4) de latitudes moyennes vers l'Arctique. Cet acide sulfurique recouvre les NGs (Noyau glaçogène) d'une couche mince lors des épisodes de pollution et contribue ainsi à augmenter l'angle de contact ($\alpha = 27^\circ$) des NGs par rapport au cas naturel ($\alpha = 12^\circ$). Cela conduit à la quasi-désactivation de la nucléabilité des aérosols sulfatés et diminue substantiellement la concentration des NGs. Cela contribue à la formation de cristaux de glace moins nombreux mais plus gros qui précipitent plus efficacement des nuages (précipitation de ciel clair). En raison de la déshydratation de la basse troposphère et des modifications de la microstructure des nuages de bas niveaux et des nuages glacés de moyenne et haute altitudes, plus de rayonnement terrestre s'échappe de la troposphère. Cette perte de rayonnement infrarouge intensifie l'inversion de température en Arctique, refroidit la basse atmosphère par l'effet de la Rétroaction déshydratation-effet de serre (RDES).

Plusieurs études de modélisation utilisant des modèles 1D et 3D (Girard et Bekcic, 2005; Girard et Stefanof, 2007 et Girard *et al.*, 2012) ont étudié l'impact d'enrobage de l'acide sulfurique sur les nuages et sur le bilan radiatif pendant l'hiver arctique. Ces études de modélisation supposent que seulement nucléation par déposition est modifiée par enrobage acide. Les résultats obtenus ont confirmé le refroidissement troposphérique produit par les RDES.

L'objectif de cette recherche est tout d'abord de déterminer l'importance relative de la nucléation par contact des cristaux et d'investiguer l'impact de l'acidification d'aérosols sur la nucléation par contact, et par conséquent sur les propriétés microphysiques et optiques et sur le bilan radiatif des nuages arctiques pendant l'hiver par la théorie classique de la nucléation (CNT). Cette dernière suggère un cadre simple pour paramétrer le taux de nucléation hétérogène de la glace en fonction de diverses propriétés physiques et structurels des NGs tels que l'angle de contact (l'angle entre le substrat de NG et l'embryon de glace formé sur le NG) qui est considérés constante pour tous les NGs (single- α). Un second objectif est d'implémenter l'approche PDF (paramétrisation de l'angle de contact des NGs de déposition selon la distribution de fonction de densité de probabilité) de l'angle de contact dans le schéma microphysique et vérifier l'impact de l'approche PDF pour la nucléation par déposition sur les résultats.

Cette étude est réalisée à travers six ensembles de simulations pour janvier 2007, simulé par GEM-LAM (une version à aire limitée du modèle Global Environnemental à Multi-échelle) au-dessus de l'Arctique. Chaque ensemble correspond à deux scénarios d'aérosols différents qui diffèrent l'un à l'autre par un seul paramètre,

incluent l'effet d'acidification, l'approche alpha-PDF et la nucléation par contact. Cette classification permet d'étudier la sensibilité du climat arctique hivernal à l'effet des paramètres en question. Les résultats indiquent que, contrairement à l'attente intuitive, la contribution des NGs de contact sur la formation de cristaux de glace dans les nuages arctiques hivernal est très faible (anomalie moyenne négative de forçage des nuages de -0.03 W/m^2 au sommet de l'atmosphère et -1.02 W/m^2 à la surface et anomalie de température négligeable) et cet effet est encore plus faible dans une masse d'air acidifiée. Donc, la microstructure des nuages est modifiée mais pas suffisamment pour faire une différence significative sur le bilan radiatif. Aussi, le paramétrage PDF n'a pas un grand effet sur la microstructure des nuages et le bilan énergétique (anomalie moyenne négative de forçage des nuages de -0.83 W/m^2 au sommet de l'atmosphère et -0.69 W/m^2 à la surface et anomalie de température négligeable aux milieux non acide). Ces résultats montrent donc que l'altération de la nucléation par contact lorsque les NGs sont recouverts d'acide a un effet négligeable comparé à la même altération sur les NGs de déposition, et ce peu importe l'approche utilisée pour l'angle de contact.

Key words: ice nuclei, contact nucleation, deposition nucleation, Arctic cloud

ABSTRACT

The presence of an intense low-pressure system over Iceland and a high pressure system centered over Siberia during the winter promotes large-scale transport of anthropogenic emissions such as sulfuric acid (H_2SO_4) from the mid-latitude to the Arctic. This sulfuric acid coats INs (ice nuclei) with a thin layer during episodes of pollution and contributes to increase the contact angle ($\alpha = 27^\circ$) of INs compared to the uncoated INs ($\alpha = 12^\circ$). As a result, the INs lost their ice nucleation ability leading to a substantial decrease of the concentration of INs. This contributes to the formation of fewer but larger precipitating ice crystals. Due to dehydration of the lower troposphere and optically thinner low-level and ice clouds, more terrestrial radiation escapes from the troposphere. This loss of infrared radiation intensifies the temperature inversion in the Arctic and cools the atmosphere.

Several modeling studies using 1D and 3D models investigated the impact of IN sulfuric acid coating on the clouds microstructure and on the cloud radiation balance during the Arctic winter. These modeling studies assume that only deposition nucleation is modified by the acid coating. The obtained results confirmed the tropospheric cooling caused by the DGF.

Contact ice nucleation, which is another freezing process, is likely to be altered by sulphuric acid coating. The purpose of this research is first to determine the relative importance of contact ice nucleation on the formation of Arctic ice clouds when the INs are uncoated and coated with sulphuric acid. To reach this objective, the GEM-LAM (limited area version of Global Environmental Multi-scale model) model is used with a two-moment microphysics scheme. For deposition ice nucleation, the classical nucleation theory (CNT) is used while contact freezing is parameterized with an empirical relationship. The CNT is a simple framework to set the heterogeneous ice nucleation rate depending on various structural and physical properties of INs such that the contact angle (the angle between the substrate and the IN embryo ice formed on IN) is considered constant for all INs (single- α). A second objective is to implement the PDF (parameterization of the contact angles of INs in deposition mode according to the distribution of probability density function) of the contact angle in the microphysics scheme approach and to verify the impact of PDF approach on the results.

This study was conducted through six sets of simulations for January 2007, simulated by GEM-LAM over the Arctic. Each set corresponds to two different aerosol scenarios, which differ from each other in a single parameter including the acidification of the INs, alpha-PDF approach and the presence of the contact freezing. This classification allows studying the sensitivity of winter Arctic climate to the effect of these parameters. The results indicate that, as opposed to the intuitive expectations, the contribution of contact INs on the formation of ice crystals in the

Arctic winter clouds is very low (negative average cloud forcing anomaly of -0.03 W/m^2 at the top of the atmosphere and -1.02 W/m^2 at the surface and negligible temperature anomaly) and this effect is even lower in an acidified air mass. Therefore, the microstructure of clouds is modified but not enough to make a significant difference in the radiation balance. Also, the PDF approach does not have a large effect on the microstructure of clouds and on the energy balance (negative mean cloud forcing anomaly of -0.83 W/m^2 at the top of the atmosphere and -0.69 W/m^2 at the surface and negligible temperature anomaly for non-acidic air mass). These results show that the alteration of the contact nucleation when the INs are covered by sulphuric acid has a negligible effect compared to the same alteration on deposition INs regardless of the approach used for the contact angle.

Mots clés: noyaux glaçogènes , nucléation par contact, nucléation par déposition, nuages arctiques

CHAPTER I

INTRODUCTION

Ice formation in the atmosphere occurs by either homogeneous freezing of water droplets or heterogeneous ice nucleation. Homogeneous freezing requires super cooling of water droplets at temperatures lower than -38°C (Pruppacher and Klett, 1998). On the other hand, heterogeneous ice nucleation starts at temperatures much higher than the threshold for homogeneous freezing, in the presence of insoluble or partially soluble aerosol particles called ice-forming nuclei (IN). The latter nucleation process is responsible for ice formation in tropospheric clouds at temperatures higher than -38°C and occurs through four different modes: (1) contact freezing occurs after the collision of a dry IN with a super-cooled drop, (2) deposition ice nucleation is the direct growth of ice from the vapour phase on a dry IN in ice super-saturated and liquid sub-saturated conditions, (3) immersion freezing is caused by an immersed IN within a liquid water drop or haze droplet and (4) condensation freezing refers to the sequence of events whereby liquid water first condenses from the vapour on the IN surface immediately followed by freezing of the liquid at liquid water saturation condition.

The INs serve to lower the free energy barrier for ice nucleation and help the water molecules to align in an ice-like structure, thus facilitating the phase transition from vapour or liquid water to ice at higher temperatures and lower relative humidities compared to homogeneous freezing.

Mineral dust particles are the most common and efficient IN in the atmosphere. Kaolinite particles represent a major component of highly efficient mineral dust and

make up to 50% of atmospheric mineral dust particles (Claquin *et al.*, 1999; Kumai, 1961; DeMott *et al.*, 2003b and Eastwood, 2008) and are proved to be a potent IN. They nucleate ice crystals in the deposition, contact, immersion and condensation freezing modes at a relatively high temperature (Pruppacher and Klett, 1998).

The onset temperature and relative humidity for heterogeneous ice formation depends on the nucleation mode and the type of IN. Recent laboratory experiments done on the heterogeneous nucleation of ice crystals on kaolinite mineral particles demonstrate that, in the deposition mode, this particle can nucleate ice at 251 K and 123% relative humidity with respect to ice (RH_i) and at 112% RH_i at temperature ranging from 233 to 246 K (Salam *et al.*, 2006). In the immersion mode, ice formation is initiated in a temperature range from 243 to 259 K while in contact mode, ice crystals nucleate at substantially higher temperatures ranging from 266 to 268 K (Pitter and Pruppacher, 1973; Eastwood *et al.*, 2008; Svensson *et al.*, 2009). These results clearly show that contact nucleation is the most efficient heterogeneous ice nucleation mode involving kaolinite particles as the solid-liquid-air interface strongly favours ice nucleation.

The IN particles can have a great influence on the climate through their interactions with the cloud ice formation processes (DeMott *et al.*, 2003a; 2003b; Richardson *et al.*, 2007) and subsequently on the cloud microstructure, the surface energy budget and on the precipitation as any changes in these parameters are capable of modifying the climate (e.g. Girard *et al.*, 2012 and references therein).

This effect is very important in the Arctic because it is a unique region characterized by very low temperature and humidity, high cloud cover and surface albedo, absence of solar radiation during winter and frequent surface based temperature inversion.

Mixed-phase clouds, containing both liquid and frozen water, are the predominant cloud type in the Polar Regions (Hoose *et al.*, 2008). Through various feedback mechanisms, these long-lived clouds have a great impact on the Arctic climate (Avramov and Harrington., 2001). During the polar night, they produce a

positive cloud radiative forcing ranging from 20 to 40 W m⁻² at the surface while during summer the cloud radiative forcing is close to zero due to the balance between the forcing in the solar and infrared radiation (Shupe and Interieri, 2004). The lifetime of mixed-phase clouds depends strongly on the ambient concentration of ice nuclei (Harrington *et al.*, 1992). The microstructure of ice clouds are also very sensitive to the concentration of IN. Previous modeling studies have shown that the cloud radiative forcing both at the surface and at the top of the atmosphere can be substantially altered when the IN concentration is modified (e.g. Hoose *et al.*, 2008; Girard *et al.*, 2012; Girard and Stefanof, 2007).

The IN concentration in the Arctic is highly variable and depends on the season. As opposed to the summer, during the cold season, most of the aerosols are transported from the mid-latitudes. This is due to the lack of local aerosol sources over the ice and snow covered surface. In fact, the presence of an intense low-pressure system over Iceland and a strong anticyclone centered over Siberia during the winter is favorable to the transport of anthropogenic pollution emissions from the mid latitude regions such as Northern European cities, China and Siberia and dust originating from East Asian deserts toward the Arctic. Therefore, the Arctic air mass can be highly polluted during the cold season by these anthropogenic aerosols and gaseous precursors (Girard *et al.*, 2012; Girard and Bekcic, 2005; Shaw, 1995). According to Iversen (1996), 70% of anthropogenic pollutants originate from Europe while sources from Asia contribute to almost 30% of it.

A large amount of anthropogenic gaseous precursors is made of sulfur dioxide. During the oxidation process, sulfur dioxide converts into sulfate (SO₄⁻²), which can thereafter react with hydrogen cations (H⁺) to form sulfuric acid (H₂SO₄) or ammonium cation (NH₄⁺) to form ammonium sulfate ((NH₄)₂SO₄) (Seinfeld, 1986). In the Arctic during winter, the concentration of ammonia and ammonium cation is low due to the lack of local sources. As a result, aerosols can be highly acidic in cases where the concentration of sulphate is large (Bigg, 1980). According to Bigg (1980), most of the aerosols in the accumulation mode are coated with a thin film of sulfuric acid during winter.

Eastwood *et al.* (2008; 2009) have shown that the ice nucleation properties of uncoated and sulfuric acid coated kaolinite particles are very different. The onset relative humidity with respect to ice (RH_i) for deposition ice nucleation initiation increases drastically in acid coated particles requiring an extra 30% of RH_i to initiate nucleation (Eastwood *et al.*, 2009; Chernoff and Bertram, 2010). Other experimental data (in-situ measurements) have shown that this process reduces the concentration of active deposition INs in the cloud levels (Borys, 1989). Also Sullivan (2010) experiment result on the acid coating effect on the coated aerosols suggests that the de-activation effect of the INs is irreversible. The coated INs do not retrieve their ice nucleation properties even after being neutralized with ammonia (Sullivan *et al.*, 2010).

As explained above, since acid coated INs initiate deposition nucleation at higher RH_i and lower temperatures compared to uncoated particles, at the same temperature and humidity conditions, there would be lower active deposition INs in acidified scenario compared to clean scenario (Girard *et al.*, 2012; Borys, 1989).

Blanchet and Girard (1994) were the first to hypothesize the effects acid coating on INs could have on the Arctic climate during the cold season. According to their hypothesis, the acid coated aerosols decrease the heterogeneous nucleation rate of ice crystals. In ice clouds, there is more water vapour available for each ice crystal when compared to unpolluted case. As a result, ice crystals grow to larger sizes. In mixed-phase clouds, ice crystals are nucleated in the thin liquid layer located at cloud top and rapidly grow by the Wegener-Bergeron-Findeisen effect (the growth of ice crystal at the expense of liquid water under ice sub-saturation and water super-saturation conditions) (Girard et Stefanof, 2007). Bigger ice crystals have larger terminal velocity and precipitate more efficiently. Thus, the acid coating contributes to dehydrate the troposphere by increasing the precipitation over a large area. Therefore, cloud ice water content is significantly reduced. The dehydration results in the decrease of the greenhouse effect due to the strong effect of water vapour and enhanced atmosphere transmissivity. Modeling studies have shown that the increased emissivity of mixed-phase clouds located in the lower troposphere

combined to the increased transmissivity of the optically thinner ice clouds upper in the troposphere produces a tropospheric cooling ranging between 0 and 2 K when compared to an uncoated aerosol scenario (Girard *et al.*, 2012; Hoose and Kristjansson, 2008; Girard and Stefanof., 2007).

The above-mentioned laboratory studies have investigated the acid coating effect on the deposition ice nucleation and immersion freezing. Because of technical complexities, the effect of acid coating of INs on contact freezing has not been investigated so far. However, it is likely that contact nucleation may also be altered by acid coating too (e.g. Hoose *et al.*, 2008).

Morrison *et al.* (2005) investigated the importance of ice nucleation on the lifetime of Arctic mixed-phase clouds using a 1-D cloud model. They found that the low-level Arctic mixed-phase clouds are highly sensitive to the mode of nucleation. They also showed that the lifetime of these clouds is highly sensitive to the concentration of the deposition INs and much less sensitive to the number concentration of contact INs. Some in situ observations and laboratory experiments show that the scavenging and precipitation at the mixed-phase cloud level depletes rapidly the deposition INs increasing the mixed-phase stratiform clouds lifetime (e.g., Harrington *et al.*, 1999; Jiang *et al.*, 2000, Morrison *et al.*, 2005). The scavenging has little impact on the concentration of contact INs in mixed-phase clouds since few active contact nuclei initiate ice nucleation upon contact with water drops (Morrison, 2005). As a result, the contact nucleation mode dominates in the Arctic mixed-phase cloud layers and controls the ice formation process when both nucleation modes are considered, contributing to the formation of long-lived co-existence of liquid and ice (Young, 1974; Hobbs and Rangno, 1985). The dominant role of the contact nucleation mode in the Arctic mixed-phase clouds suggest the need to investigate in more details its role within arctic mixed-phase and consequently in the Arctic climate. However some other studies contradict the dominance of contact nucleation in Arctic mixed-phase clouds by giving the dominant role to the deposition nucleation mode (Harrington *et al.*, 1999; Harrington and Olsson, 2001; Avramov and Harrington, 2001).

In the Hoose *et al.* (2008) study on the influence of dust mineralogical composition on heterogeneous ice nucleation in mixed-phase clouds, the deposition freezing potential is believed to be less important and has been neglected. The contact nucleation mode was assumed to be dominant in the formation of Arctic mixed-phase clouds. They investigate the sensitivity of the climate to the anthropogenic emission effect through simulations for present-day and preindustrial era using the coupled aerosol–climate model ECHAM5-HAM. In their present-day simulations, they assumed coated INs. Therefore, contact ice nucleation was suppressed. The simulation result gives an annual mean difference of -0.6 W/m^2 in longwave radiative flux between the present day and the preindustrial era the top of the atmosphere in the northern hemisphere where the glaciations ability of part of INs are reduced by anthropogenic pollutant emission (Hoose *et al.*, 2008).

According to the above-mentioned studies, the importance of contact ice nucleation is still unclear. More work needs to be done on its importance and whether or not deactivated contact IN by acid coating could have a substantial effect on the Arctic clouds and radiation during winter. This study investigates the role of deposition and contact ice nucleation modes in clean (uncoated IN) and polluted (sulfuric acid coated IN) air masses to study their role in winter time Arctic clouds and subsequently on the Arctic climate.

This thesis is organized into three main chapters beginning with the theoretical concepts. The second chapter presents the methodology and describes the numerical model GEM-LAM and experimental set-up including land-surface, radiation and microphysical schemes of the model and discusses the simulation configuration and explanations of the various processes of ice nucleation. The third chapter is devoted to the presentation and analysis of results. Finally the conclusion of this study will be presented at the end.

CHAPTER II

METHODOLOGY

2.1 Description of the model GEM-LAM

All the simulations have been performed with the version 3.3.0 of the Limited Area Global Environmental Multi-scale model (GEM-LAM) in climate mode. This model includes 53 vertical levels with the highest level located at 10 hPa. The numerical formulation and physics package of the model is described in details by Côté *et al.* (1998). The physics package contains several operational parameterizations for the physical phenomena such as turbulent flux of momentum, heat and moisture, surface layer effects, gravity wave drag, prognostic clouds, solar and infrared radiation with or without interaction with clouds, deep and shallow convection, condensation and precipitation. The surface scheme is ISBA (Interactions Soil-Biosphere-Atmosphere) from Noilhan and Planton (1989). It determines the lower boundary conditions for the vertical diffusion of temperature, moisture, and momentum. It also computes the hydrological surface budget and evolution in time of the following prognostic variables according to the continuous formulation discussed in Noilhan and Planton (1989): surface temperature (representative of both canopy and soil surface), mean (or deep-soil) temperature, surface volumetric water content, liquid and frozen bulk soil water contents, liquid water retained on the vegetation canopy foliage, equivalent water content of the snow reservoir, liquid water retained in the snow pack, snow albedo, and relative snow density (Noilhan and Planton, 1989). In the following subsections, the radiation

parameterization and the microphysics scheme are described in details because of their important role in the current investigation.

2.1.1 Correlated-k radiation Scheme

The radiative transfer scheme in GEM-CLIM is from Li and Barker (2005) is based on the correlated-k distribution (CKD) method for gaseous transmission to handle the overlap of several gases (here H₂O, CO₂, O₃, N₂O, CH₄, CFC₁₁₋₁₄). It has 9 bands in the long-wave frequencies and 3 bands in the shortwave frequencies (Li and Barker, 2005).

In this scheme the transmission function for each gaseous absorber in k space is defined by the following equation

$$Tr(w) = \int_0^{\infty} e^{-wk} f(k) dk \quad (2.1)$$

Where w is the amount of the vertically integrated absorber amount (kg/m²), k is absorption coefficient of the gas and $f(k)$ is the k -distribution function and is given by:

$$f(k) = \frac{1}{\Delta\nu} \int_{\Delta\nu} \delta[k - k(\nu)] d\nu \quad (2.2)$$

in which $k(\nu)$ is frequency dependent absorption coefficient of the gas in the space of frequency ν , $\Delta\nu$ in the incident wave band width and $\delta[k - k(\nu)]$ is the Dirac function.

2.1.2 Microphysics scheme of Milbrandt and Yau

The microphysics scheme used in this project is from Milbrandt and Yau (2005a,b). There are three versions of this scheme: one-moment, two-moment and three-moment bulk approaches. The hydrometeors are divided into six classes including cloud droplets, cloud ice crystals, raindrop, snow, graupel and hail.

The one moment version predicts the mixing ratio for all types of hydrometeors (cloud droplets, cloud ice crystals, raindrop, snow, graupel and hail). In the double moment approach, the prognostic mixing ratio and total number concentration of hydrometeors are independently predicted. The hydrometeor size distribution is described by a gamma size distribution function $N(D) = N_c D^\beta e^{-\lambda D}$, in which N_c (the intercept of the size of each category) and λ are prognostic parameters; D is the diameter of an individual hydrometeor and β is the spectral shape parameter that has a constant value. Recently, a three-moment scheme was introduced in which β is diagnosed from a monotonically increasing function of the mean-mass diameter (Milbrandt and Yau, 2005a). In the three-moment version, the shape parameter is a prognostic variable that varies in a bulk parameterization. It is obtained by solving the sixth moment predictive equation (Milbrandt and Yau, 2005a; 2005b).

In this study, we use the two-moment version with a constant (one for cloud and 0 for hail, graupel, snow and rain) spectral shape parameter. The scheme is composed of three main parts; the preliminary calculations are done in part one, the second part deals with the cold microphysics processes and both sources and sinks of ice phase in the atmosphere, and the last part is devoted to warm cloud microphysics processes and is based on Cohard and Pinty (2000a).

2.1.2.1 Ice nucleation in deposition-immersion mode

Either primary ice nucleation, collection process (conversion, accretion and aggregation) of ice particles or homogeneous freezing of cloud droplets are

of ice phase in the atmosphere, and the last part is devoted to warm cloud microphysics processes and is based on Cohard and Pinty (2000a).

2.1.2.1 Ice nucleation in deposition-immersion mode

Either primary ice nucleation, collection process (conversion, accretion and aggregation) of ice particles or homogeneous freezing of cloud droplets are considered as the source of the ice phase formation in the atmosphere. In the first freezing mode, the deposition-immersion freezing parameterization is based on Bertram parameterization (Wheeler and Bertram, 2011) and occurs when the supersaturation with respect to ice is reached. In the original version of the scheme, the parameterization of Meyers *et al.* (1992) was used. In the version of the scheme used in this study, the approach of Du *et al.* (2011) and Girard *et al.* (2012) is considered. This approach is based on the classical nucleation theory. The parameterization represents both the nucleation by deposition on uncoated INs and the immersion freezing of coated INs, which are inactivated haze particles.

The total number of ice crystal formed by deposition nucleation in dt ($N_{\text{deposition}}$) is given by the following equation:

$$N_{\text{deposition}} = N_o \left(1 - \exp \left(A_K A \exp \left(\frac{16\pi\sigma_{iv}^3 f(m_{iv})}{3k^3 N_i^2} \right) \int_{t_0}^t \frac{dt}{T^3 [\ln S_{ice}]^2} \right) \right) \quad (2.3)$$

where A is the pre-exponential factor (Pruppacher and Klett, 1998), A_K is the area of a single kaolinite particle, σ_{iv} is the ice-vapor interfacial energy (0.106 J m^{-2}), N_i is the molecular concentration of ice (cm^{-3}), S_{ice} is the saturation ratio with respect to ice, N_o is the total number concentration of deposition ice nuclei ($=100000 \text{ m}^{-3}$), k is the Boltzmann's constant ($1.380622 \times 10^{-23} \text{ J K}^{-1}$), T is the temperature (K) and $f(m_{iv})$ is defined as the equation below:

$$\begin{aligned}
& \left. \left. \left. \frac{1}{2} \left(\frac{r_a}{r_g} \right)^3 \left(2 - 3 \left(\frac{\frac{r_a - \cos \alpha}{r_g}}{\sqrt{1 - 2 \left(\frac{r_a}{r_g} (\cos \alpha) + \left(\frac{r_a}{r_g} \right)^2 \right)}} \right) + \left(\frac{\frac{r_a - \cos \alpha}{r_g}}{\sqrt{1 - 2 \left(\frac{r_a}{r_g} (\cos \alpha) + \left(\frac{r_a}{r_g} \right)^2 \right)}} \right) \right) \right) \right) \right)^3 \\
& + \frac{1}{2} \left(3 \cos \alpha \left(\frac{r_a}{r_g} \right)^2 \left(\left(\frac{\frac{r_a - \cos \alpha}{r_g}}{\sqrt{1 - 2 \left(\frac{r_a}{r_g} (\cos \alpha) + \left(\frac{r_a}{r_g} \right)^2 \right)}} \right) - 1 \right) \right) \right) \quad (2.4)
\end{aligned}$$

where α is the contact angle (the angle between the ice embryo and the substrate of the IN), r_a is the kaolinite radius and is equal to $0.39 \mu\text{m}$ (Girard *et al.*; 2013) and r_g is the critical embryo radius and is defined as:

$$r_g = \frac{2\sigma_{iv}}{\rho R_v T \ln S_{ice}} \quad (2.5)$$

where ρ is the liquid water density and R_v is the gas constant for water vapour.

The contact angle is set to 12° for uncoated dust INs and 27° for sulphuric acid coated dust INs. These values are based on laboratory experiments of Eastwood *et al.* (2008; 2009).

To avoid the over depletion of water vapor by the ice nucleation process, the nucleation rate is limited by a maximum value for deposition ice crystal concentration, N_{max} , defined by the following equation:

$$N_{\max} = \frac{\rho}{m_{i0}} \frac{q - q_{si}}{1 + \left(\frac{5806.485 L_s q_{si}}{c_p (T - 7.66)^2} \right)} \frac{1}{2\Delta t} \quad (2.6)$$

where ρ is the density, m_{i0} is the initial mass of nucleated ice crystal (10^{-12} kg), q is the mixing ratio and q_s is the ice saturation mixing ratio, L_s is the latent heat of sublimation (283.5×10^4 J kg^{-1}), c_p is the specific heat at constant pressure and Δt is the time step.

The parameterization for deposition ice nucleation has been modified in this study to better reproduce the laboratory experiments of Eastwood *et al.* (2008; 2009). The approach of Wheeler and Bertram (2012) is adopted in which the contact angle is not constant but rather represented by a probability distribution.

From the equation 2.3, the single contact angle can be calculated by fitting the measured RH_i required to nucleate 1% of available ice nucleus (Wheeler and Bertram, 2011).

However the results of a recent research on this subject proves that none of the frozen fraction-saturation ratio graphs related to fixed contact angles of 3° , 7° and 14° could capture the increasing slope of N_i/N_o with increasing S_{ice} as derived from experimental data; therefore the single contact angle model fails to describe the surface properties of all INs (Wheeler and Bertram, 2011).

In order for CNT to better model the experimental data, the original CNT framework in which a single contact angle is assumed to all available INs (hereafter called single- α scenario) needs to be generalized to a more exact framework. This new framework assigns a single contact angle for each individual IN but a distribution of contact angles to different INs. The probability of occurrence of each contact angle is given by a probability density function (PDF) to incorporate the variability in the IN surface properties (α -PDF scenario) (Wheeler and Bertram, 2011;

In order for CNT to better model the experimental data, the original CNT framework in which a single contact angle is assumed to all available INs (hereafter called single- α scenario) needs to be generalized to a more exact framework. This new framework assigns a single contact angle for each individual IN but a distribution of contact angles to different INs. The probability of occurrence of each contact angle is given by a probability density function (PDF) to incorporate the variability in the IN surface properties (α -PDF scenario) (Wheeler and Bertram, 2011; Marcolli *et al.*, 2007). In this approach, the nucleability of each single IN is equal over the entire surface but varies from particle to particle.

This representation of contact angle with a Gaussian probability distribution function described by the following equation fits pretty well the experimental data:

$$f(\alpha) = B \exp\left[-\frac{(\alpha - \mu)^2}{2\sigma^2}\right] \quad (2.7)$$

here μ and σ are the mean and standard deviation of the distribution and B is the normalization constant such that

$$\int_0^\pi f(\alpha) d\alpha = 1 \quad (2.8)$$

Considering the variation of contact angle of INs, the nucleated fraction derived by the CNT needs to be restated to the following relation between the nucleated fraction and heterogeneous nucleation rate:

$$\frac{N_f}{N_0} = 1 - \int_0^\pi \exp[-J(\alpha)At] f(\alpha) d\alpha \quad (2.9)$$

As opposed to the single contact angle model parameterization, the heterogeneous nucleation rate varies from particle to particle because of varying contact angle in the PDF parameterization.

Results of the study conducted by Kulkarni (2012) on variable dust particle sizes at different temperatures show that the contact angle in single- α scenario does not show significant dependency to the experimental parameters such as temperature, relative humidity with respect to ice or the size of the dust particle. However, in the α -PDF scenario the contact angle parameters are significantly sensitive to the above-mentioned experimental parameters. Therefore any change in environment conditions has a rather big effect in the ice forming ability and consequently on clouds properties (Kulkarni *et al.*, 2012).

2.1.2.2 Ice nucleation in contact mode

Contact nucleation (including, diffusiophoresis, thermophoresis and Brownian diffusion) is parameterised following Cotton *et al.* (1986) and Walko *et al.* (1995). Contact freezing occurs at temperatures below -2 °C in the presence of liquid water. According to this parameterization of contact nucleation, the number of crystals produced by diffusiophoresis, thermophoresis and Brownian diffusion is respectively defined by the following three equations:

$$\frac{N_{conD}}{dt} = F_1 F_2 \frac{R_v T}{L_{lv} \rho_a} \quad (2.10)$$

$$\frac{N_{conT}}{dt} = \frac{F_1 F_2 f_t}{\rho_a} \quad (2.11)$$

$$\frac{N_{conB}}{dt} = F \psi_a \quad (2.12)$$

where R_v is the gas constant for water vapour, ρ_a is the air density, T is the air temperature (K), L_{lv} is the latent heat. F_1 , F_2 , f_t and ψ_a are respectively defined by equations (2.13), (2.16), (2.17) and (2.19) :

$$F_1 = 2\pi D_c N_{ic} N_a \quad (2.13)$$

where D_c is the cloud droplet diameter, N_{ic} is the cloud droplet concentration and N_a is the concentration of INs available for contact freezing and is defines as:

$$N_a = \exp(4.11 - 0.262T_c) \quad (2.14)$$

where T_c is cloud droplets temperature and is defined by:

$$T_c = T + \frac{G(T, p) \times (S - 1) L_d}{\kappa} \quad (2.15)$$

in which $G(T, p)$ is the thermodynamics function, S is the dimensionless hydrometeor shape parameter and κ is the air thermal diffusivity.

The equation for F_2 is given by:

$$F_2 = \frac{\kappa}{p} (T_{ac} - T_c) \quad (2.16)$$

in which p is the atmospheric pressure in hPa and T_{ac} is air temperature in °C.

$$f_i = \frac{0.4 \left[1 + 1.45K_n + 0.4K_n \exp\left(-\frac{1}{K_n}\right) (\kappa + 2.5K_n\kappa_a) \right]}{(1 + 3K_n)(2\kappa + 5\kappa_a K_n + \kappa_a)} \quad (2.17)$$

where κ_a thermal conductivity of aerosol in $\text{Jm}^{-1}\text{s}^{-1}$ and K_n is the Knudsen number and is defined as :

$$K_n = \frac{\lambda_{a0} T p_0}{T_0 p r_a} \quad (2.18)$$

Where $\lambda_{a0} = 6.6 \times 10^{-8} m$ is the mean free path at reference temperature $T_0 = 293.12$ K and reference pressure $p_0 = 101325$ Pa and r_a is the aerosol radius.

Finally ψ_a is the aerosol diffusivity and is defined by

$$\psi_a = \frac{kT_c}{6\pi r_a \mu_a} (1 + K_n) \quad (2.19)$$

where μ_a is the dynamic viscosity of air.

The total primary ice nucleation concentration, N_{total} , is given by:

$$N_{total} = \min \left(N_{max}, N_{deposition} + N_{contact} \right) \quad (2.20)$$

2.2 Experiment configuration

2.2.1 Simulation domain

GEMCLIM is a limited area model, which means the simulation domain does not cover the entire Earth's surface. In this study, the integration domain is rectangular (9100 km x 7700 km) and is centred over the Arctic. It covers all areas north of 50°N including the Arctic Ocean, the North Atlantic and Pacific Oceans, most of Europe, Northern Asia, Iceland, Greenland, Siberia and Northern Canada (see Figure 2.1).

A horizontal resolution of 0.25° was adopted. The simulation domain contains 364 grid points in the x-direction and 308 grid points in the y-direction including a 12-points sponge zone. Results are analysed on a sub-domain of 8500 km x 7100 km to eliminate the twelve-grid point pilot of the domain boundaries. The simulations are

performed with a total of 53 vertical levels from 1000 hPa to 10 hPa with the highest resolution in the lower levels.

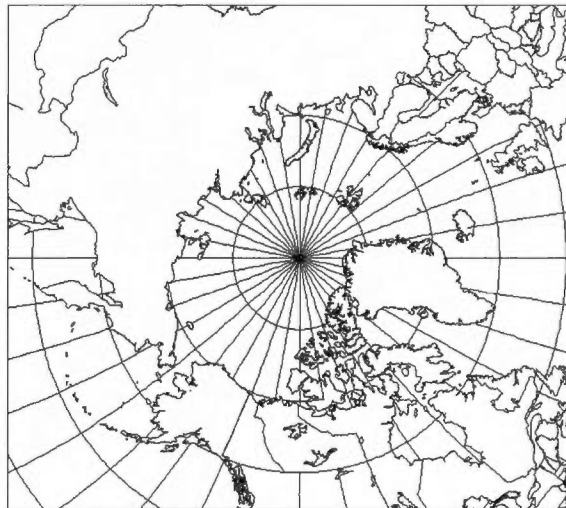


Figure 2.1: Domain of integration by GEMCLIM model, including dominant sources of anthropogenic sulfate in winter.

It is noteworthy to mention that all the experiments are done over a mask applied on the domain above. This mask is limited over the Arctic sea ice boundaries. This mask is used to avoid regions with temperatures too warm (for instance over the free water) not relevant for our study.

2.2.2 Initial conditions at the boundaries

Since GEMCLIM is a limited area model, boundary conditions are required for the integration. The initial and lateral boundary conditions of the domain are initialized at the surface at $t = 0$ and are provided by the European Centre Meteorological Weather Forecasting Centre (ECMWF) analysis data. The analyzed fields are available on 18 pressure levels (1000, 925, 850, 775, 700, 600, 500, 400, 300, 250, 200, 150, 100, 70, 50, 30, 20 and 10 hPa) on a longitude/latitude grid with a 2° by 2° spatial resolution at every six hour (i.e. at 00, 06, 12 and 18 UTC). The

variables are then interpolated to the GEMCLIM grid. Sea ice and sea surface temperature are from AMIP2 (*Atmospheric Model Intercomparison Project*) (Hurrell *et al.*, 2008). They are available on a grid at a horizontal resolution of 1° by 1°. They are then interpolated to the GEMCLIM grid.

2.2.3 Ensemble techniques and statistical analysis

According to Rinke and Dethloff (2000) and Rinke *et al.* (2004), the Arctic is characterized by large values for internal variability due to the pronounced sensitivity of Arctic atmospheric simulations to uncertainties in initial and boundary conditions with the high horizontal resolution regional climate model. This effect is amplified during the cold season when the atmospheric circulations over the Arctic are stronger.

According to Stefanof (2007) study on the sensitivity of Arctic climate on the dehydration-greenhouse feedback, the evolution in external forcing, called signals, due to the evolution of some natural forces (solar radiation, volcanic aerosols, etc...) or anthropogenic factors (increased concentration of greenhouse gases or aerosols, etc...) could be a source of climate variation in regional climate models. It is therefore important to take into account this pronounced magnitude of internal variability in the model. To do so, the technique of ensemble of several simulations is used. This technique allows distinguishing the anthropogenic forcing "signal" from the "noise" produced by the internal variability of the simulated system. The noise is reduced by increasing the number of simulations (IPCC, 2001).

The ensemble technique consists of taking the average of several runs of the same scenario and perturbing the initial conditions between each simulation following Rinke and Dethloff (2000). This technique is used to estimate the magnitude of the internal variability of the model.

In our experiments, each aerosol scenario is investigated with 10 simulations (ensemble), each one with a 12-hour temporal lag in initial conditions with respect to the previous simulation. The start date of the first simulation is on December 1st, 2006 at 00 UTC. This also changes the spin-up period for each of the ensemble members depending on the simulation start date (see table 2.1).

Table 2.1: Periods of integration for all simulations. Mentioned are the beginning and end of each simulation, spin-up duration and the analysis period considered for all simulations

Simulation number	Simulation start date	Simulation end date	Spin-up period	Analyse period
1	01/12/2006 at 00 UTC	31/01/2007 at 00 UTC	30 days	01/01/2007 at 00 UTC to 31/01/2007 at 00 UTC
2	01/12/2006 at 12 UTC		29 ½ days	
3	02/12/2006 at 00 UTC		29 days	
4	02/12/2006 at 12 UTC		28 ½ days	
5	03/12/2006 at 00 UTC		28 days	
6	03/12/2006 at 12 UTC		27 ½ days	
7	04/12/2006 at 00 UTC		27 days	
8	04/12/2006 at 12 UTC		26 ½ days	
9	05/12/2006 at 00 Z UTC		26 days	
10	05/12/2006 at 12 UTC		25 ½ days	

The internal variability of the model is defined by the variance between each ensemble member and its average. Consider $X_{i,j,k}$ to be the magnitude of the variable X from the k^{th} run of ensemble of n simulations at grid point (i,j) where i and j are the horizontal indices.

The mean of the ensemble of n simulations for the variable X over grid point (i,j) , $\bar{X}_{i,j}$, is calculated according to the equation below (Champigny, 2008):

$$\bar{X}_{i,j} = \frac{\sum_{k=1}^n X_{i,j,k}}{n} \quad (2.21)$$

Having this mean value from the equation (2.21), one can calculate the unbiased sample variance ($s_{i,j}^2$) of n simulations by the following equation. The variance represents the internal variability of the variable $X_{i,j}$ at the grid point (i, j) :

$$s_{i,j}^2 = \frac{\sum_{k=1}^n (X_{i,j,k} - \bar{X}_{i,j})^2}{n-1} \quad (2.22)$$

We can then calculate the spatial mean of the $s_{i,j}^2$ for all the grid point by the following equation:

$$s^2 = \frac{\sum_{i=1}^{N_x} \sum_{j=1}^{N_y} s_{i,j}^2}{N_x \cdot N_y} \quad (2.23)$$

The objective is to converge the ensemble variance, s^2 , to the true population variance after n simulations indicating the stabilization of the internal variability of the model. According to Champigny (2008), the variance converges into a fixed value as the number of simulations in an ensemble approaches to five.

2.3 Statistical analysis of the results (Student's t-test)

One of the major problems in the study of stochastic systems is the identification of statistically significant area; this is defined as the area in the domain in which the difference between means of a given variable in both scenarios is significant to a desired confidence level.

To determine these areas, one needs to perform a statistical test for the difference between two independent populations (reference and perturbed) from which a sample is taken. It is assumed that each population is characterized by a normal distribution.

The statistical test allows us to provide a non-zero signal with a desired confidence level. This non-zero signal is produced by reducing the concentration of ice nuclei. Indeed, the difference between the two cases (reference and perturbed) is partly caused by internal variability of the model and partly by the reduction in ice nuclei number concentration (Champigny, 2008).

The confidence on difference of a given field from two scenarios over the entire domain is evaluated using the student t-test with a desired confidence level. The statistical test is described in Appendix B.

2.4 Sensitivity study

In this study, the sensitivity study consists of comparing six ensembles (each associated with an aerosol scenario) of ten simulations for January 2007, two by two, to verify the sensitivity of wintertime Arctic clouds and radiation to contact nucleation, air acidification and the contact angle.

Table 2.2 shows the aerosol scenarios and their associated acronym. The first set consists of simulations in non-polluted air with a constant contact angle set to 12° in which the concentration of contact INs is non-zero (NAT1). The second set consists of simulations in non-polluted air in the absence of contact freezing in which contact angle is set to 12° (NAT2). The third scenario differs from the second by the fact that the contact angle is not constant anymore but varies according to a PDF distribution as discussed in section 1.2.2. The fourth set of simulations corresponds to acid polluted episode of Arctic air in the presence of contact nucleation in which contact angle is set to 27° (AC1). The fifth aerosol scenario corresponds to acid polluted episode in which the contact nucleation is excluded from the microphysics scheme (AC2) and finally the sixth set of simulations corresponds to non-polluted air mass with the presence of contact freezing in which the contact angle is distributed according to a normal distribution probability function (AC3).

Table 2.2: Introduction of six aerosol scenarios to check the Arctic climate sensitivity

NAT1	Non-acid with contact ($\alpha = 12^\circ$)
NAT2	Non-acid without contact ($\alpha = 12^\circ$)
NAT3	Non-acid without contact (α -PDF)
AC1	Acid with contact ($\alpha = 27^\circ$)
AC2	Acid without contact ($\alpha = 27^\circ$)
AC3	Non-acid with contact (α -PDF)

Subsequently, comparing these sets of simulations two by two, allows analyzing the impact of the parameterisation changes on the cloud microstructure and radiative forcing over the Arctic during January 2007. The Table 2.3 shows the components of each pair and its related anomaly when the anomaly is defined as the difference between two scenarios of each pair.

Table 2.3: Introduction of the components of six pairs to check the Arctic climate sensitivity

Pairs	Involved aerosol scenarios	Pair Anomaly
Pair 1	AC1 and NAT1	AC1-NAT1
Pair 2	AC3 and NAT1	AC3-NAT1
Pair 3	NAT1 and NAT2	NAT1-NAT2
Pair 4	AC1 and AC2	AC1-AC2
Pair 5	AC2 and NAT2	AC2-NAT2
Pair 6	AC3 and NAT3	AC3-NAT3

CHAPTER III

RESULTS

3.1 Model validation

Model validation, which includes the comparison of model simulations with analysis data, is an essential step to verify how accurate the model is capable of reflecting the real atmospheric processes. In other words, the validation ensures how precisely the model predictions match the experimental data and the observations.

Here the important atmospheric fields chosen to verify the model are the sea level pressure, the temperature at 850 hPa and the geopotential height at 500 hPa. In fact the ensemble mean of each field averaged for January 2007 are compared to January averaged observational data from ECMWF analysis.

Figure 3.1 shows the difference of geopotential height at 500 hPa, the MSLP and the temperature at 850 hPa between the ECMWF analysis and the model output for the NAT1 aerosol scenario averaged on January 2007 over the Arctic. The averaged values of differences of these fields with the ECMWF analysis over the Arctic for the aerosol scenario NAT1 are found in table 3.1. Since the NAT1 scenario is quite representative of the other aerosol scenarios, only the NAT1 validation is shown here. Validation of the other aerosol scenarios for the same variables can be found in Appendix A.

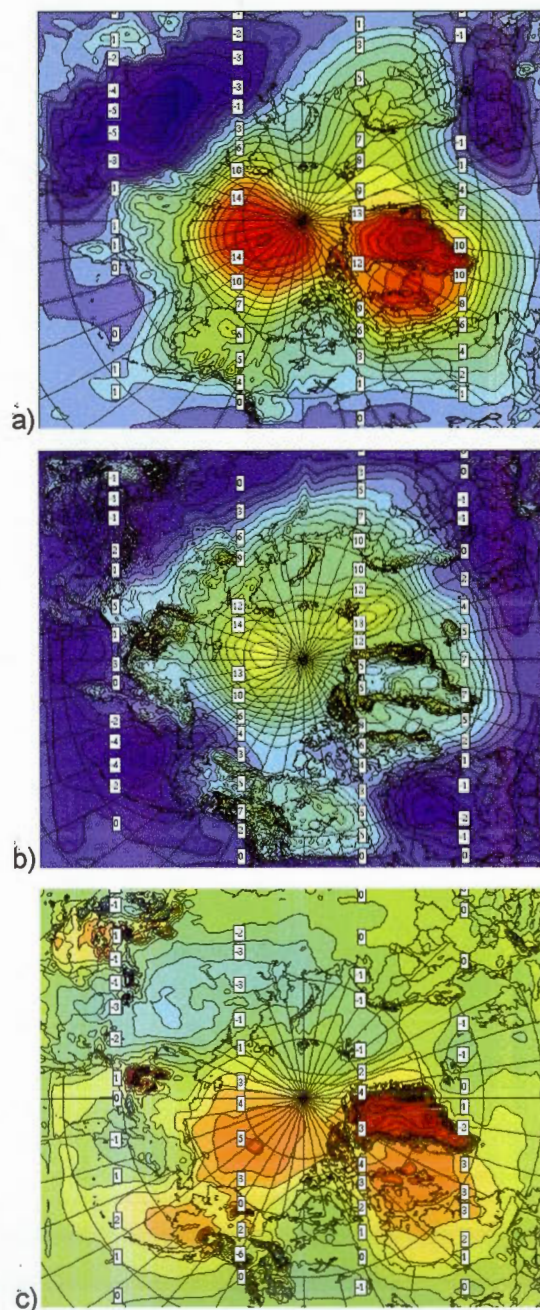


Figure 3.1: The differences of (a) geopotential height at 500 hPa (dam), (b) MSLP (hPa), (c) temperature ($^{\circ}\text{C}$) at 850 hPa between the observations from ECMWF and GEMCLIM simulations averaged over January 2007 for aerosol scenario NAT1.

Table 3.1: The mean January differences of geopotential height at 500 hPa, the MSLP and the temperature at 850 hPa with the ECMWF analysis averaged over the Arctic for aerosol scenario NAT1

NAT1	Analysis mean	Model output mean	Difference mean
Sea level pressure (hPa)	1009	1012	3.58
Temperature at 850 hPa (°C)	-12.79	-12.1	-0.43
Geopotential at 500 hPa (dam)	521	524	3

For the NAT1 aerosol scenario, the mean difference of geopotential height at 500 hPa with ECMWF analysis is 3 dam. This difference is overestimated over a significant part of the Arctic including the Greenland, Greenland Sea, Norwegian Sea and North Arctic ocean peaking at the Greenland with a maximum up to 18.3 dam. This difference is also negative over Siberia and the North Sea with a minimum of -6.8 dam scenario over Siberia. The results are consistent to the one obtained by Girard *et al.* (2012) with the over-estimation over Greenland and North Arctic ocean and the under-estimation over Siberia. However the model has larger bias in January compared to January-February of Girard *et al.* (2012) that ranges between -4 to 4 dam.

As for the temperature field at 850 hPa in the NAT1 aerosol scenario, the differences between the model output and the analysis from ECMWF for January 2007 vary generally between 2 and -2 °C over a vast area in the Arctic with a spatial average of 0.64 °C. However, the temperature at 850 hPa is underestimated locally over Siberia with a minimum value of -11.3 °C. According to Champigny (2008), this error in local temperature simulation is related to the variation in the daily ice over. Also the difference is overestimated over a large area in the Arctic including Greenland, Arctic Ocean and North of East Siberian Sea with its peak over Greenland ranging from equal to 10.4 °C. The difference values are consistent with the geopotential height bias over the same area.

The MSLP for January 2007 is underestimated compared to ECMWF analysis by 5 hPa over the Bering Sea. It is also overestimated over the Greenland Sea, Laptev Sea, East Siberian Sea, Barents Sea, Kara Sea and the Arctic Ocean with values up to 16 hPa. However, the MSLP overestimation larger than 16 hPa is found over Greenland and Siberia caused by the topography and the model extrapolation in sea level pressure calculation. Except regions mentioned for overestimation and underestimation, the mean sea level pressure is reproduced quite well by the model with values ranging from -2 to 5 hPa.

It is noteworthy to mention that since this is the anomaly of the scenarios in the pairs that is important to us and make the basis of this study, the error by the model do not have any effect in this study.

3.2 Comparison of the aerosol scenarios

3.2.1 Comparison of AC1 and NAT1 (Pair 1)

In this section, the sensitivity of Arctic cloud and radiation to the presence of the sulfuric acid coated INs is examined using the GEM-LAM climate model for January 2007 over the Arctic.

According to the mean sea level pressure pattern for January 2007 in the Arctic (see Figure 3.2), the presence of an intense low-pressure system over the North Atlantic and an anticyclone over Siberia favors the formation of storms that cause strong upper-level winds blowing from the mid-latitudes to the North Pole. This large-scale circulation favors the transport of anthropogenic aerosols from industrial regions of Eurasia to the Arctic. The Aleutian cyclone also provides a pathway for the transport of anthropogenic aerosols emitted over East Asia to the Arctic.

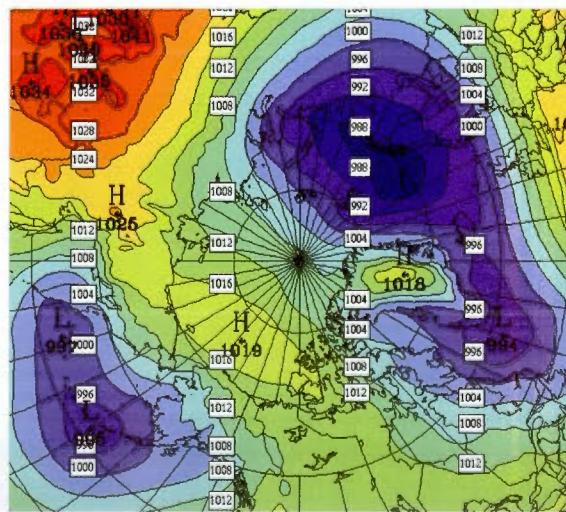


Figure 3.2: The MSLP from ECMWF analysis averaged over January 2007.

Figure 3.3a and b show the vertical profiles of ice water content and ice crystal number concentration for aerosol scenarios NAT1 and AC1 spatially averaged over

a mask delimited by sea ice boundaries. As a result of the more frequent clear sky precipitation in the AC1 aerosol scenario, the ice mixing ratio and ice crystal concentration is smaller compared to the uncoated NAT1 scenario throughout the troposphere. According Archuleta (2005), a proportion of acid coated aerosol to the total aerosol mass of 20%, increases the clear air precipitation by 50%. According to the explanation given in Chapter I, the decreased heterogeneous nucleation rate of ice crystals caused by acid coated aerosols changes the ice formation process and the microstructure of Arctic clouds in the polluted air mass. In fact, the decreased nucleation rate at the cloud levels leads to the formation of relatively fewer ice crystals that grow to larger sizes. On the other hand, since more water vapor is available in the atmosphere for each crystal, the crystals grow even bigger in the polluted air mass and precipitate more efficiently from the cloud levels. This phenomenon is generally called clear sky precipitation or diamond dust.

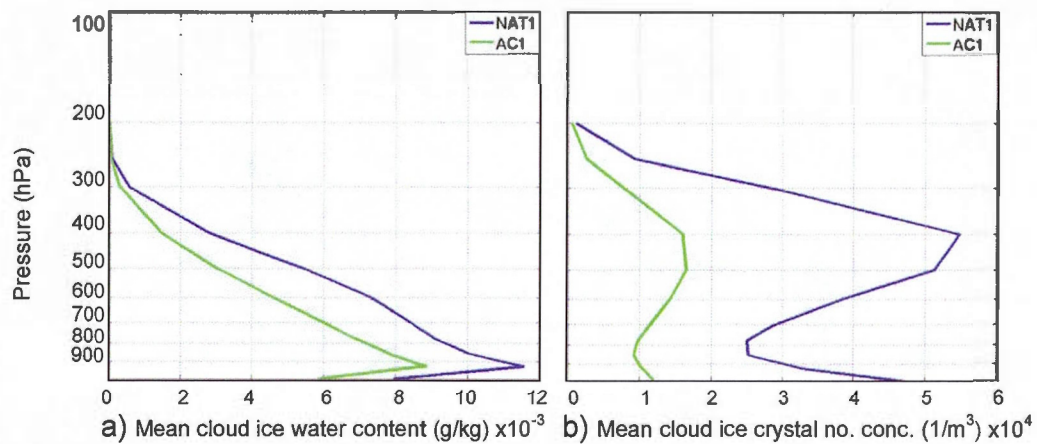


Figure 3.3: Vertical profiles of cloud (a) ice water content ($\times 10^{-3}$ g/kg) and (b) ice crystal number concentration ($\times 10^4$ $1/m^3$) for aerosol scenarios NAT1 and AC1 averaged over time and spatially averaged over a mask delimited by sea ice boundaries.

Figure 3.4a and b show the vertical profiles of liquid water content and droplet number concentration for aerosol scenarios NAT1 and AC1 averaged over the sea ice boundaries mask. The liquid water mixing ratio and water drop concentration are larger in the AC1 scenario compared to the uncoated NAT1 scenario throughout the

troposphere. The reduced concentration of ice crystals in the mixed-phase clouds in aerosol scenario AC1 reduces the evaporation rate of water droplets. Indeed, in the AC1 scenario, the Bergeron effect (evaporation of liquid water droplets followed by the deposition of water vapor on ice crystals) is limited by the smaller deposition rate of water vapor onto ice crystals, which are in much smaller concentration in the AC1 aerosol scenario. Therefore in the polluted air mass, the mixed-phase clouds are more frequent with a frequency between 30 to 50% (Girard *et al.*, 2012).

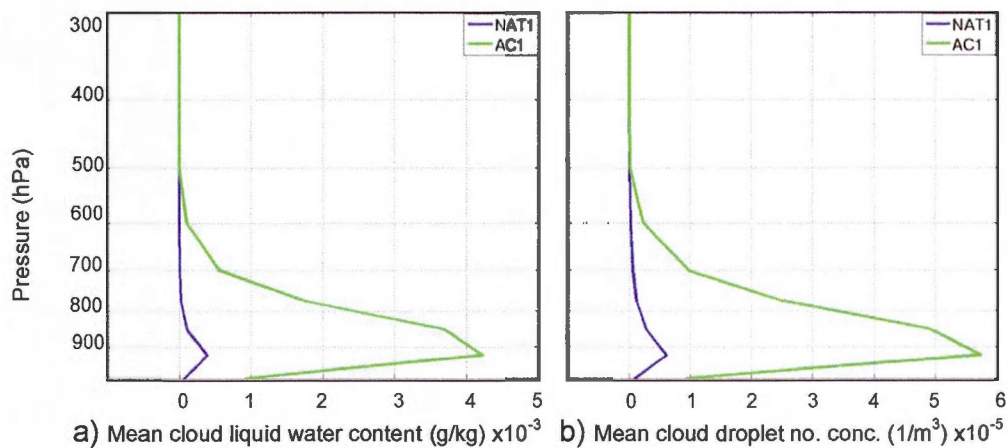


Figure 3.4: Vertical profiles of cloud (a) liquid water content ($\times 10^{-3} \text{ g/kg}$) and (b) liquid drop number concentration ($\times 10^5 \text{ 1/m}^3$) for aerosol scenarios NAT1 and AC1 averaged over time and spatially averaged over a mask delimited by sea ice boundaries.

Figure 3.5 shows mean January mean ice water path and liquid water path anomaly in the Arctic. The liquid water path anomaly is almost positive everywhere over the Arctic with values generally ranging between 0 and 0.05 kg/m^2 and peaking at 0.2 kg/m^2 at Perry Island. The ice water path anomaly is almost negative everywhere over the Arctic with values varying between 0 and -0.3 kg/m^2 and is positive over very small regions over western and south eastern Greenland with a maximum value of 0.03 kg/m^2 . As expected, the results show a decrease in ice water path of -0.0155 kg/m^2 and an increase of 0.0079 kg/m^2 in liquid water path in AC1 aerosol scenario compared to NAT1 scenario averaged over the sea-ice mask.

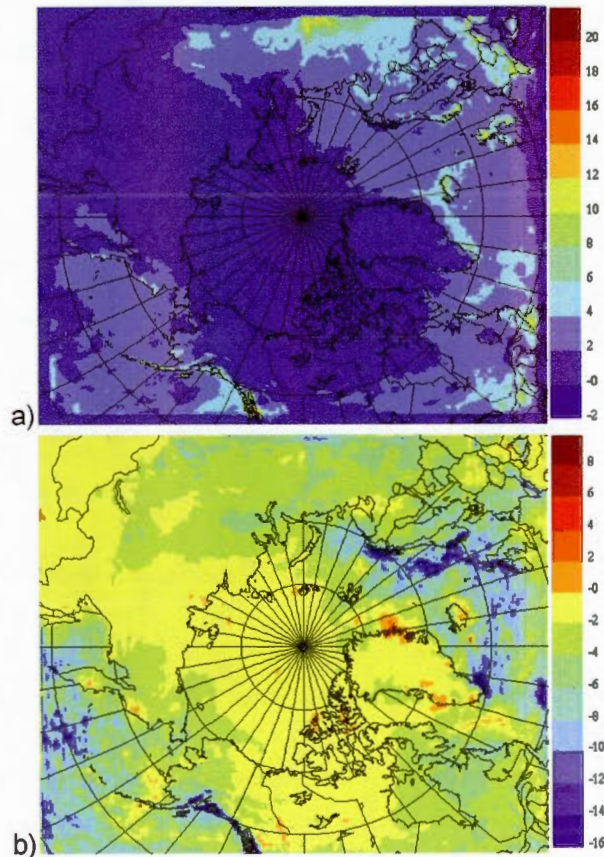


Figure 3.5: January mean (a) liquid water path anomaly ($\times 10^{-2}$ mm) and (b) ice water path anomaly ($\times 10^{-2}$ mm) in the Arctic when the anomaly is defined as the difference between AC1 and NAT1 (AC1-NAT1).

The reduced ice crystal number concentration in AC1 scenario reduces the total deposition of water vapor on the cloud ice crystals. This phenomenon increases the relative humidity with respect to ice in the polluted scenario (AC1). As shown in Figure 3.6., results show January mean positive RH_i anomaly of 6.5 % at 850 hPa averaged over the mask delimited by sea ice boundaries. Figure 3.6b shows that the RH_i anomaly is maximum over the coldest regions of the Arctic during the winter mainly north of 80°N . This result was somewhat expected since the ratio of saturated vapour pressure over liquid water and over ice increases as the temperature decreases. Therefore, for the same relative humidity with respect to liquid water, RH_i increases as the temperature decreases.

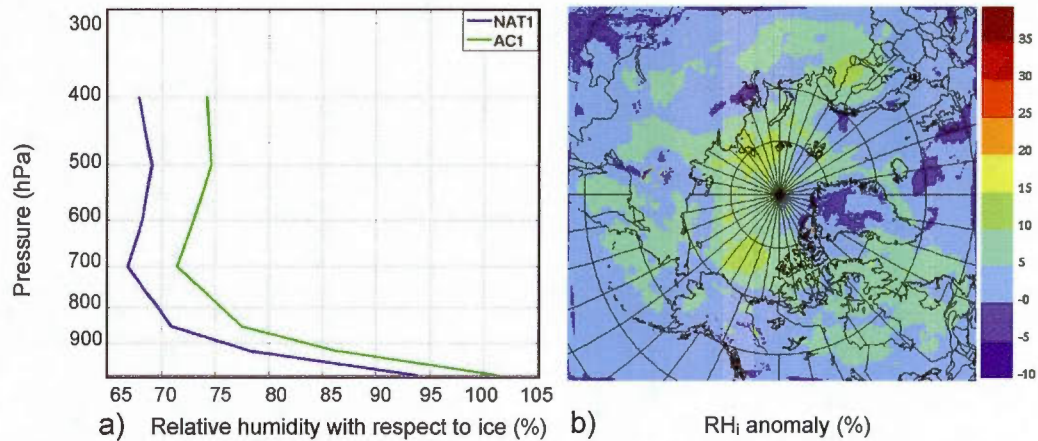


Figure 3.6: January 2007 mean RH_i (%) (a) vertical profile averaged over a mask delimited by sea ice boundaries and (b) anomaly at 850 hPa for aerosol scenarios NAT1 and AC1 when the anomaly is defined as the difference between AC1 and NAT1 (AC1-NAT1).

Figure 3.7a and b show the CRF anomaly at the surface and at the TOA over the Arctic in January 2007. Based on the dependency of the cloud forcing to the tropospheric hydrometeor content, the reduction of the cloud optical thickness reduces the downwelling IR radiation to the surface resulting in a mean negative cloud forcing of -0.8 W/m^2 at the surface averaged over sea-ice boundaries. The decreased ice water path and the increased frequency of mixed-phase cloud in the acid coated aerosol scenario reduce the thickness over which the mid and high ice clouds act as blackbody objects. The optically thinner and more transparent high and mid clouds formed in the polluted environment of the AC1 scenario ensure more IR radiation leaving the high troposphere producing a mean negative cloud forcing anomaly at the top of the atmosphere of -3.15 W/m^2 averaged over the sub domain delimited by the sea-ice boundaries. These results are consistent with the negative cloud forcing at the TOA obtained by Girard *et al.* (2012) in a similar study.

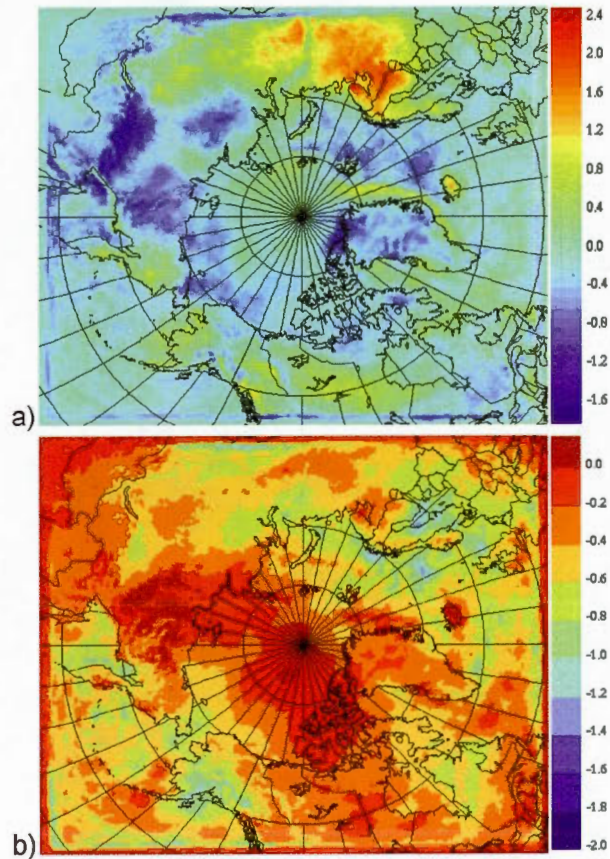
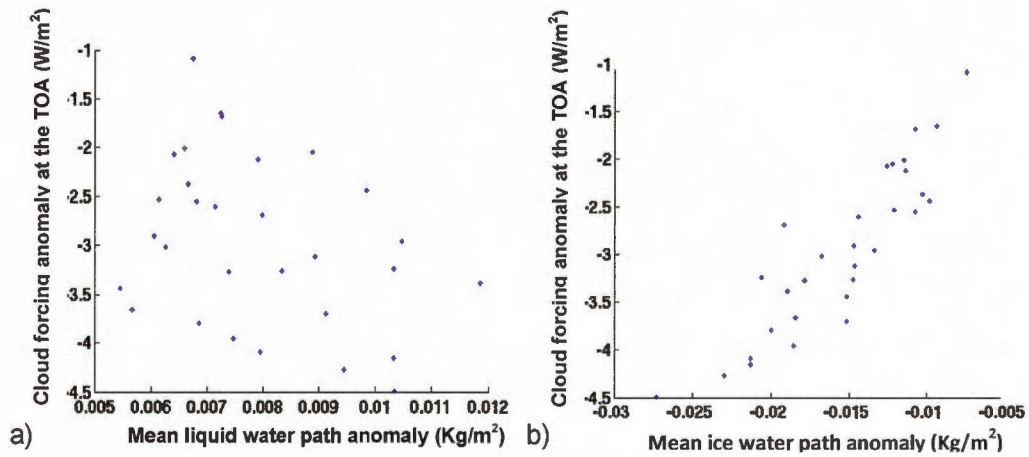


Figure 3.7: Mean January 2007 cloud forcing anomaly ($\times 10 \text{ W/m}^2$) at (a) the surface and at (b) the TOA over the Arctic when the anomaly is defined as the difference between AC1 and NAT1 (AC1-NAT1).

Figures 3.8a and b show the co-variation of the daily mean cloud forcing anomaly of at TOA as a function of respectively daily mean vertically integrated liquid water path anomaly and ice water path anomaly averaged over the sub-domain delimited by sea ice. As expected, the absolute value of CRF anomaly at TOA increases by the increase in the absolute value for ice and liquid water path anomaly.



Figures 3.8: Pair 1 scatter plot of the daily mean cloud forcing anomaly (W/m^2) of January 2007 at TOA as a function of daily mean vertically integrated (a) liquid water path anomaly (Kg/m^2) and (b) ice water path anomaly (Kg/m^2) averaged over the sub-domain delimited by sea ice when the anomaly is defined as the difference between AC1 and NAT1 (AC1-NAT1).

Figure 3.9a and b show the mean January temperature vertical profile over the sub-domain delimited by sea-ice boundaries. A negative temperature anomaly over a vast area of the Arctic is obtained.

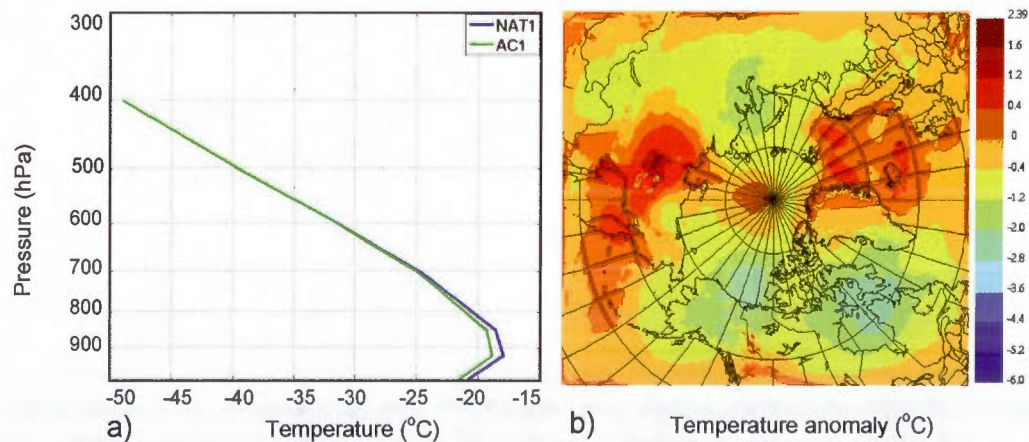


Figure 3.9: January 2007 mean temperature ($^{\circ}\text{C}$) (a) vertical profiles (b) anomaly at 850 hPa averaged over a mask delimited by sea ice boundaries for aerosol scenarios NAT1 and AC1 when the anomaly is defined as the difference between AC1 and NAT1 (AC1-NAT1).

As shown in the table 3.2, the results show a mean cooling of -0.9°C at 1000 hPa, mean cooling of -0.78°C at 850 hPa and a mean cooling of -0.006°C at 500 hPa averaged over the sea-ice mask. This result is consistent with Girard *et al.* (2012) with a cooling up to -3°C near the surface and cooling values ranging from -2°C to -4°C at 850 and 500 hPa.

Table 3.2: Pair 1 temperature anomaly at 1000, 850 and 500 hPa and cloud forcing anomaly at TOA and surface at the surface averaged over the sub-domain delimited by sea-ice boundaries

Mean CRF anomaly at surface (W/m^2)	-0.8
Mean CRF anomaly at TOA (W/m^2)	-3.15
Mean temperature anomaly 1000 ($^{\circ}\text{C}$)	-0.89
Mean temperature anomaly 850 ($^{\circ}\text{C}$)	-0.78
Mean temperature anomaly 500 ($^{\circ}\text{C}$)	-0.006

Previous studies and observations have also shown an intensification of the surface-based temperature inversion as obtained in our study. Based on study on temperature vertical profiles of 27,000 cases during the years 1950 to 1990 during the Arctic winter, Kahl *et al.* (1993) showed that the temperature inversion of the Arctic air mass has strengthened with a mean -2°C cooling at the surface and a mean 2°C rise in temperature at high altitudes. Another research conducted by Stefanof (2007) suggests a surface cooling of -3.3°C over the central Arctic due to the DGF effect. This cooling produces a horizontal temperature gradient between the North Pole and mid-latitudes which potentially intensifies the atmospheric circulation and the pollution transport toward the Arctic.

One may argue that obtained results of the cloud microstructure change could be linked to temperature or RH_i changes in our simulations. Figures 3.10 shows the graphs of ice crystal number concentration and liquid drop number concentration anomaly as a function of RH_i and temperature anomalies. Results show that the liquid drop concentration anomaly increases and the ice crystals concentration anomaly decreases in the troposphere regardless of temperature and RH_i anomaly

signs suggesting that these anomalies are caused by the decrease in the INs concentration and are independent to the RH_i and temperature changes in the troposphere.

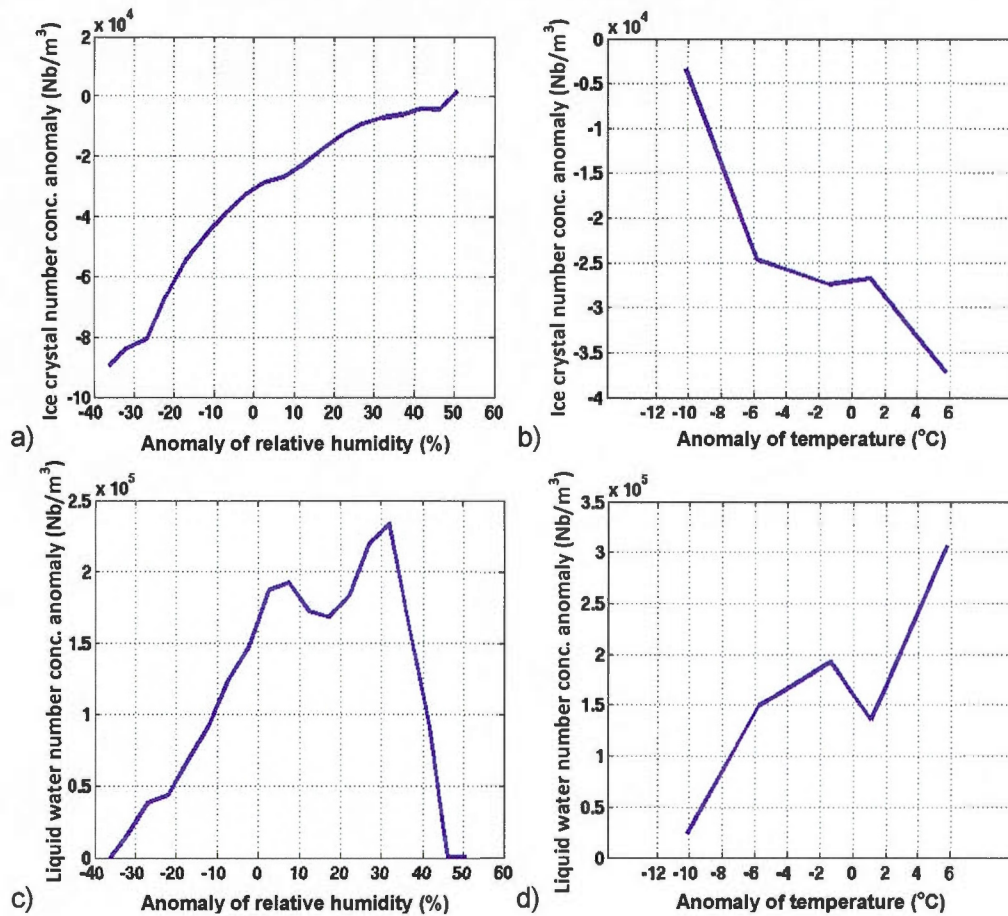


Figure 3.10: January daily mean of (a,c) ice crystal number concentration ($1/m^3$) and water drop concentration ($1/m^3$) anomalies as a function of RH_i (averaged over 5% intervals) and (b,d) temperature (averaged over 5 K intervals) anomalies spatially averaged over a mask delimited by sea ice boundaries when the anomaly is defined as the difference between AC1 and NAT1 (AC1-NAT1).

3.2.2 Comparison of AC3 and NAT1 (Pair 2)

In this section, the effects of the PDF representation of the contact angle on the cloud properties are investigated. The probability density function distribution used in this study is based on laboratory experiments of Wheeler and Bertram (2011). The PDF is a Gaussian distribution with a contact angle median value of 18.7° and a standard deviation of 5° . In the model, the PDF is discretized with 29 contact angles that increase from 4.9° to 33.2° . This parameterization of contact angle is compared to the original CNT framework with a single contact angle value of 12° .

According to Kulkarni (2012), the required onset RH_i value for ice nucleation on dust particles in the deposition mode highly depends on the contact angle. The lower the contact angle, the lower the required onset RH_i for nucleation initiation. Based on this fact, the frozen fraction value changes with contact angle in the PDF representation of ice nucleation, i.e. the deposition nucleation is more efficient for dust particles with smaller contact angles.

Kulkarni (2012) also suggests that in the single contact angle approach, the nucleated fraction jumps from zero at low relative humidity to the maximum value at onset RH_i value in a step-like function whereas in the PDF distribution approach, the non-zero nucleated fraction increases gradually as RH_i increases. Therefore, because of the wide range of contact angles from 4.9° to 33.2° in the AC3 scenario, ice crystals nucleate at almost all magnitudes of RH_i but in the single contact angle approach, the INs trigger nucleation only after the RH_i reaches the threshold value for ice nucleation. One therefore expects that the nucleation of ice crystals in the AC3 scenario will be much more progressive.

Figure 3.11 shows the spatial (over the sea ice mask) and temporal means ice crystal water content and number concentration vertical profiles simulated by the AC3 and the NAT1 aerosol scenarios. The ice water content and the ice crystal concentration in AC3 scenario are smaller than in NAT1 scenario throughout the

troposphere. Differences reach up to 30% and 50% for the ice water content and ice crystal number concentration respectively. According to the normal probability distribution function (see equation 2.7), the larger the absolute value of the difference between the contact angle and the mean value, $(|\mu-\alpha|)$ is, the smaller the deposition nucleation probability by the IN will be. Therefore in the AC3 scenario, most of the INs have a contact angle equal to 18.7° , which is higher than the fixed contact angle value used in NAT1 scenario ($\alpha=12^\circ$). But since ice nucleation by INs with lower contact angles occurs at lower RH_i values, there is less chance for INs with contact angles equal to 18.7° and higher to nucleate ice crystals. That is why more INs get activated in NAT1 scenario than in AC3 scenario leading to a greater concentration of smaller ice particles in the single contact angle approach of CNT.

Because of the contact angle dependency of IN nucleability to the RH_i value in the AC3 aerosol scenario, the deposition ice nucleation is initiated by INs with smaller contact angles that need relatively lower RH_i values to start ice nucleation. On the other hand, according to the PDF distribution, the number concentration of INs with small contact angles is much lower than number concentration of INs with $\alpha=12^\circ$. Therefore, there is fewer active INs in the AC3 scenario than in the NAT1 scenario. As a result, the relatively big ice crystals formed in the AC3 aerosol scenario precipitate more efficiently from the cloud levels compared to the NAT1 scenario. This explains the smaller ice crystal mixing ratio and ice crystal number concentration in scenario AC3 compared to scenario NAT1.

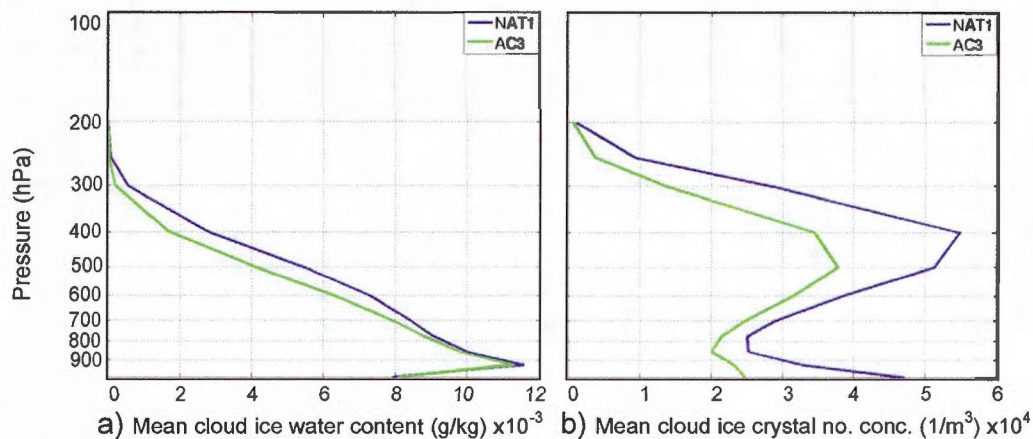


Figure 3.11: Vertical profiles of cloud (a) ice water content ($\times 10^{-3}$ g/kg) and (b) ice crystal number concentration ($\times 10^4$ $1/m^3$) for aerosol scenarios NAT1 and AC3 averaged over time and spatially averaged over a mask delimited by sea ice boundaries.

The decreased ice crystal number concentration in the AC3 scenario leads to the formation of bigger ice crystals when compared to the NAT1 scenario. More water vapor is available to deposit on each ice crystal in the AC3 scenario. Moreover, the fact that ice nucleation is more progressive in the AC3 scenario keeps the RH_i from varying as much as in the NAT1 scenario. Figure 3.12a shows the covariation of ice crystal number concentration with the RH_i and the standard deviation of the former variable for both aerosol scenarios. The standard deviation of the ice crystal concentration is much higher in the NAT1 scenario mainly for the largest ice concentration values. This corresponds to times when the onset RH_i is reached. In NAT1, a large number of ice crystals get nucleated because of the step function nature of the single contact angle approach. The number concentration of ice crystals is much less variable in the AC3 scenario since the ice nucleation is much more progressive.

High amount of water vapor is deposited onto ice crystal in both NAT1 and AC3 aerosol scenarios, but since there are less active INs in AC3 compared to NAT1, the deposition rate of water vapor on the ice crystal in NAT1 is higher than in AC3. Consequently the RH_i in AC3 is higher than in NAT1. Furthermore, the step-

like function of the NAT1 scenario can be seen through the larger standard deviation of RH_i . Indeed, RH_i has to reach higher values in NAT1 compared to AC3 to nucleate ice crystals. Once the large number of ice crystals is nucleated, RH_i goes down to smaller values when compared to the AC3 scenario as shown in Figure 3.12b. The January mean positive RH_i anomaly of 1.18 % at 850 hPa is obtained over the mask delimited by sea ice boundaries in the Arctic.

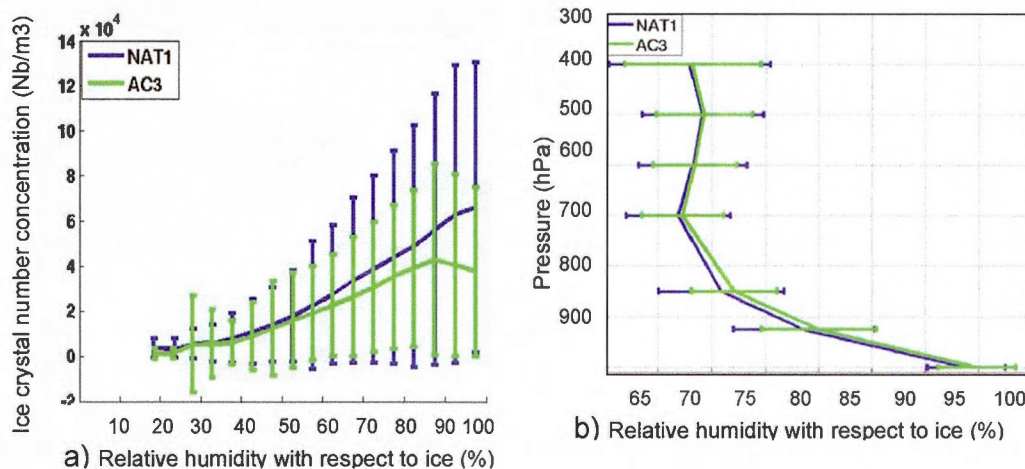


Figure 3.12: January a) daily mean of ice crystal number concentration ($\times 10^4$ $1/m^3$) and b) mean vertical profiles of the mean RH_i (as a function of RH_i averaged over time and spatially averaged over a mask delimited by sea ice boundaries for NAT1 and AC3 while the horizontal bars show the RH_i standard deviation at each pressure level and vertical bars show the ice crystal number concentration standard deviation at related RH_i values in the troposphere.

Figures 3.13a and b show the mean cloud liquid water content and number concentration averaged over the sea ice mask. In the NAT1 scenario, the liquid water content and number concentration is larger compared to the AC3 aerosol scenario with the largest difference near 875 hPa. At these low levels, temperature is relatively warm with values around -15°C . In the NAT1 scenario, the liquid saturation with respect to water is often reached before the ice supersaturation reaches the onset value for ice nucleation. Cloud liquid droplets are then activated instead of ice crystals. In the AC3 scenario, the fact that some ice crystals can nucleate at lower contact angles (in other terms at lower ice supersaturation) (discussed in section

2.1.2.1) prevents the saturation ratio to reach the liquid saturation point. Therefore, the activation of cloud droplets is not as frequent in the AC3 scenario.

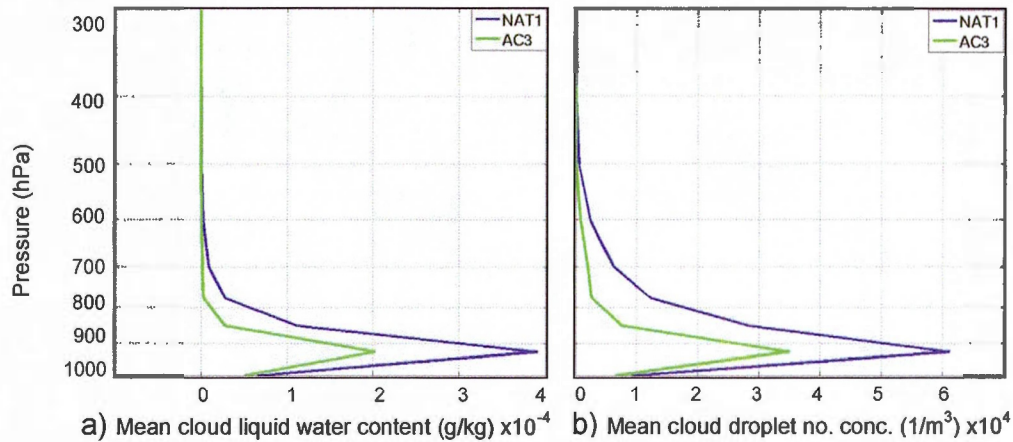


Figure 3.13: Vertical profiles of cloud (a) liquid water content ($\times 10^{-4}$ g/kg) and (b) liquid drop number concentration ($\times 10^4$ $1/m^3$) for aerosol scenarios NAT1 and AC3 averaged over time and spatially averaged over a mask delimited by sea ice boundaries.

The regional distribution of the decrease in ice and the increase in liquid water paths in the AC3 aerosol scenario compared to the NAT1 scenario are shown in Figures 3.14 and b, which show the mean January ice and liquid water path anomaly over the Arctic. The liquid and ice water path anomalies are positive over the Central Arctic, eastern and central Siberia, Northern Greenland, Greenland Sea and Northern Canada and are negative elsewhere over the Arctic with the largest decrease over the Barents Sea. The results give a mean January ice water path anomaly of -0.0027 kg/m^2 and liquid water path anomaly of -0.0002 kg/m^2 averaged over the sea-ice mask.

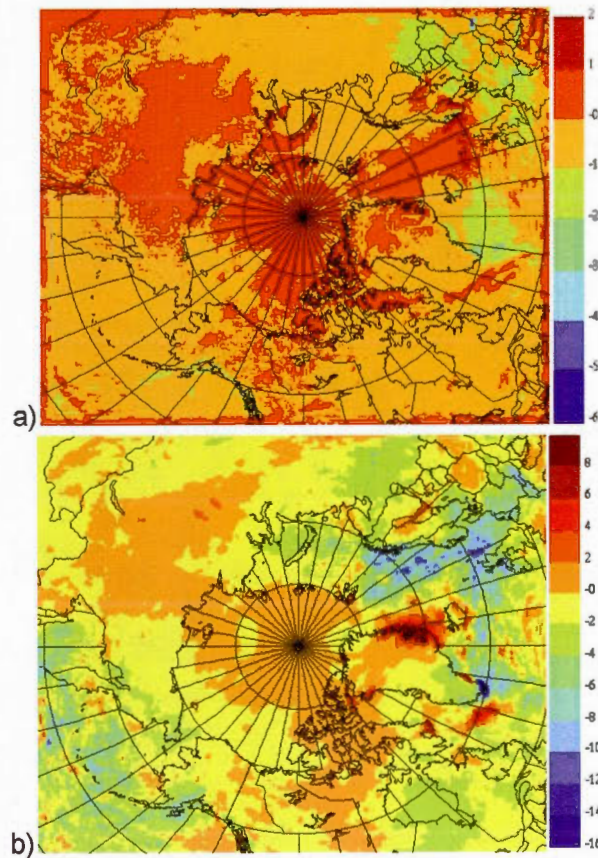


Figure 3.14: January mean (a) liquid water path anomaly ($\times 10^{-2}$ mm) and (b) ice water path anomaly ($\times 10^{-2}$ mm) in the Arctic when the anomaly is defined as the difference between AC3 and NAT1 (AC3-NAT1).

As discussed in section 3.2.1, changes in the cloud microstructure can alter the cloud radiative forcing both at the surface and at the TOA. Figure 3.15a and b show the CRF anomaly at the surface and at the TOA. The CRF anomalies at the surface and at the TOA are positive over the central Arctic, central and eastern Siberia, the north of Greenland and Greenland Sea. The positive CRF anomaly values at the surface and at the TOA range mostly between 0 and 9 W/m^2 and 0 to 6 W/m^2 respectively. Largest CRF anomalies are located over south-eastern Greenland. CRF anomaly at the surface and at the TOA are negative over a vast area of the Arctic including Alaska, eastern, north and north western Siberia, Bering Sea, South and south eastern Greenland, Kara Sea, Bering Sea and Norwegian

Sea. These negative CRF anomalies vary between 0 and -10 W/m^2 at the surface and reach a minimum value of -14 W/m^2 over the Kara Sea. At the TOA, these negative CRF anomalies mostly vary from 0 to -8 W/m^2 and reach a minimum value of -8.8 W/m^2 over north-western Siberia. A mean decrease of ice crystal and droplet concentrations in AC3 due to the PDF parameterisation of contact angle decrease the CRF at the surface and at TOA with a mean value of -0.83 W/m^2 and -0.69 W/m^2 respectively over the sub-domain delimited by sea ice. It should be noted that most CRF anomalies at the surface and TOA are not statistically significant (see Figures D.7 and D.8 in appendix D). However, few places that are statistically significant indicate negative CRF anomalies, which is consistent with the IWP and LWP anomalies.

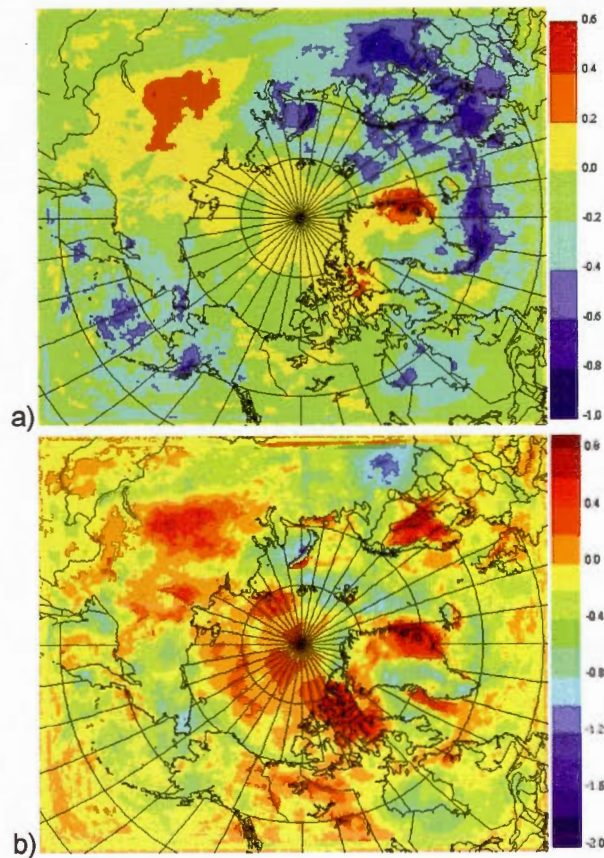
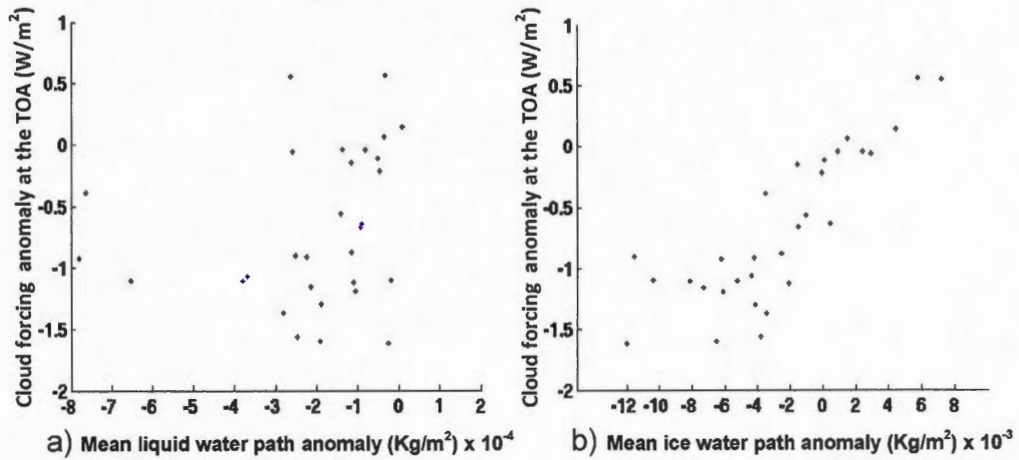


Figure 3.15: January 2007 cloud forcing anomaly ($\times 10^3 \text{ W/m}^2$) at (a) the TOA and (b) the surface for the pair 2 when the anomaly is defined as the difference between AC3 and NAT1 (AC3-NAT1).

Figures 3.16a and b show the co-variation of CRF at TOA as a function of vertically integrated ice and liquid water paths. The negative cloud forcing anomaly at TOA decreases as the ice water path decreases in the clouds while it does not depend to the liquid water path in the troposphere suggesting that the liquid water path in the clouds is higher than 15 g/m^2 in both scenarios of the pair 2. At this point the clouds emit as blackbody and any change in the water content do not affect the cloud forcing at the surface.



Figures 3.16: Pair 2 scatter plot of the daily mean cloud forcing anomaly (W/m^2) of January 2007 at TOA as a function of daily mean vertically integrated (a) liquid water path anomaly ($\times 10^{-4} \text{ Kg/m}^2$) and (b) ice water path anomaly ($\times 10^{-3} \text{ Kg/m}^2$) averaged over the sub-domain delimited by sea ice when the anomaly is defined as the difference between AC3 and NAT1 (AC3-NAT1).

Figure 3.17 shows the mean January temperature anomaly at 850 hPa over the Arctic. The temperature anomaly is positive over the central Arctic Ocean, eastern Siberia, North and east of Greenland, Bering Sea, Greenland Sea, Norwegian Sea and central Arctic with values ranging mostly from 0 to 1 K and is negative most of the places north of 70°N with values ranging for 0 to -2 K and a minimum of -3.3 K over South-western Greenland. The regions with positive/negative temperature anomaly match to a great extent to the regions where CRF anomaly at the TOA or at the surface is positive/negative shown in Figures 3.15a and b.

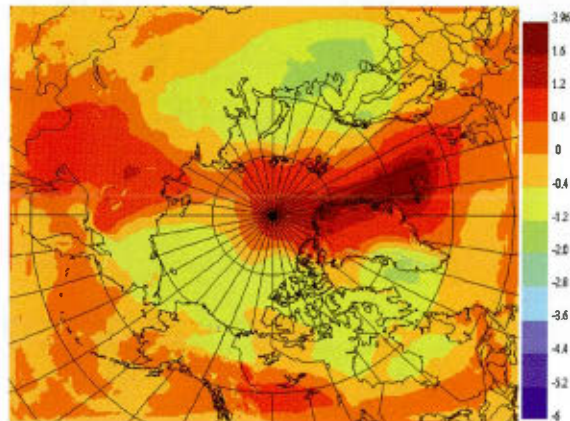


Figure 3.17: Mean January temperature anomaly over the Arctic at 850 hPa when the anomaly is defined as the difference between AC3 and NAT1 (AC3- NAT1).

Figure 3.18 shows the mean January vertical profile of the temperature of spatially averaged over the sea-ice mask for the AC3 and NAT1 aerosol scenarios. The temperature vertical profile in both AC3 and NAT1 are very close to each other. This shows that despite the positive and negative regional temperature anomalies over the Arctic, the spatially averaged temperature anomaly over the whole Arctic is somewhat small with values between -1 K and 0 K.

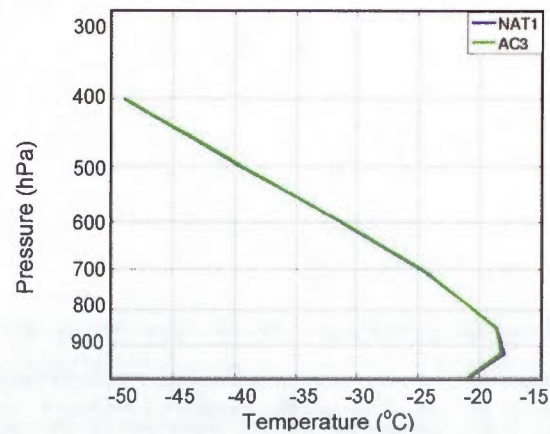


Figure 3.18: January 2007 mean temperature ($^{\circ}\text{C}$) vertical profiles averaged over a mask delimited by sea ice boundaries for aerosol scenarios NAT1 and AC3.

3.2.3 Comparison of NAT1 and NAT2 (Pair 3)

Both NAT1 and NAT2 are uncoated aerosol scenarios. The only difference between these scenarios is the presence or not of contact ice nucleation. In NAT2 scenario, contact nucleation is absent and all ice crystals form by deposition ice nucleation and immersion freezing. In NAT1, nucleation by contact is added to the other ice nucleation modes.

Figures 3.19a and b show the January mean ice water content and ice crystal number concentration averaged in time and space over the sea-ice border mask. The ice crystal concentration is slightly smaller in NAT1 throughout the troposphere. The ice water content is slightly smaller in NAT1 in the lower troposphere and there is no difference between NAT1 and NAT2 above 700 hPa. These results show that the addition of contact freezing decreases the number concentration of ice crystals with very weak changes of the ice water content.

In the presence of contact ice nucleation, a part of the available liquid water turns into ice by contact nucleation in the NAT1 scenario. Consequently, in an ice supersaturated environment, a part of the available water vapor deposits on the surface of these ice crystals. This phenomenon contributes to reduce the RH_i in the NAT1 scenario to lower values when compared to the NAT2 scenario. Figure 3.20 shows that the spatial and temporal mean RH_i is decreased by a few percent between 900 hPa and 500 hPa. Results for January 2007 show a mean negative RH_i anomaly of -2.2 % at 850 hPa averaged over the mask delimited by sea ice boundaries. Deposition ice nucleation strongly depends on the onset RH_i . In the NAT1 scenario, the threshold value required for deposition ice nucleation is not reached as often as in the NAT2 scenario. This reduces the deposition ice nucleation rate in the clouds and subsequently slightly reduces the total number of active ice nucleus at the cloud level in the NAT1 scenario. This finally results in a small decrease in the ice mixing ratio and ice crystal number concentration compared to the NAT2 scenario.

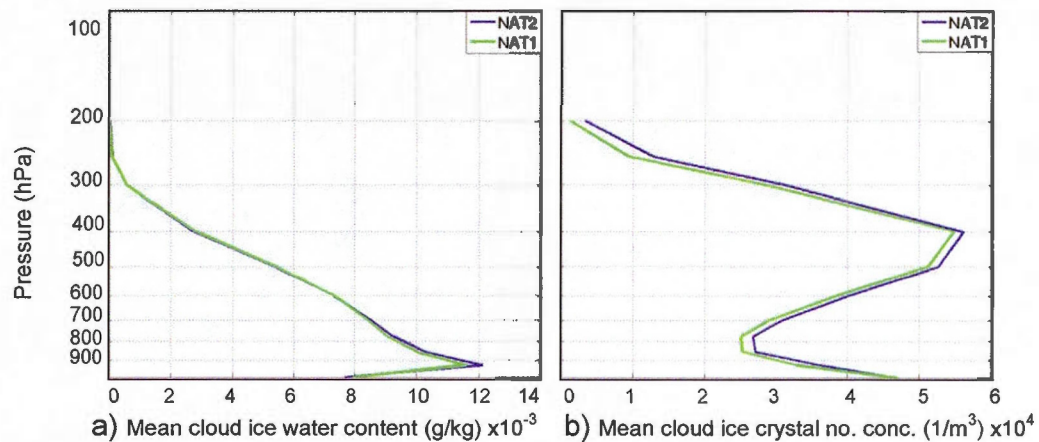


Figure 3.19: Vertical profiles of cloud (a) ice water content ($\times 10^{-3}$ g/kg) and (b) ice crystal number concentration ($\times 10^4$ 1/m³) for aerosol scenarios NAT1 and NAT2 averaged over time and spatially averaged over a mask delimited by sea ice boundaries.

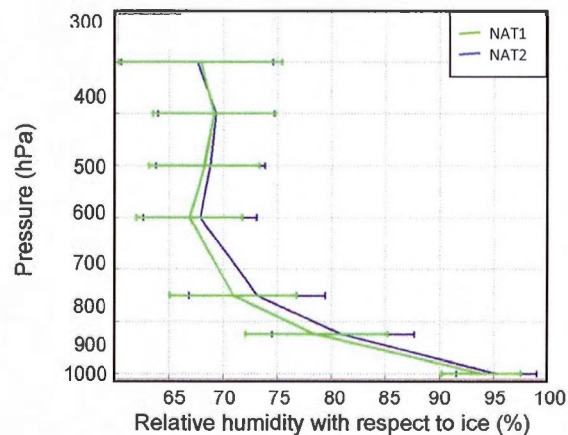


Figure 3.20: Vertical profiles of the mean relative humidity with respect to ice (%) with associated standard deviations (horizontal bars) for aerosol scenarios NAT1 and NAT2 averaged over time and spatially averaged over a mask delimited by sea ice boundaries.

Above 500 hPa, the temperature falls below -40°C . At these temperatures, homogeneous freezing of haze and water droplets becomes dominant. Since the RH_i at high altitudes are almost equal in both scenarios, there is no significant difference between NAT1 and NAT2 scenarios at the homogeneous nucleation levels. Therefore, the difference between NAT1 and NAT2 scenarios become smaller at

high altitudes. This eventually leads to negligible anomaly at high altitudes and almost identical high clouds microstructure in both NAT1 and NAT2 aerosol scenarios.

Figure 3.21 shows the spatial and temporal mean vertical profile of the liquid water content and cloud droplet concentration. The presence of contact INs causes a very slight increase in the liquid water concentration and liquid water content in the NAT1 aerosol scenario especially at 900 hPa where the mixed-phase clouds are mostly found. In fact, the lower ice crystal concentration in the NAT1 scenario increases the saturation with respect to water and reduces subsequently the evaporation rate of liquid water in NAT1 scenario. The Bergeron effect is limited by the lower ice crystal concentration and the higher supersaturation. On the other hand, because of the higher concentration of ice crystals in the NAT2 aerosol scenario, more liquid water is evaporated to deposit on the surface of available ice crystals in an ice super-saturated and liquid water sub-saturated environment. Therefore the combination of these two factors increases the water evaporation rate in the NAT2 scenario and decreases the liquid water content and concentration at the mixed-phase clouds level. As a result, the liquid water mixing ratio and concentration in the NAT1 is higher than in the NAT2 in the lower troposphere.

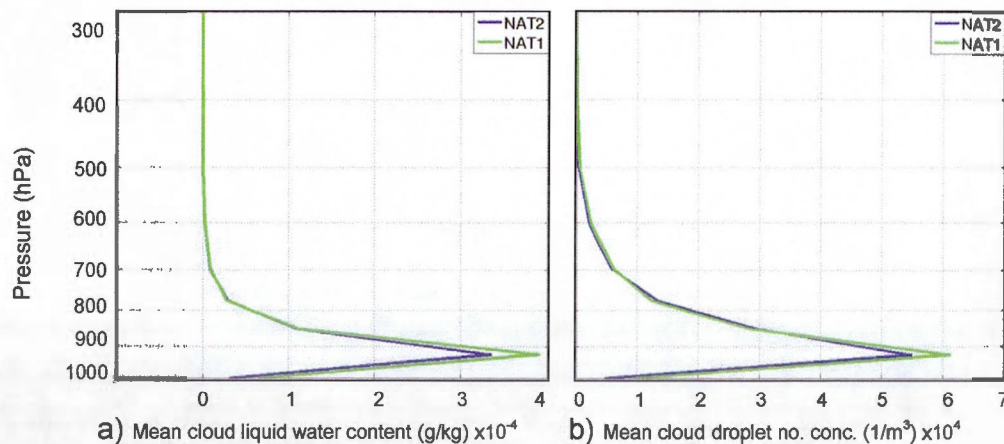


Figure 3.21: Vertical profiles of (a) cloud liquid water content ($\times 10^{-4}$ g/kg) and (b) liquid drop number concentration ($\times 10^4$ $1/m^3$) for aerosol scenarios NAT2 and NAT1 averaged over time and spatially averaged over a mask delimited by sea ice boundaries.

Figures 3.22a and b show the January mean liquid and ice water path anomaly for the whole domain. The liquid water path anomaly is positive over a large area including south of Greenland, the Labrador Sea, Baffin Bay, Hudson Bay, Bristol Bay, Bering Sea and a great part of Siberia. This anomaly has negligible small negative values close to 0 over a large area in the North Pole and peaks at the Bill Baileys Bank, Faroe Island and North of Scotland. The average value for January over the mask delimited by sea ice boundary gives a small positive liquid water path anomaly of $8.1 \times 10^{-5} \text{ kg/m}^2$. The January mean ice water path anomaly shows positive anomalies over Siberia, North and south of Greenland, North of Quebec, Hudson Bay, Chukchi Sea, East Siberian Sea and is negative over the Greenland Sea, North of Siberia, North of Canada and the Central Arctic. The spatially mean ice water path anomaly averaged over sub-domain delimited with sea-ice boundaries for the month of January gives a negative and relatively small value of $-6.7 \times 10^{-4} \text{ kg/m}^2$. However, the ice water path anomaly is larger over regions that are warmer than the Central Arctic and are characterized by a large occurrence of mixed-phase clouds (e.g. Girard *et al.*, 2012). This is the case for the Kara and Barents Sea with ice water path anomalies of up to -0.06 mm . These results confirm the ice crystal loss and the liquid water increase in NAT1 aerosol scenario compared to NAT2 but also show the regional aspect of the largest changes.

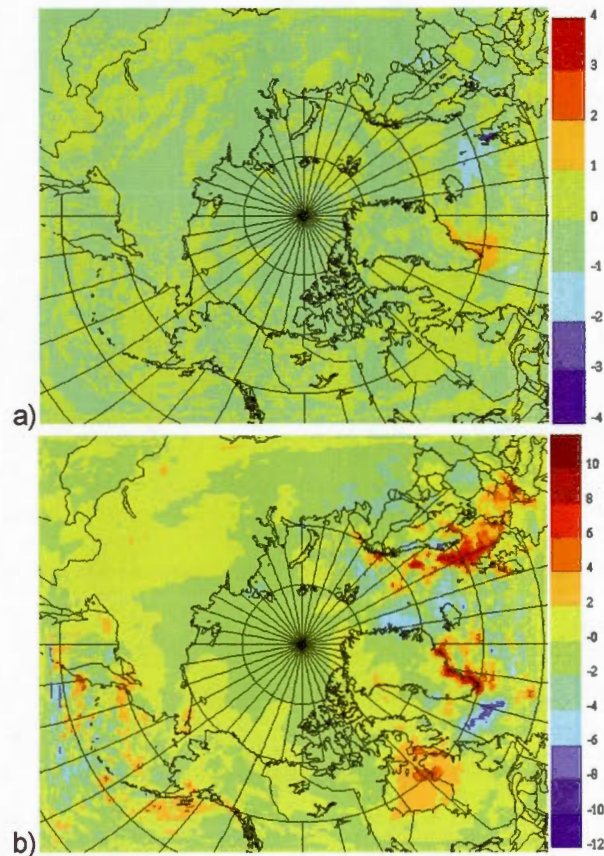


Figure 3.22: January mean (a) liquid water path anomaly ($\times 10^{-2}$ mm) and (b) ice water path anomaly ($\times 10^{-2}$ mm) in the Arctic when the anomaly is defined as the difference between NAT1 and NAT2 (NAT1- NAT2).

Figure 3.23a, b and c show respectively the co-variability of RH_i , ice crystal number concentration and droplet number concentration with temperature. At the favourable temperature range for contact ice nucleation, that is between -15°C and -38°C , the RH_i in NAT1 is lower than that of NAT2. Figures 3.23b and c respectively confirm that, at this temperature range, the ice crystal concentration in NAT1 is lower and cloud droplet concentration is higher when compared to NAT2. While the above discussion is true for temperatures lower than -15°C , differences between both scenarios are not the same at warmer temperatures. For these warmer temperatures, deposition ice nucleation on kaolinite particles is not possible anymore because the ice supersaturation cannot reach the onset ice supersaturation value for

ice nucleation before reaching the saturation with respect to liquid water. Therefore, only contact and immersion nucleation are active in NAT1 while only immersion freezing is active in NAT2. Not surprisingly, the number concentration of ice crystals is larger in NAT1 for these temperatures. At temperatures close to 0°C, the droplet number concentration is larger in NAT1 compared to NAT2. This seems to be linked to the fact that RH_i is also larger in NAT1 for the warmest temperatures.

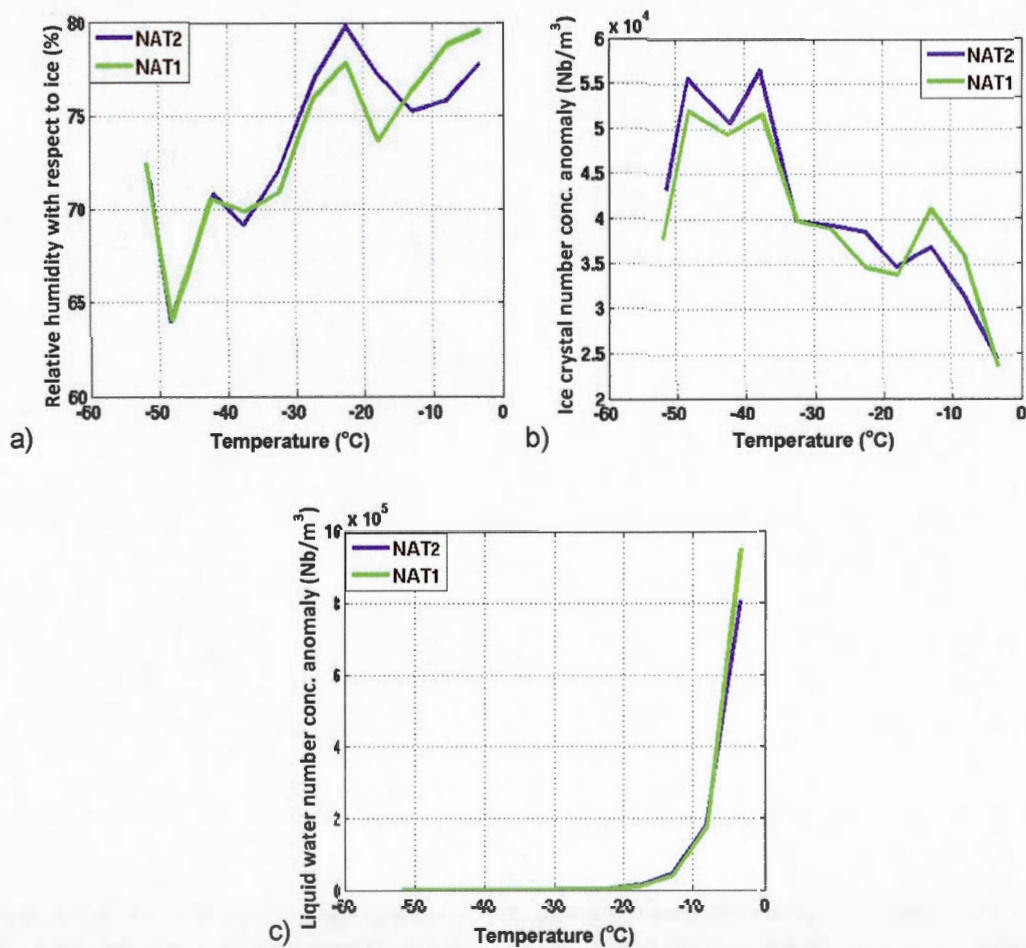


Figure 3.23: January daily mean (a) relative humidity with respect to ice (%) (b) ice crystal number concentration ($\times 10^4$ $1/m^3$) (c) liquid water drop concentration ($\times 10^5$ $1/m^3$) with temperature averaged over 5 K intervals for aerosol scenarios NAT1 and NAT2 averaged over time and spatially averaged over a mask delimited by sea ice boundaries.

These results show no important differences on the microstructure of both ice only and mixed-phase clouds between NAT1 and NAT2. However, previous studies (e.g. Girard *et al.*, 2012) have shown that even small differences in the cloud microstructure may lead to substantial effects on the cloud radiative forcing and the temperature in the Arctic wintertime atmosphere.

Figure 3.24a and b show the cloud radiative forcing anomaly at the surface and at the TOA respectively. The CRF anomalies at the surface and at the TOA are both negative over the north of Siberia, central Arctic Ocean, west of Greenland, the Scandinavia and Norwegian. The CRF anomalies are positive over the north and northwest of Canada, south of Siberia, Barents Sea and the Kara Sea. These CRF anomalies are rather small and the absolute values of the maximum negative and positive CRF anomalies are smaller than 10 W/m^2 .

Based on the dependence of cloud radiative properties to the mass concentration of hydrometeors, a mean decrease of the ice water path of -6.7×10^{-4} mm (averaged over the sub-domain delimited by sea-ice boundaries) contributes to reduce the mean January CRF to -0.03 W/m^2 at the top of the atmosphere and to -1.02 W/m^2 at the surface in NAT1 compared to NAT2 averaged over the sub-domain delimited by sea-ice boundaries. It should be noted that the positive CRF anomalies both at the surface and at the TOA are not statistically significant as opposed to most of the negative CRF anomalies over the sea ice mask (see Figures D.7 and D.8 in Appendix D). Therefore, the averaged values both at the surface and at the TOA are likely to be underestimated.

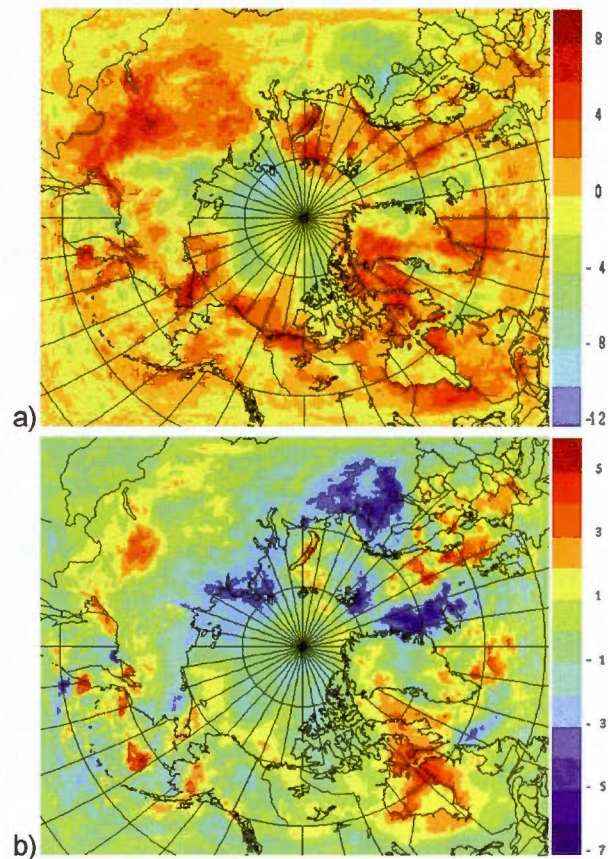
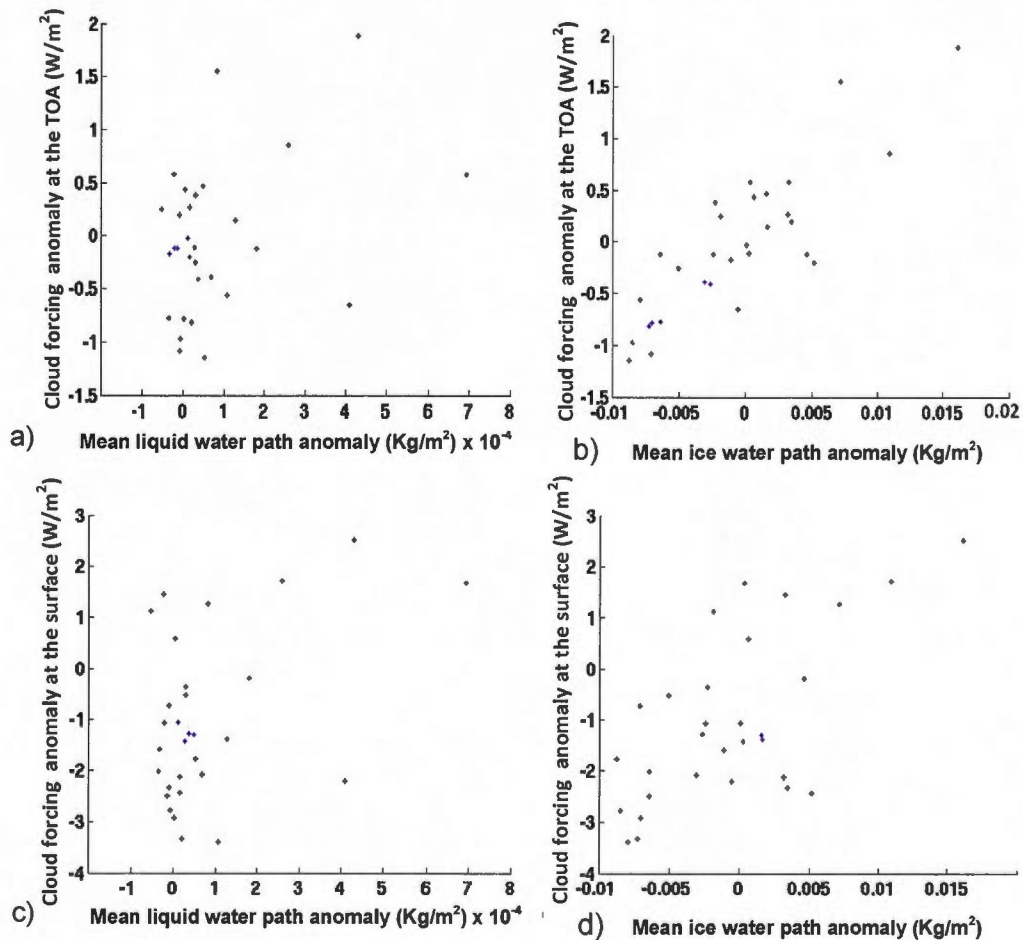


Figure 3.24: Mean January 2007 cloud forcing anomaly (W/m^2) at (a) the surface and at (b) the TOA over the Arctic when the anomaly is defined as the difference between NAT1 and NAT2 (NAT1- NAT2).

This fact is also shown in the Figure 3.25b and d, which show respectively the co-variation of cloud forcing anomaly at TOA with the vertically integrated ice and liquid water path. Results show that the cloud forcing anomaly absolute values at both TOA and at the surface are highly correlated to the integrated ice water anomaly and increases as integrated ice water anomaly absolute value increases. However, the CRF anomalies do not depend on the liquid water path. The positive liquid water path anomaly of 8.1×10^{-5} mm does not make a change in the CRF at the surface and at the TOA. In fact, as both NAT1 and NAT2 aerosol scenarios have liquid water path values higher than 15 g/m^2 , clouds emit as blackbody objects in the

infrared in these two scenarios. Thus, an increase in the liquid water path in NAT1 does not change the radiation characteristics of the clouds.



Figures 3.25: Pair 3 scatter plot of the daily mean cloud forcing anomaly of January 2007 at TOA and at the surface (W/m^2) as a function of daily mean vertically integrated (a,c) liquid water path anomaly ($\times 10^{-4} Kg/m^2$) and (b,d) ice water path anomaly (Kg/m^2) averaged over the sub-domain delimited by sea ice when the anomaly is defined as the difference between NAT1 and NAT2 (NAT1- NAT2).

Figure 3.26 shows the mean January temperature anomaly over the Arctic at 850 hPa. The mean January temperature anomaly at 850 hPa is negative over the north of Siberia, Scandinavia, Barents Sea and Norwegian Sea. The temperature anomaly is also positive over Northern Canada, Baffin Bay, Labrador Sea and a part

of North Atlantic Ocean at the North of Europe. As expected, the regions with the negative/positive temperature anomaly over the Arctic during January coincide to a great extent with the region where the CRF anomalies are negative/positive (see Figure 3.24) confirming the impact of cloud forcing on the tropospheric temperature. It should be noted that statistical tests reveal that the temperature anomalies are not statistically significant. It is however reasonable to assume that additional ensemble members would have confirmed the negative temperature anomaly areas since the corresponding CRF anomalies at the TOA are statistically significant.

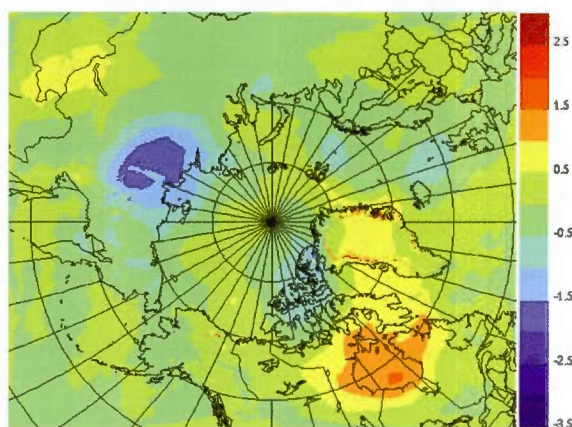


Figure 3.26: mean January temperature anomaly over the Arctic at 850 hPa when the anomaly is defined as the difference between NAT1 and NAT2 (NAT1- NAT2).

Figure 3.27 show the mean January vertical temperature profile of NAT1 and NAT2 aerosol scenarios. Results show that, the presence of contact nucleation do not have a significant effect on the temperature suggesting that the addition of contact nucleation INs in the clear Arctic clouds does not change the tropospheric clouds microstructure and the tropospheric temperature. However, the temperature anomaly can be regionally relatively important.

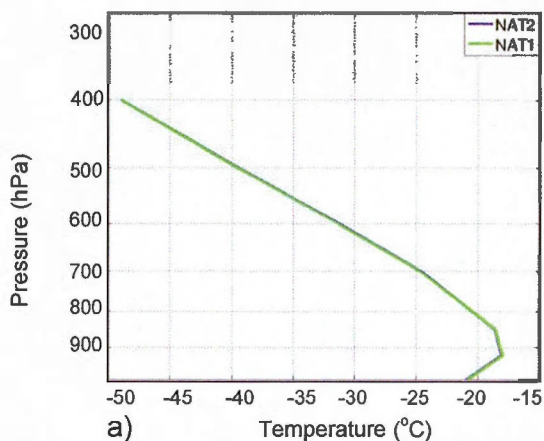


Figure 3.27: January 2007 mean temperature ($^{\circ}\text{C}$) vertical profiles averaged over a mask delimited by sea ice boundaries for aerosol scenarios NAT1 and NAT2.

3.2.4 Comparison of AC1 and AC2 (Pair 4)

The difference between the two acid coated scenarios involved in this pair is the presence of contact INs in the AC1 scenario and its absence in the AC2 scenario in an acid polluted environment. The aim of this comparison is to investigate the effect of contact nucleation when the deposition ice nucleation is limited by acid coating on INs.

Figure 3.28a and b show the January mean ice water content and ice crystal number concentration spatially averaged over a mask delimited by sea-ice boundaries for AC1 and AC2 aerosol scenarios. At pressure levels below 400 hPa, the ice crystal concentration is slightly smaller in the AC1 compared to the AC2 and is almost equal at higher altitudes. Also the addition of contact INs in AC1 does not have a significant impact on the ice water content throughout the troposphere.

Following the same reasoning explained in the section 3.2.3, adding contact INs contribute to decreases the total number concentration of active INs resulting in the formation of fewer but bigger ice crystals and consequently more frequent precipitation from the cloud levels. Therefore, the contribution of contact nucleation

in the clouds reduces the total ice crystal number concentration and ice content in the troposphere. It is noteworthy to mention however that the decrease in the ice crystal concentration in the acid polluted environment is lower when compared to the decrease obtained in the pair 3 (NAT1 and NAT2). In NAT1, the presence of contact IN contributes to decrease the variability of the cloud ice supersaturation. Therefore, the ice nucleation events by deposition are less frequent as explained in section 3.2.3. In the AC1 scenario, it is also true. However, the nucleation events in AC2 are much smaller in terms of ice crystal number concentration because of the acid coating on INs and the higher onset ice supersaturation for ice nucleation. Therefore, the differences are much smaller between AC1 and AC2 when compared to differences between NAT1 and NAT2.

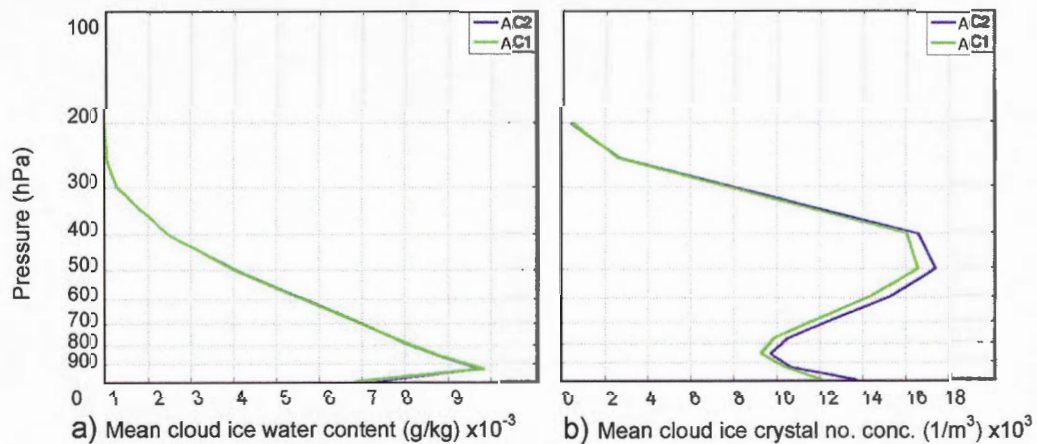


Figure 3.28: Vertical profiles of cloud ice water (a) content ($\times 10^{-3}$ g/kg) and (b) ice crystal number concentration ($\times 10^3$ $1/m^3$) for aerosol scenarios AC1 and AC2 averaged over time and spatially averaged over a mask delimited by sea ice boundaries.

Figure 3.29 shows the mean vertical profile of RH_i during January 2007 averaged over the sea-ice mask in the Arctic for the AC1 and AC2 aerosol scenarios. According explanation given above, because of the slight effect of the presence of contact nucleation in the acid polluted environment, the RH_i vertical profile in both AC1 and AC2 aerosol scenarios are almost equal throughout the troposphere.

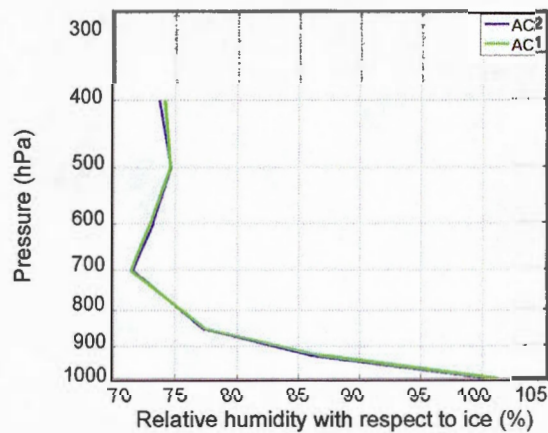


Figure 3.29: Vertical profile of the mean relative humidity with respect to ice (%) for aerosol scenarios AC1 and AC2 averaged over time and spatially averaged over a mask delimited by sea ice boundaries.

Figures 3.30a and b show respectively the vertical profile of January mean liquid water content and liquid droplet concentration spatially averaged over the sea ice mask. The liquid water content and water droplet concentration in AC1 and AC2 scenarios are almost equal throughout the troposphere except between 920 and 720 hPa, which is the pressure level interval related to the presence of mixed-phase clouds. At this interval, the ice crystal concentration is higher in the AC1 scenario compared to the AC2 scenario. Following the same reasoning explained in the section 3.2.3, the lower nucleation rate in AC1 aerosol scenario increases the supersaturation with respect to water. This fact and the decreased ice crystal concentration in the AC1 scenario contribute to reduce the liquid water evaporation rate at the presence of contact INs, increasing the liquid water content and water droplet concentration in the AC1 scenario compared to the AC2.

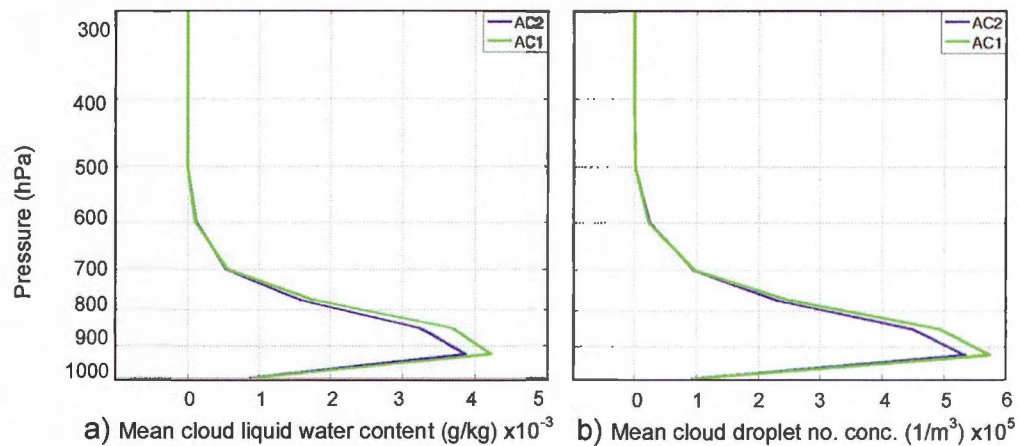


Figure 3.30: Vertical profiles of cloud liquid water (a) content ($\times 10^{-3}$ g/kg) and (b) liquid drop number concentration ($\times 10^5$ $1/m^3$) for aerosol scenarios AC1 and AC2 averaged over time and spatially averaged over a mask delimited by sea ice boundaries.

Figures 3.31a and b show the mean January liquid and ice water path anomaly over the Arctic. The liquid water anomaly is positive over the north and west of Siberia, the central Arctic Ocean, the Bering Sea, the Hudson Bay and peaks over the Barents Sea. It is also negative over the north west of Canada, southern Siberia, the Labrador Sea and north of the Northwest Territories. The mean January spatially averaged liquid water path anomaly is positive and equals 0.00078 kg/m^2 over the sea-ice mask. The mean ice water path anomaly is either positive or negative with small values over most of the regions. The largest anomaly is negative over the Barents Sea. The mean January spatially averaged ice water path anomaly is negligible over the mask delimited the sea-ice boundaries.

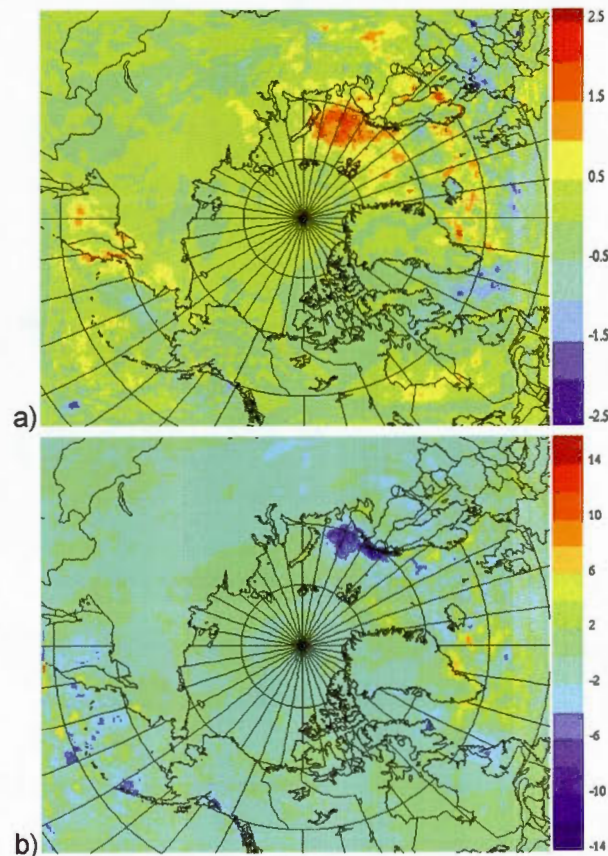


Figure 3.31: January mean (a) liquid water path anomaly ($\times 10^{-2}$ mm) and (b) ice water path anomaly ($\times 10^{-2}$ mm) in the Arctic when the anomaly is defined as the difference between AC1 and AC2 (AC1-AC2).

The mean January CRF anomalies at the surface and at the TOA are shown respectively in Figures 3.32a and b. The mean January CRF anomalies at the surface and at the TOA are both positive over the far northern and eastern Siberia, great part of Mongolia, great part of Greenland, Greenland Sea, Labrador Sea, western Alaska, the Arctic Ocean at the North of Siberia and are negative elsewhere in the Arctic. These CRF anomalies over the vast area of the Arctic are rather small with absolute values ranging between 0 and 2 W/m^2 . When averaged over a mask delimited by sea-ice boundaries, we obtain a positive CRF anomaly at TOA of 0.05 W/m^2 and 0.48 W/m^2 at the surface.

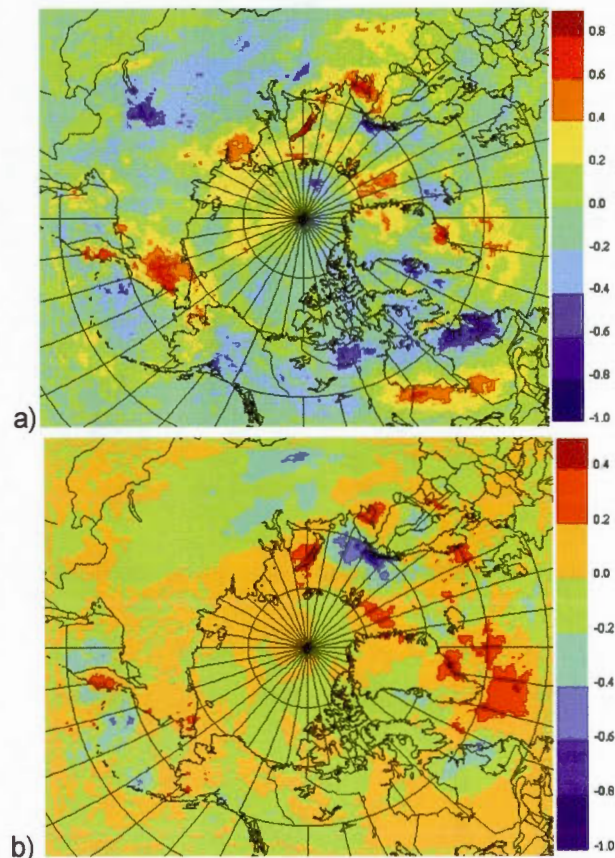


Figure 3.32: Mean January 2007 cloud forcing anomaly ($\times 10 \text{ W/m}^2$) at (a) the surface and at (b) TOA over the Arctic when the anomaly is defined as the difference between AC1 and AC2 (AC1-AC2).

Figure 3.33 shows the mean January temperature anomaly over the Arctic at 850 hPa. This anomaly is positive over western and northern Siberia, Alaska, the Greenland, Greenland Sea and the Arctic Ocean at the North of Siberia and is negative elsewhere. As opposed to the other comparisons done in the other sections (for instance for pair 3), regions with negative (positive) CRF anomalies do not necessarily correspond to regions where cooling (warming) is obtained. Figure 3.34 shows the daily mean CRF anomaly at the TOA as a function of the daily mean temperature anomaly for each grid point inside the mask delimited by sea ice boundaries for pair 4 and pair 3. While a good relationship exists between the anomalies of CRF at TOA with temperature anomalies for pair 3 ($r=0.60$), this is not

the case for pair 4 with $r=0.09$ with several points with positive (negative) CRF at the TOA producing negative (positive) temperature anomaly. In pair 4, the anomalies of the CRF at the TOA remain small (-2 W m^{-2} to $+2 \text{ W m}^{-2}$) when compared to pair 3 (-4 W m^{-2} to $+4 \text{ W m}^{-2}$). Such small CRF anomalies have a smaller effect on temperature than other anomalies resulting of cloud microphysical changes such as the atmospheric circulation. In this research, the exact reason has not been investigated.

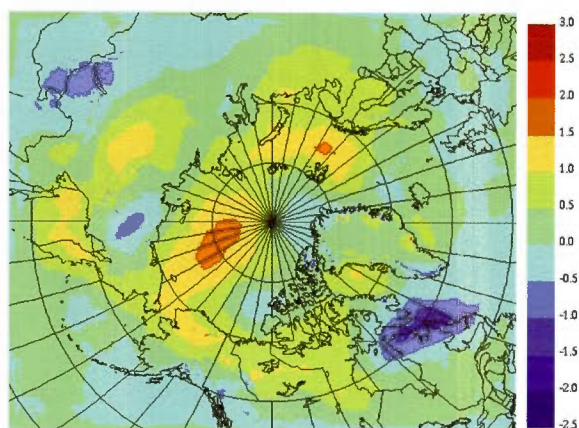


Figure 3.33: Mean January temperature anomaly over the Arctic at 850 hPa when the anomaly is defined as the difference between AC1 and AC2 (AC1- AC2).

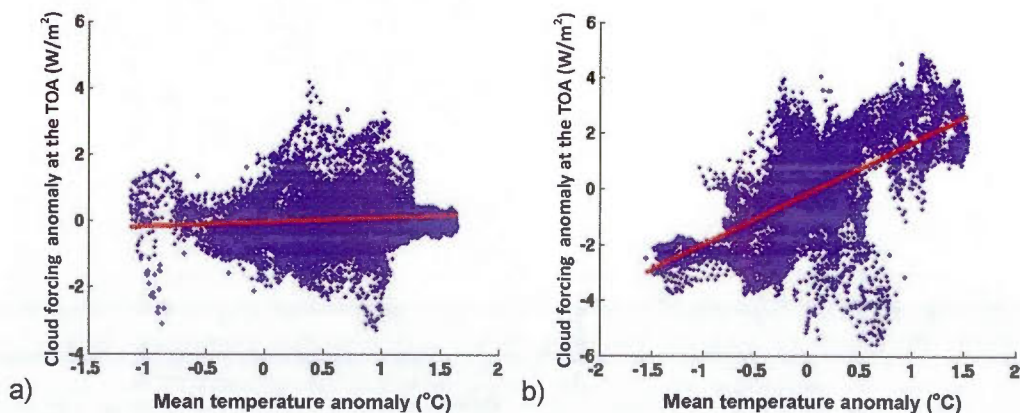
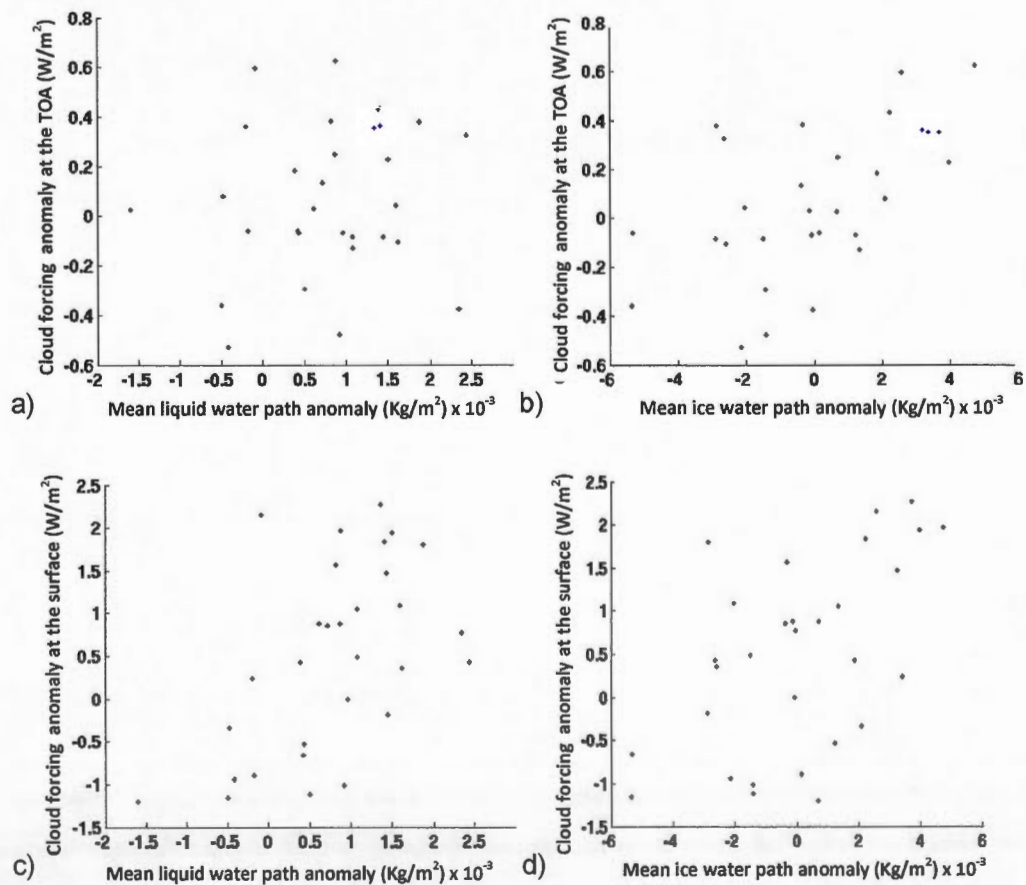


Figure 3.34: Daily mean CRF anomaly at the TOA as a function of the daily mean temperature anomaly for each grid point inside the mask delimited by sea ice boundaries for the (a) pair 4 and (b) pair 3 when the anomaly is defined as the difference between AC1 and AC2 (AC1- AC2).

Figures 3.35 show the co-variation of cloud forcing anomaly at the TOA and at the surface as a function of vertically integrated ice and liquid water path anomalies. Results show that the CRF anomaly at the TOA is rather weakly related to the liquid and ice water path anomalies with both negative and positive CRF anomalies values for negative CRF anomalies. These results are due to the fact that the ice and liquid water path anomalies are rather small with values one order of magnitude smaller than the liquid and ice water path anomalies obtained for the pair 3. The CRF anomalies at the surface are more directly related to the liquid water path anomalies and do not depend on the ice water path anomalies.



Figures 3.35: Pair 4 scatter plot of the daily mean cloud forcing anomaly of January 2007 at TOA and at the surface (W/m^2) as a function of daily mean vertically integrated (a,c) liquid water path anomaly ($\times 10^{-3} Kg/m^2$) and (b,d) ice water path anomaly ($\times 10^{-3} Kg/m^2$) averaged over the sub-domain delimited by sea ice when the anomaly is defined as the difference between AC1 and AC2 (AC1-AC2).

Figure 3.36 shows the vertical profile of temperature averaged over the sea ice mask for aerosol scenarios AC2 and AC1. In the presence of contact nucleation (AC1), there is a warming of less than 0.5 K in the lower troposphere between 950 and 700 hPa with no significant differences higher in the troposphere.

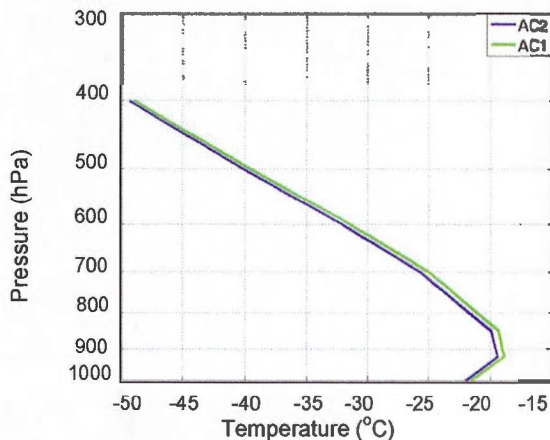


Figure 3.36: January 2007 mean temperature ($^{\circ}\text{C}$) vertical averaged over a mask delimited by sea ice boundaries for aerosol scenarios AC2 and AC1.

3.2.5 Comparison of AC2 and NAT2 (Pair 5)

In this pair, the effect of acid coating in the absence of contact ice nucleation is investigated. A comparison of this pair with the pair 1 indicates the role and importance of contact ice nucleation when the deposition ice nucleation is affected by acid coating. Indeed, one may hypothesize that contact ice nucleation can compensate to some extent the decrease of ice nucleation by deposition. The pair 5 investigated in this section allows us to evaluate this issue.

The pair 5 includes the acid coated AC2 and the uncoated NAT2 aerosol scenarios in the absence of contact INs. Here, the same argument used for the pair 1 is applicable except that in the pair 5, the absence of contact freezing should be considered in the nucleation process. Also, the reasoning applied for the pair 4 could be used to investigate the effect of no the contact INs on the Arctic clouds

characteristics. As discussed in the section 3.2.1, the acid coating on INs contributes to reduce the concentration of active deposition INs and consequently decrease the number concentration of ice crystals and ice water content. Figure 3.37a and b show that similar results are obtained for the pair 5. As expected, results show a lower ice water content and ice crystal number concentration in the acid-coated AC2 aerosol scenario compared to the uncoated NAT2 scenario throughout the troposphere.

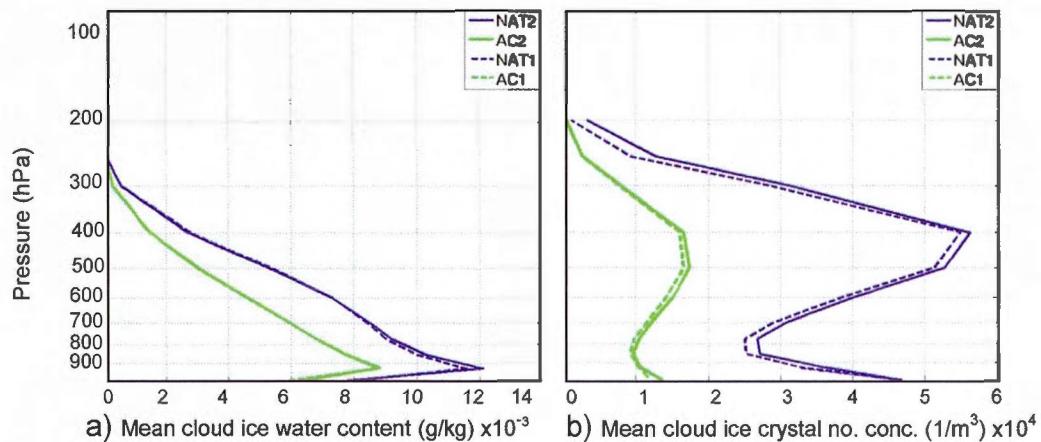


Figure 3.37: Vertical profiles of cloud (a) ice water content ($\times 10^{-3}$ g/kg) and (b) ice crystal number concentration ($\times 10^4$ $1/m^3$) for aerosol scenarios NAT2, AC2 (solid lines), and NAT1, AC1 (dotted lines) averaged over time and spatially averaged over a mask delimited by sea ice boundaries.

A comparison between the ice crystal concentration in the troposphere in the pair 5 and pair 1 (see Figures 3.37a,b) shows that the decrease of the ice crystal concentration in the pair 5 is slightly larger compared to the pair 1. This is due to the absence of contact INs in the pair 5. This deactivation of contact INs in the NAT2 aerosol scenario of the pair 5 contributes to increase the RH_i in the troposphere to the onset RH_i required for the deposition nucleation, activating a part of deposition INs. This deposition INs activation event compensates the deactivation of contact INs effect in the uncoated scenario of the pair 5 increasing slightly the active INs in the uncoated scenario of the pair 5 compared to that of the pair 1. The same thing happens in the acid polluted environment, except that since coated INs have higher RH_i onset for deposition nucleation compared to uncoated INs, the deposition

nucleation rate is lower over the coated INs with contact angles as high as 27° in AC1 scenario compared to the uncoated NAT1 scenario with contact angle of 12° (see Chapter I). Thus, the absence of contact INs has smaller impact in the polluted environment compared to the clear environment. It is noteworthy to mention that the absence of the contact INs does not have a pronounced effect on the cloud ice content in the troposphere.

Figures 3.38a and b show the vertical profile of liquid water content and liquid water drop concentration averaged over the sea-ice mask in the NAT2, AC2, NAT1 and AC1 aerosol scenarios. Following the same reasoning used in the section 3.2.1, the lower ice crystal concentration and higher ice supersaturation in the acidified AC2 scenario of the pair 5 contribute to reduce the water evaporation rate by Bergeron effect, increasing the liquid water content and water drop concentration number in the AC2 scenario compared to the uncoated NAT2 scenario.

A comparison between the liquid water content anomaly and water droplet concentration in the pairs 3 and 1 (see Figures 3.38a,b) shows that the liquid water content and droplet concentration in the pair 1 increases more by acid coating on INs compared to the pair 5. The larger ice crystal concentration in the AC2 scenario contributes to enhance the evaporation of liquid droplets and the deposition on ice crystals by the Bergeron effect. As a result, the liquid water content and droplet number concentration is slightly lower in the AC2 scenario compared to the AC1 scenario. The results give a mean January liquid water content anomaly of 3.14×10^{-6} kg/kg for the pair 5 and mean value of 3.57×10^{-6} kg/kg for the pair 1 at 850 hPa.

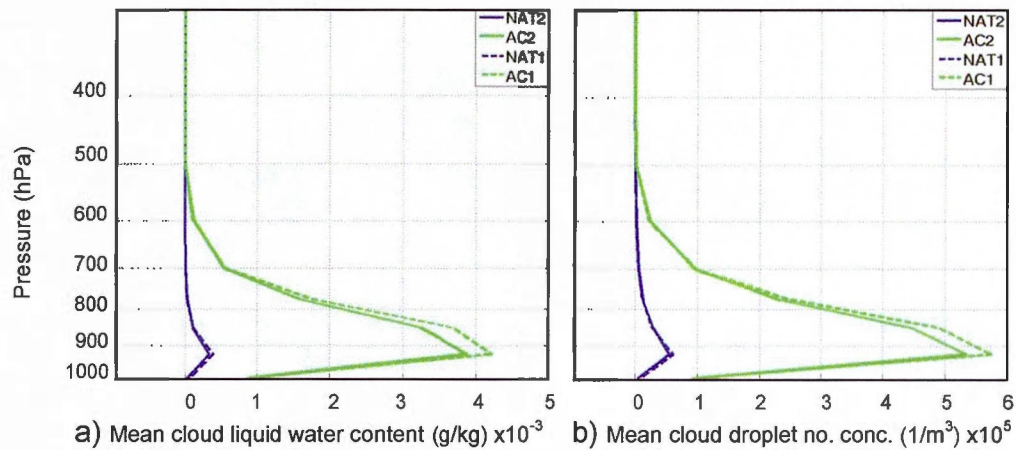


Figure 3.38: Vertical profiles of cloud (a) liquid water content ($\times 10^{-3}$ g/kg) and (b) liquid drop number concentration ($\times 10^5$ 1/m³) for aerosol scenarios NAT2, AC2 (solid lines), and NAT1, AC1 (dotted lines) averaged over time and spatially averaged over a mask delimited by sea ice boundaries.

As observed in the figures 3.37 and 3.38, the results show the effect of acid coating of INs in both pairs 1 and 3 are similar. The contribution of contact freezing on the cloud microstructure in an acidic scenario is therefore very small. The hypothesis made at the beginning of this section about the possibility that contact ice nucleation could compensate the lower ice nucleation by deposition in the acidic aerosol scenario is not verified.

Figure 3.39 shows the mean January RH_i vertical profile over the sub-domain delimited by sea-ice boundaries for the NAT2 and AC2 scenarios. The partial IN deactivation by the acid coating increases the available water vapor in the troposphere making the RH_i higher in the acidified AC2 scenario than in the non-acid NAT2 scenario. The results give a mean January RH_i anomaly of 4% at 850 hPa in pair 5 averaged over the sub-domain delimited by sea-ice boundaries. This result is very similar to what was obtained in pair 1 (see Figure 3.6b). This means that contact ice nucleation is not important enough to significantly reduce the relative humidity with respect to ice.

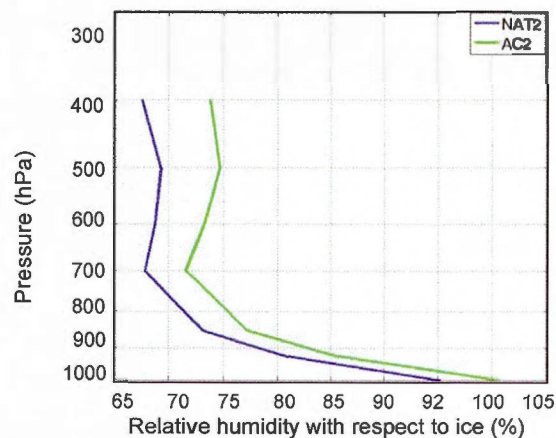


Figure 3.39: Vertical profile of the mean relative humidity with respect to ice (%) for aerosol scenarios NAT2 and AC2 averaged over time and spatially averaged over a mask delimited by sea ice boundaries.

The mean January ice and liquid water path anomaly over the Arctic are shown in Figures 3.40a and b. These figures show that the increase in the January mean liquid water content and the decreases in the ice water content are widespread over the Arctic. The results give a January mean positive liquid water path anomaly of $7.2 \times 10^{-3} \text{ kg/m}^2$ and a negative ice water path anomaly of -0.0162 kg/m^2 averaged over the the sub-domain delimited by sea-ice boundaries.

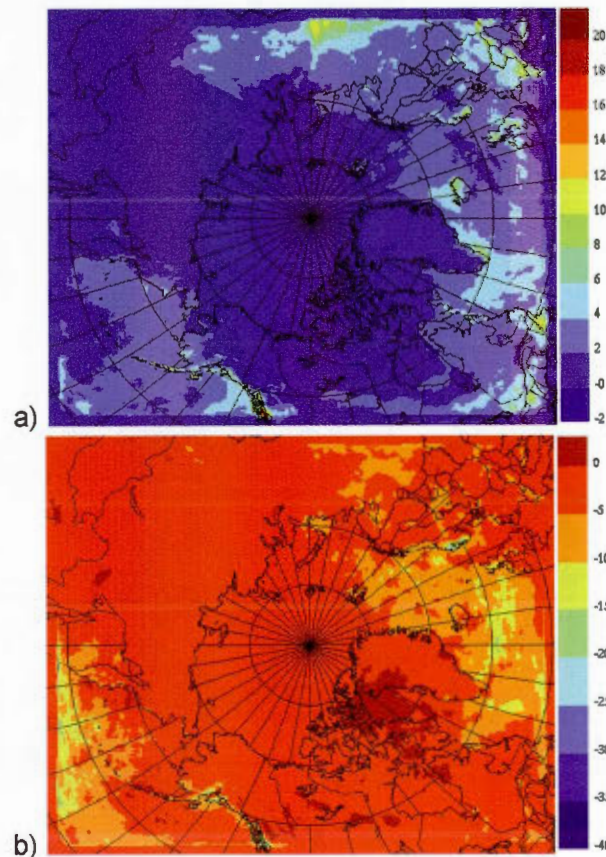


Figure 3.40: January mean (a) liquid water path anomaly ($\times 10^{-2}$ mm) and (b) ice water path anomaly ($\times 10^{-2}$ mm) in the Arctic when the anomaly is defined as the difference between AC2 and NAT2 (AC2-NAT2).

Figures 3.41a and b show the CRF anomalies respectively at the surface and at the TOA. The CRF anomaly at the surface is positive over the Bering Sea, northern Canada and western and central Siberia with values mostly ranging between 0 and 15 W/m^2 and is negative elsewhere with values ranging from 0 and -10 W/m^2 . The CRF at the TOA is almost negative everywhere in the Arctic except over a small area in Sakha at the eastern Siberia and Baffin Bay at the south of Greenland where the anomaly is positive with a maximum value as small as 1.6 W/m^2 . However the spatially averaged CRF anomalies over the sea-ice mask at the Arctic give a mean negative CRF anomaly of -0.23 W/m^2 at the surface and a mean negative CRF anomaly of -3.2 W/m^2 at the TOA.

Based on the dependency of the cloud forcing to the hydrometeor concentration in the atmosphere, the increase of the liquid water path in the troposphere should increase the CRF at the surface. The resulted negligible CRF anomaly at the surface is due to the colder low-level cloud temperatures in AC2, which compensates the radiative effect of the liquid water path increase. The optically thinner and more transparent clouds formed by the effect of acidic pollutant on the cloud microstructure in the mid and upper troposphere increases the infrared transmissivity of this part of the atmosphere. As a result, more IR radiation escapes to space in the AC2 aerosol scenario. This, results in a negative cloud radiative forcing anomaly at TOA averaged over the sub domain delimited by the sea-ice boundaries.

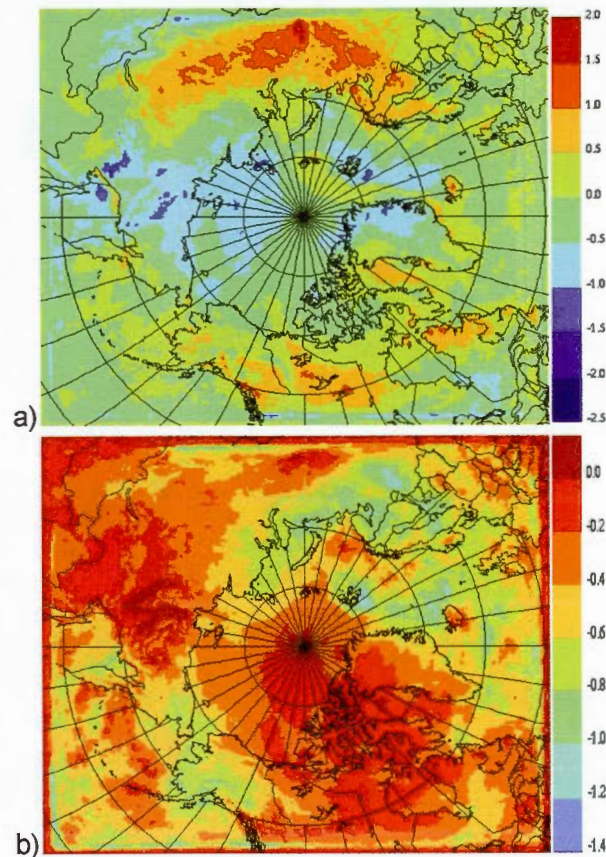
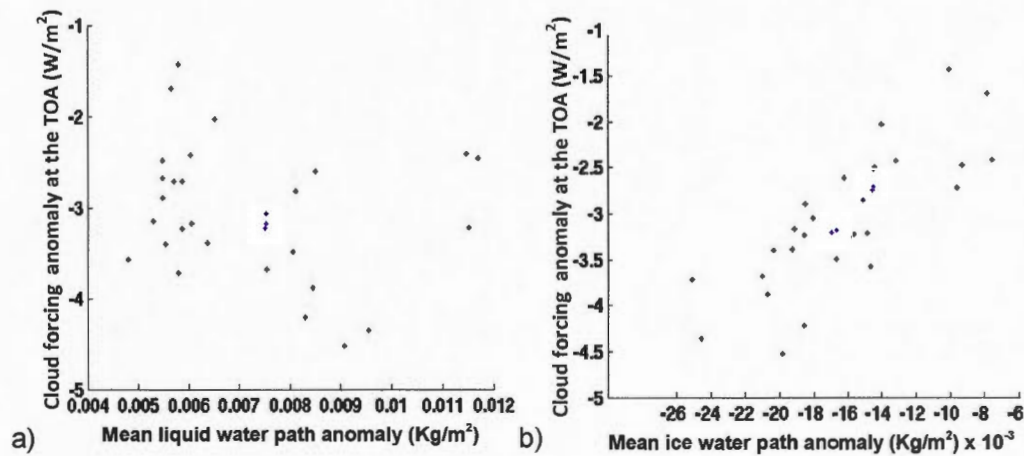


Figure 3.41: Mean January 2007 cloud forcing anomaly ($\times 10 \text{ W/m}^2$) at (a) the surface and at (b) TOA over the Arctic when the anomaly is defined as the difference between AC2 and NAT2 (AC2-NAT2).

Figures 3.42a and b show the co-variation of cloud forcing anomaly at TOA as a function of integrated liquid and ice water path. Figure 3.42a shows that the increase in the liquid water path does not have any significant effect in the CRF at the TOA. Just like the pair 1, the reason of this fact could be the high content of liquid water in the troposphere, which causes that the clouds emit as the blackbody. However, the CRF at the TOA strongly depends on the ice water path decrease in the acidified AC2 scenario.



Figures 3.42: Pair 5 scatter plot of the daily mean cloud forcing anomaly of January 2007 at TOA as a function of daily mean (a) liquid water path anomaly (Kg/m²) and (b) ice water path anomaly (x10⁻³ Kg/m²) averaged over the sub-domain delimited by sea ice when the anomaly is defined as the difference between AC2 and NAT2 (AC2-NAT2).

The mean January anomaly of temperature at 850 hPa has been shown in the Figure 3.43. The temperature anomaly is positive over a small area over the central and northern Greenland, Greenland Sea, Sakha at the eastern Siberia. Western and central Mongolia and over the Bering Sea and is negative elsewhere in the Arctic with cooling up to 3 K. As expected, the regions with positive/negative temperature anomaly match to a great extent to the regions where CRF anomaly at the TOA or at the surface is positive/negative (see Figures 3.41a,b) confirming the effect of cloud forcing on the tropospheric temperature.

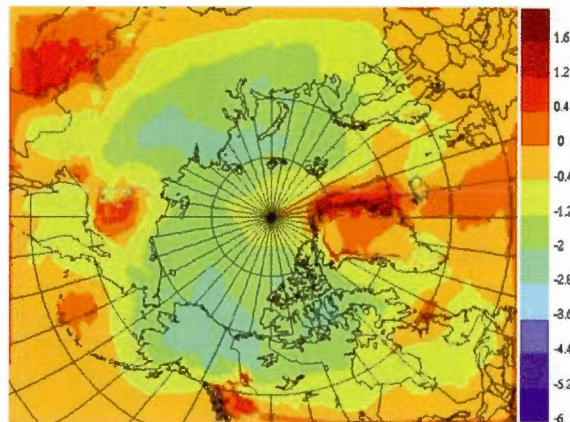


Figure 3.43: Mean January temperature anomaly over the Arctic at 850 hPa when the anomaly is defined as the difference between AC2 and NAT2 (AC2- NAT2).

These negative cloud forcings reduce the troposphere temperature at all pressure levels. Figure 3.44 compares the mean January vertical profile of temperatures on AC2 and NAT2 averaged over the sea-ice mask. As expected, in the AC2 acidified scenario the temperature is lower than in uncoated NAT2 scenario with largest values in the lower troposphere.

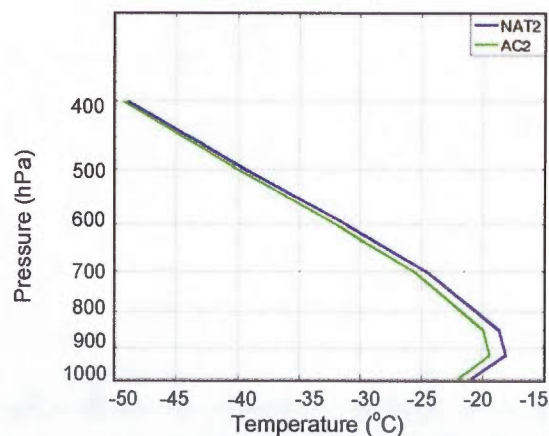


Figure 3.44: Vertical profile of the mean temperature ($^{\circ}\text{C}$) for aerosol scenarios NAT2 and AC2 averaged over time and spatially averaged over a mask delimited by sea ice boundaries.

Table 3.3 displays the temperature anomaly at 500, 850 and 1000 hPa caused by the negative cloud forcing. Given that fact that CRF absolute anomaly in the pair

5 is larger than in the pair 1, more infrared energy escapes to the outer space in the pair 5, therefore the temperature decreases more in the acidified scenario of pair 5 compared to pair 1 in which contact nucleation is considered.

Table 3.3: Pair 5 temperature anomaly at 1000, 850 and 500 hPa and cloud forcing anomaly at TOA and surface at the surface averaged over the sub-domain delimited by sea-ice boundaries

Mean CRF anomaly at surface (W/m^2)	-0.23
Mean CRF anomaly at TOA (W/m^2)	-3.2
Mean temperature anomaly 1000 hPa ($^{\circ}\text{C}$)	-1.28
Mean temperature anomaly 850 hPa ($^{\circ}\text{C}$)	-1.32
Mean temperature anomaly 500 hPa ($^{\circ}\text{C}$)	-0.63

3.2.6 Comparison of AC3 and NAT3 (Pair 6)

This pair is similar to the pair 3 in terms of the presence or not of the contact nucleation in a non polluted environment. It however differs from the pair 3 by the range of contact angles normally distributed according to the probability density function (see equation 2.7). The pair 6 includes two uncoated scenarios: NAT3 in which the contact INs are absent and the AC3 scenario with contact INs.

Figures 3.45a and b show respectively the January mean vertical profile of the ice water content and the ice crystal number concentration for the aerosol scenarios NAT3 and AC3 spatially averaged over the mask delimited by the sea-ice boundaries. The ice crystals concentration in the AC3 aerosol scenario is smaller everywhere throughout the troposphere compared to that of the NAT3 scenario in which the contact INs are absent. The ice water content in the AC3 scenario is smaller than the NAT3 scenario at all pressure levels except near the surface between 920 and 1000 hPa where the ice water content in both scenarios are almost equal. Following the same reasoning used for the pair 3 in the section 3.2.3, the

presence of the contact INs contributes to deactivate a part of deposition INs by reducing the RH_i . As a result, the onset RH_i for deposition ice nucleation is not reached as often in aerosol scenario AC3. This reduces the total ice crystal number concentration and ice mixing ratio in the clouds.

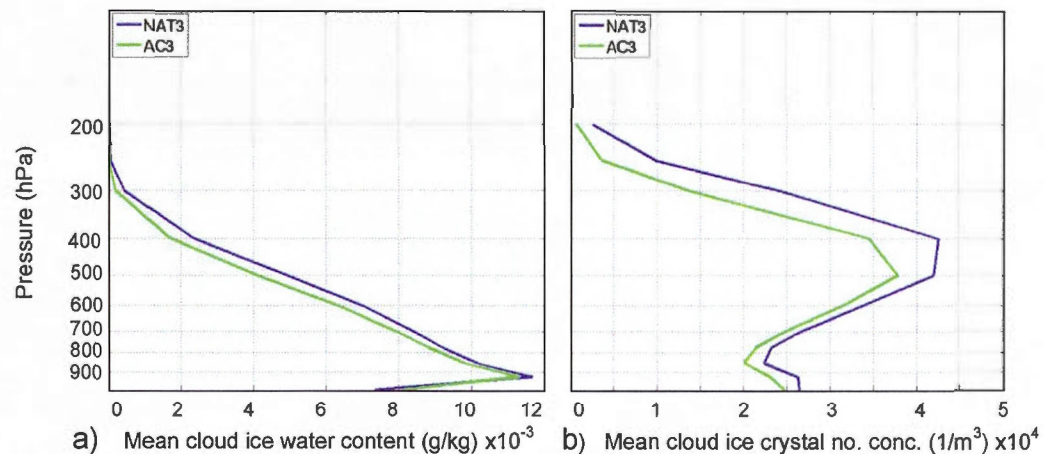


Figure 3.45: Vertical profiles of cloud ice (a) content ($\times 10^{-3}$ g/kg) and (b) ice crystal number concentration ($\times 10^4$ $1/m^3$) for aerosol scenarios AC3, NAT3 averaged over time and spatially averaged over a mask delimited by sea ice boundaries.

Figure 3.46 shows the January mean vertical profile of RH_i averaged over the sea-ice mask. At the lower troposphere between 1000 and 920 hPa, the RH_i in the AC3 scenario is equal to that of the NAT3 scenario and is lower in the mid and upper troposphere. The January mean RH_i negative anomaly over the mask delimited by sea ice boundaries peaks at -1.8 % at 850 hPa. This decrease in RH_i is due to the formation of ice crystals by contact freezing in the AC3 scenario. These ice crystals absorb the available water vapour in the troposphere and contribute to decrease the RH_i . The required threshold for deposition ice nucleation is therefore not reached as often as in the aerosol scenario NAT3. Figure 3.47 clearly shows that the difference in the ice crystal concentration is related to the difference in RH_i between AC3 and NAT3.

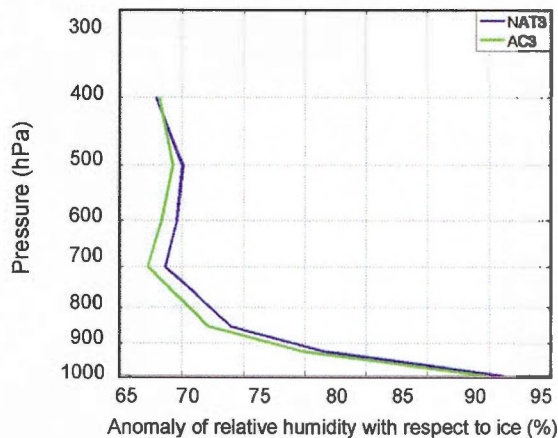


Figure 3.46: Vertical profile of the mean relative humidity with respect to ice (%) for aerosol scenarios NAT3 and AC3 averaged over time and spatially averaged over a mask delimited by sea ice boundaries.

Figure 3.47 shows the ice crystal number concentration anomaly as a function of RH_i anomaly. As discussed earlier, the negative RH_i anomaly is associated with negative ice crystal number concentration anomaly. Negative (positive) RH_i anomalies are associated to negative (positive) ice crystal number concentration.

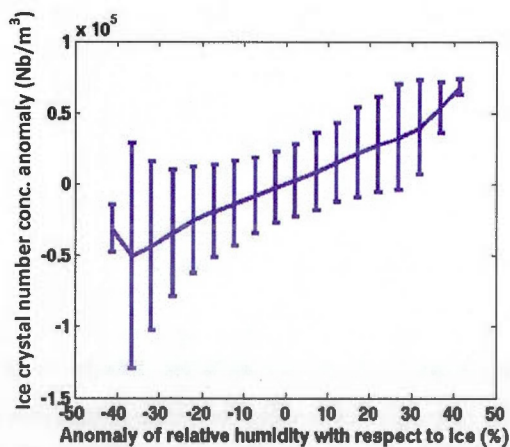


Figure 3.47: January daily mean of ice crystal number concentration ($1/m^3$) anomaly as a function of RH_i (averaged over 5% intervals) and spatially averaged over the sea-ice mask with the related standard deviation (vertical bars) when the anomaly is defined as the difference between AC3 and NAT3 (AC3-NAT3).

Figures 3.48a and b show the January mean vertical profile of liquid water content and water droplets number concentration averaged over the mask delimited by sea-ice boundaries. The liquid water concentration is slightly higher in the presence of the contact INs in the AC3 scenario compared to the NAT3 scenario throughout the troposphere especially between 900 and 940 hPa where the mixed-phase clouds are mostly found. The addition of the contact INs in the AC3 scenario has a very small impact on the liquid water content. The reason of the increase in the liquid water concentration at the presence of contact INs is explained in section 3.2.3. The differences between both scenarios for the cloud liquid droplet concentration are not related to either temperature or RH_i (figures not shown). It is in fact related to the Bergeron effect, which is reduced in the AC3 scenario compared to the NAT3 scenario due to the smaller ice crystal concentration that can absorb the water vapor from the evaporation of water droplets.

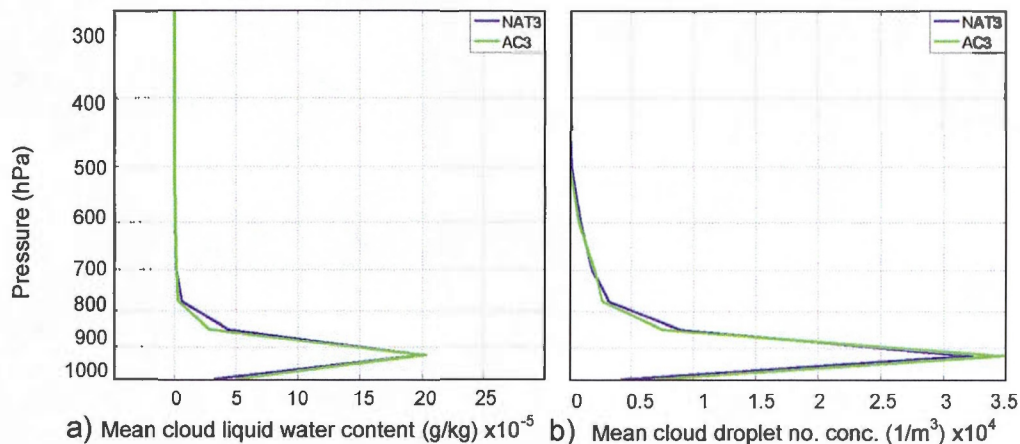


Figure 3.48: Vertical profiles of cloud liquid water (a) content ($\times 10^{-5}$ g/kg) and (b) liquid drop number concentration ($\times 10^4$ $1/m^3$) for AC3 and NAT3 aerosol scenarios averaged over time and spatially averaged over a mask delimited by sea ice boundaries.

Figures 3.49a and b show respectively January mean liquid and ice water path anomalies averaged over the Arctic sea-ice mask. The liquid water path anomaly is positive over the eastern and central Siberia, a great part of Mongolia, central and northern Greenland, Foxe Basin, central Arctic Ocean, Bering Sea, Kara Sea,

Labrador Sea and Scandinavia and is negative elsewhere. Values of these anomalies remain however small. The ice water path anomaly is negative over most of the Arctic with the largest values over the Kara and Barents Sea. These regions are warmer than the Central Arctic and are characterized by a large occurrence of mixed-phase clouds (e.g. Girard *et al.*, 2012). Contact ice nucleation is therefore more frequent over these areas due to the frequent presence of cloud liquid droplets. Results give a mean ice water path anomaly of -5.9×10^{-4} kg/m² and liquid water path anomaly of 2.7×10^{-5} kg/m² averaged over the sub-domain delimited by sea-ice boundaries. These results confirm the ice crystal loss and the small liquid water increase in the presence on contact INs in the AC3 aerosol scenario.

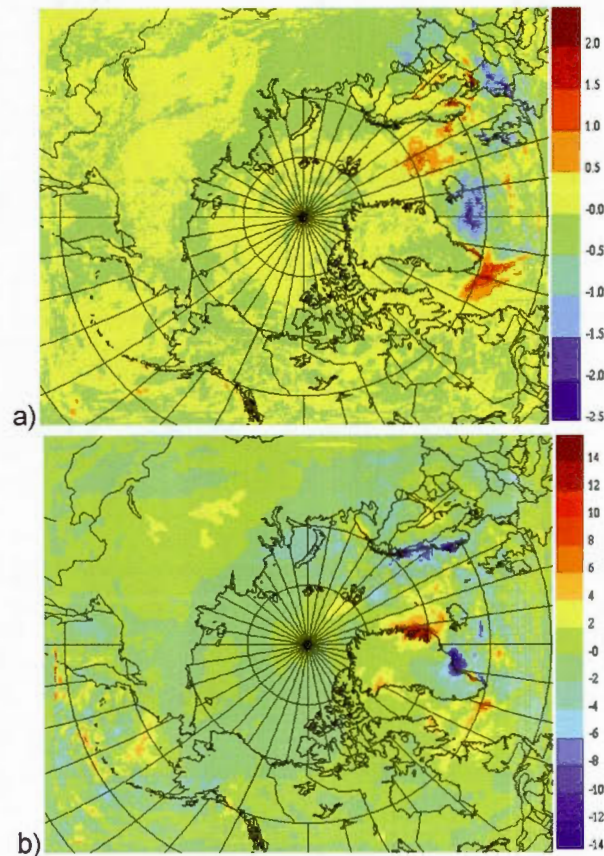


Figure 3.49: January mean (a) liquid water path anomaly ($\times 10^{-2}$ mm) and (b) ice water path anomaly ($\times 10^{-2}$ mm) in the Arctic when the anomaly is defined as the difference between AC3 and NAT3 (AC3-NAT3).

Figures 3.50a and b show January mean cloud radiative forcing anomalies respectively at the surface and at the TOA. The CRF anomalies are positive, ranging from 0 to 10 W m^{-2} at the surface and from 0 to 6 W m^{-2} at the TOA, over a vast region in the Arctic including Northern Canada, Central Siberia, Northern Greenland and a part of the Bering Sea. This anomaly is negative over the Central Arctic, the Alaska and Eastern Siberia with values ranging from 0 to -5 W m^{-2} at the surface and from 0 to -8 W m^{-2} at the TOA. Based on the dependency of the cloud forcing at the surface and at the TOA to the hydrometeors concentration, the reduction of the clouds ice water path due to the addition of contact INs in the AC3 scenario should cause a negative CRF anomalies at the surface and at the TOA over areas where

the cloud microstructure is the most affected by contact ice nucleation, which is the Barents and Kara Sea. Results are consistent with this idea with negative CRF anomaly over these regions of up to -10 W m^{-2} at the surface and -6 W m^{-2} at the TOA. However, when averaged over the sea-ice mask, the mean January negative ice water path anomaly of $-6 \times 10^{-4} \text{ mm}$ produces a very small negative cloud forcing anomaly of -0.2 W/m^2 at TOA and a negative CRF anomaly of -0.66 W/m^2 at the surface. These small averaged values are caused by positive CRF occurring in very cold areas where the LWP and IWP anomalies are very small. Positive CRF anomalies are therefore likely to be due to internal variability of the model. The statistical test performed on these results shows that the CRF anomalies at the surface are not statistically significant (see Figure D.7 in Appendix D for the pair 6). However, the negative CRF anomalies at the TOA over the Barents and Kara Sea are statistically significant (see Figure D.8 in Appendix D for the pair 6). Positive CRF anomalies at the TOA are not statistically significant. Therefore, these positive CRF anomalies should be interpreted as highly uncertain.

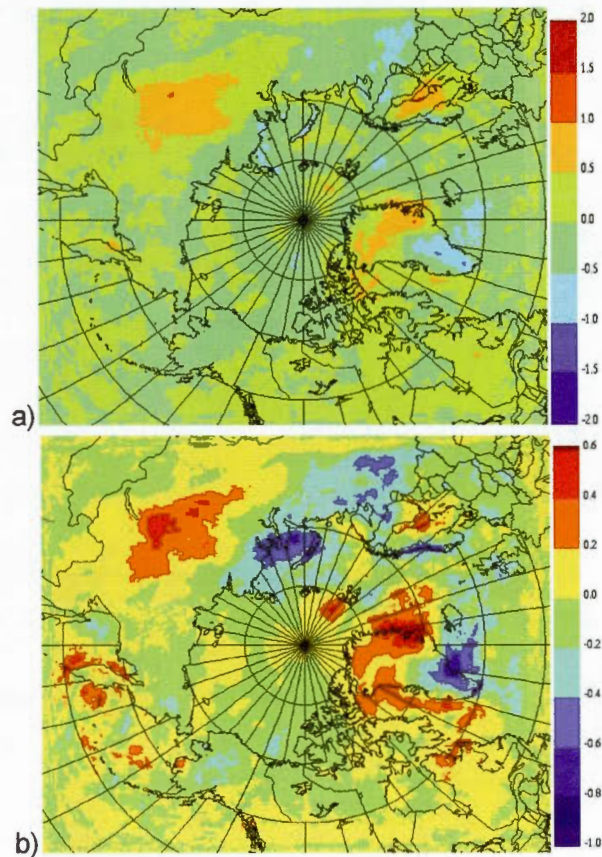
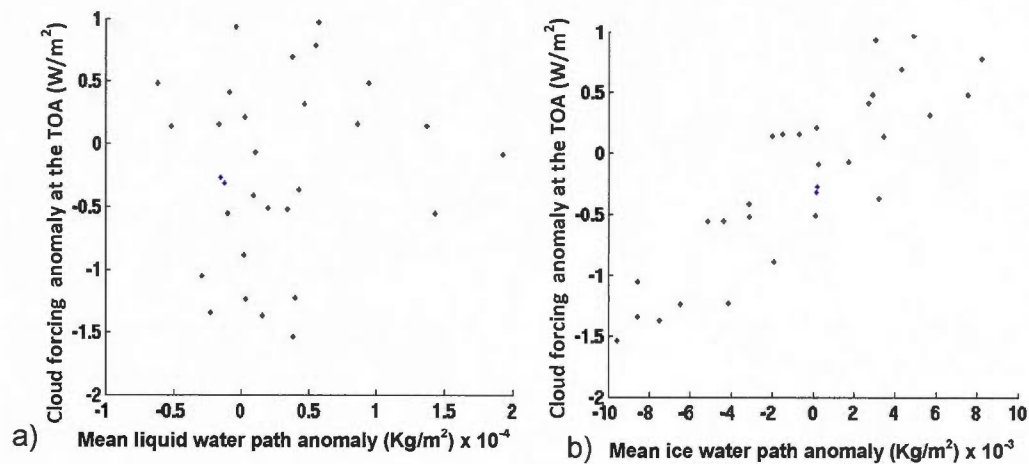


Figure 3.50: Mean January 2007 cloud forcing anomaly ($\times 10 \text{ W/m}^2$) at (a) the surface and at (b) the TOA over the Arctic when the anomaly is defined as the difference between AC3 and NAT3 (AC3-NAT3).

Figures 3.51a and b show the co-variation of cloud forcing anomaly at TOA to the vertically integrated ice and liquid water path anomalies. The small liquid water anomaly does not seem to be determinant for the CRF at the TOA. However, a stronger relationship is obtained with the ice water path. A variation of the IWP in the mid and upper levels contributes to change the atmospheric transmissivity and therefore affects the CRF at the TOA.



Figures 3.51: Pair 6 scatter plot of the daily mean cloud forcing anomaly of January 2007 at TOA as a function of daily mean vertically integrated (a) liquid water path anomaly ($\times 10^{-4}$ Kg/m²) and (b) ice water path anomaly ($\times 10^{-3}$ Kg/m²) averaged over the sub-domain delimited by sea ice when the anomaly is defined as the difference between AC3 and NAT3 (AC3-NAT3).

Figure 3.43 shows the mean January temperature anomaly at 850 hPa. This anomaly is positive over southeastern Siberia, North of Greenland, Baffin Sea, Greenland Sea, Northern part of the Barents Sea and the Arctic Ocean with values ranging mostly from 0 to 2 K and is negative elsewhere in the Arctic with a minimum up to -2 K over the Kara Sea. The regions with positive/negative temperature anomaly match to a great extent to the regions where CRF anomaly at the TOA or at the surface is positive/negative (see Figures 3.50 a,b).

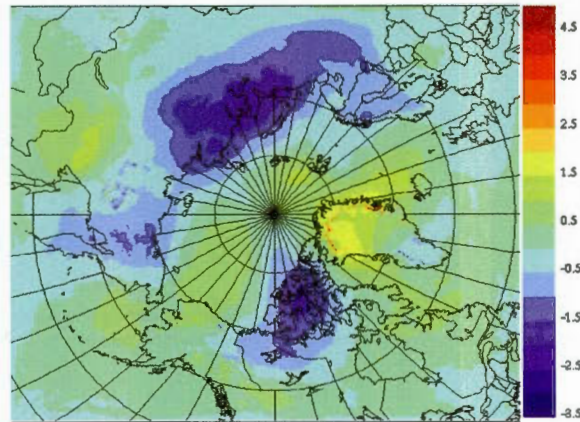


Figure 3.52: Mean January temperature anomaly over the Arctic at 850 hPa when the anomaly is defined as the difference between AC3 and NAT3 (AC3- NAT3).

Figure 3.53 shows the mean January vertical profile of the temperature of AC3 and NAT3 aerosol scenarios over the Arctic spatially averaged over the mask of sea-ice boundaries. The temperature vertical profile in the AC3 and NAT3 are very close together. These results show that the temperature anomaly can be regionally relatively important; however, when averaged over the whole Arctic, the temperature anomaly becomes negligible.

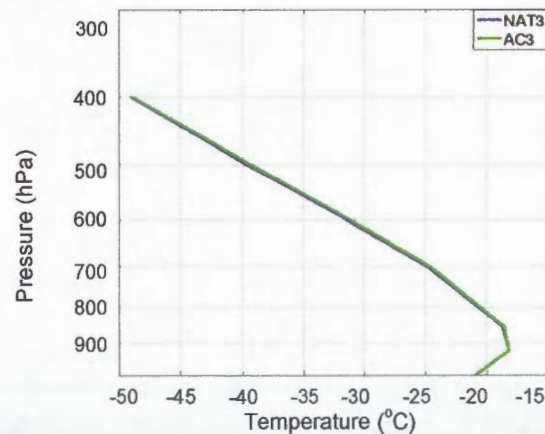


Figure 3.53: January 2007 mean temperature ($^{\circ}\text{C}$) vertical profiles averaged over a mask delimited by sea ice boundaries for aerosol scenarios NAT3 and AC3.

DISCUSSION AND CONCLUSIONS

The presence of intense low-pressure system centered over Iceland and an anticyclone over Siberia during the winter generates large-scale atmospheric circulation, which is very favourable to the transport of anthropogenic pollution from highly populated areas of northern Europe and north-eastern Asia to the North Pole. Most of these aerosols are highly acidic (Bigg, 1980).

Mineral dust particles are among the most abundant IN in the atmosphere. Many laboratory experiments on coated and uncoated mineral dust particles have been performed by Eastwood *et al.* (2008; 2009), Knopf and Koop (2006), Salam *et al.* (2007), Cziczo *et al.* (2009), Niedermeier *et al.* (2010) and Sullivan *et al.* (2010b). Results indicate that sulfuric acid coating on these INs substantially increases the onset ice supersaturation for ice nucleation. Ice nucleation occurs therefore at a much lower rate compared to uncoated dust particle. The coating effect on ice nucleation was also indirectly observed during the Arctic Gas and Aerosol Sampling Program (AGASP) by Borys (1989). In this study, the authors showed that the IN concentration is decreased by 3 to 4 orders of magnitude during highly polluted (Arctic haze) events (Borys, 1989).

Several modeling studies (Girard and Bekcic, 2005; Girard and Stefanof, 2007 and Girard *et al.*, 2012) have been set to investigate the impact of the acid sulfuric coating on INs on the wintertime Arctic clouds and energy budget. The results of these studies show that the acid coating reduces the nucleation rate over the acid coated INs forming relatively fewer and larger ice crystals that precipitate more often from the clouds. The resulting optically thinner clouds are more transparent to IR radiation and produce negative cloud forcing anomaly. This leads to a tropospheric cooling, which further promotes water vapor condensation and the reduction of the water vapor greenhouse effect. This effect is known as the dehydration-greenhouse

feedback that was hypothesised for the first time by Girard and Blanchet (1994; 1995).

This hypothesis has been investigated using 1D and 3D models (Girard and Bekcic, 2005; Blanchet and Girard, 2005; Girard and Stefanof, 2007; Girard *et al.*, 2012). All these modeling studies have confirmed the tropospheric cooling produced by the DGF.

In the most recent modeling study on the DGF by Girard *et al.* (2012), the ice nucleation is parameterized by the classical nucleation theory, which is a simplified parameterization of heterogeneous ice formation independent of physiochemical characteristics of aerosols in which all INs have identical surface properties with a single contact angle. Girard *et al.* (2012) also assumed that only deposition ice nucleation is altered by acidic coating. Although no laboratory experiment (set up too complex to make such experiments) has shown any alteration of acid coating on INs, it is very likely that the acid coating will alter this ice nucleation mode (personal communication).

A recent research study conducted by Wheelers *et al.* (2011) on the deposition freezing on mineral dust particles proves that the results obtained by classical nucleation theory with the assumption of a constant contact angle for all dust particles fail to fit the laboratory data. The authors have proposed a more refined parameterization than the single contact angle framework for CNT to incorporate the variability in the IN surface properties in order to better reproduce the laboratory experiments data in the climate models. In their approach, they assigned a distribution of contact angles to deposition INs where the probability of nucleation of each individual IN was defined by a normal probability distribution function (PDF) (Wheeler *et al.*, 2011; Marcolli *et al.*, 2007). In this approach, the nucleability of each single IN is equal over the entire surface but varies from particle to particle.

The purpose of this study is to assess the importance of contact nucleation in clean and acid polluted environments to investigate the probable acid coating effect on the contact ice nucleation on the wintertime Arctic clouds microstructure and

terrestrial energy budget. Also, the effect of more realistic PDF parameterisation of contact angles has been investigated in a clean environment through the simulations performed by the GEM-LAM model for January 2007.

In the present work, six sets of sensitivity test have been simulated to investigate the sensitivity of ice nucleating properties of kaolinite particles to the changes in ice formation condition and its impact on the properties of wintertime Arctic clouds. The first pair, which includes AC1 and NAT1 aerosol scenarios, investigates the effect of acid coating on the wintertime Arctic clouds in the presence of contact INs. The second pair, which includes AC3 and NAT1 aerosol scenarios, studies the effect of PDF parameterisation in an uncoated IN air mass on the Arctic clouds and radiative budget. The third pair, which includes AC2 and NAT2 aerosol scenarios, is similar to the pair 1 except that contact nucleation is absent. The pair 4, which includes AC1 and AC2 aerosol scenarios, studies the effect of including contact nucleation in an acid polluted environment. The pair 3, which includes NAT1 and NAT2 aerosol scenarios, studies the effect of the presence of contact nucleation on the properties of Arctic clouds in a clean environment. Finally, the pair 6, which includes AC3 and NAT3 aerosol scenarios, is similar to the pair 3 except that the PDF parameterization of contact angles is used instead of the single contact angle approach.

The results of the pairs 1, with a mean ice water path anomaly of -0.0155 kg/m^2 , mean liquid water path anomaly of 0.0079 kg/m^2 , mean negative cloud forcing anomaly of -0.8 W/m^2 at the TOA and a surface cooling of $0.89 \text{ }^\circ\text{C}$ in the acidified scenario, are consistent with the results obtained by Girard *et al.* (2012) with a mean ice water path anomaly of -0.0126 kg/m^2 , mean positive liquid water path anomaly of 0.0153 kg/m^2 , mean cloud forcing anomaly of -2.37 W/m^2 at the TOA and a mean surface cooling of $2.1 \text{ }^\circ\text{C}$.

The results of the pair 1 are consistent with Girard *et al.* (2012) with a mean decrease in ice water path of 0.0155 kg/m^2 and a mean increase of liquid water path of 0.0079 kg/m^2 in the acidified scenario compared to respectively ice water path

anomaly and liquid water path anomaly of -0.0126 kg/m^2 and 0.0153 kg/m^2 obtained by Girard *et al.*; mean negative cloud forcing anomaly of -0.8 W/m^2 at the top of the atmosphere compared to the cloud forcing at the TOA of -2.37 W/m^2 obtained by Girard *et al.* and a surface cooling of $0.89 \text{ }^\circ\text{C}$ near the surface compared to 2.1 obtained by Girard *et al.*

In the pair 2, the PDF parameterization with contact angles ranging from 4.9 to 33.2° (see equation 2.7) is compared to the original CNT framework with a single contact angle value of 12° . According to the normal PDF, the majority of aerosols have contact angles larger than single- α parameterization of contact angle of 12° calculated by classical nucleation theory. The onset RH_i for deposition freezing is a strong function of the contact angle with a clear trend of increasing RH_i with increasing contact angle. Thus the deposition ice nucleation is very efficient for dust particles with smaller contact angles that are in minority according to the PDF distribution function. As a result, fewer aerosols are capable to nucleate ice in PDF parameterization of contact angle and the nucleation rate of ice crystals in the deposition mode decreases. Therefore the ice water content and the ice crystal number concentration are smaller in the PDF parameterization compared to single- α parameterization.

Based on the dependency of IN nucleability to the RH_i threshold for deposition nucleation in the PDF parameterization, the ice crystals nucleate at almost all values of RH_i but in the single contact angle approach, the INs initiate deposition ice nucleation only after the RH_i reaches the threshold required for ice nucleation. One therefore expects that the nucleation of ice crystals in the AC3 scenario will be much more progressive. The reduced number of ice crystal in the PDF parameterization decreases the water vapor deposition rate on the ice crystals by Bergeron effect and results in an increase of the RH_i .

In the PDF parameterization, the fact that some ice crystals can nucleate at lower contact angles (in other words at lower ice supersaturation) prevents the saturation ratio to reach the liquid saturation point and reduces therefore the

activation of cloud droplets compared to single- α parameterization. Thus, the liquid water content and number concentration in single- α parameterization is larger than in PDF.

Based on the dependency of the CRF to the tropospheric hydrometeor concentration, a mean decrease of ice crystal and droplet concentrations in the PDF parameterisation of contact angle reduces the CRF at the surface and at TOA and results in a mean small tropospheric cooling of 0.3 K near the surface over the whole Arctic. This surface cooling is smaller than the cooling of the pair 1.

In the pair 3, the importance of contact nucleation is investigated in a clean environment. In the presence of contact ice nucleation, a part of the liquid water turns into ice by contact nucleation absorbing a part of the available water vapor in an ice supersaturated environment. This reduces the RH_i in the troposphere and reduces the deposition ice nucleation rate, which is highly dependent on RH_i . The decrease in the deposition IN number concentration is larger than the increase in contact IN concentration. Therefore adding contact aerosols reduces the total concentration of ice nucleus and contributes to reduce the ice crystal concentration. The decreased ice crystal concentration increases the saturation with respect to water and limits the liquid water evaporation by Bergeron effect. This results in an increase of the liquid water concentration in the troposphere. The decrease of tropospheric ice crystal concentration in a clean air mass reduces slightly the cloud forcing at the surface and at the TOA and do not have a considerable effect on the tropospheric temperature. It should be noted that despite the fact that the temperature anomaly is so small in this pair but the temperature anomaly can be regionally relatively important with a cooling of more than 1 K over the Barents Sea.

In the pair 4, the effect of contact ice nucleation is investigated in a polluted environment (acid-coated INs). Just like the pair 3, by adding contact nucleation aerosols, a part of the water droplets nucleate ice upon contact with contact INs ice crystals formed in contact mode grow larger by Bergeron effect and prevent the air mass to reach the ice supersaturation required for deposition nucleation. This

deactivates a part of deposition INs and consequently the total ice crystal concentration in the troposphere. However, the ice crystal concentration decrease of the acid coated INs is lower than the ice crystal decrease due to the present of contact INs obtained in the pair 3 (NAT1 and NAT2). In NAT1, the presence of contact IN contributes to decrease the variability of the cloud ice supersaturation. Therefore, the ice nucleation events by deposition are less frequent. In the AC1 scenario, same argument is true for the pair 4 except that due to the acid coating on INs and the higher onset ice supersaturation required for deposition ice nucleation, the nucleation rate in AC2 is much smaller than in the NAT2 aerosol scenario. This shows that the presence of the contact INs in an acid polluted environment has a very small effect on the cloud microstructure in the troposphere.

Results show small positive CRF anomalies at the surface and at the TOA. Because of the small ice and liquid water path anomalies in the pair, these CRF anomalies are not dependant to the liquid and ice water path anomalies. These small CRF anomalies produce a slight increase in the tropospheric temperature of less than 0.5 K in the lower troposphere and negligible temperature anomalies at higher altitudes.

The pair 5 and pair 1 are similar except that contact nucleation is absent in pair 5. The cloud microstructure alteration by acid coating in this pair is almost the same as in the pair 1 and reduced concentration of total active INs contribute to reduce the ice crystal concentration and the ice content in the troposphere. The reduced number of ice crystals takes up less water vapor in the acidified scenario increasing the tropospheric RH_i . It is noteworthy to mention that the decrease of ice crystal concentration in the pair 5 is slightly larger than in the pair 1. The reason is the absence of contact INs in the pair 5 that increases the RH_i to the onset required for deposition nucleation activating a part of deposition INs that compensate in part the contact INs deactivation. The same thing happens in the acidified environment except that since the acid coated deposition INs require higher RH_i onset to initiate the deposition ice nucleation, the compensation of deactivated contact INs by the activated of deposition INs are slightly less stronger. The reduced number of ice

crystals combined by the increased supersaturation with respect to water limits the Bergeron effect and decrease the water evaporation rate in the troposphere increasing the tropospheric liquid drop concentration and water content. Here the increase in the liquid water number concentration in the pair 5 is slightly lower than in the pair 1, the reason is again the absence of contact INs in the pair 5 that increases the ice crystals in the troposphere evaporate more liquid water in the clear scenario than in the acidified scenario compared to the pair 1.

The optically thinner and more transparent mid and high clouds and the thicker and colder mix-phase clouds formed in the acidified environment increases the upward IR emission to the outer space leading into the a negative cloud radiative forcing anomaly and a decrease in the temperature at all pressure levels.

The effect of acid coating in both pair 1 and 3 are similar suggesting that the contribution of contact INs on the ice formation procedure in the clouds is very weak (specially in the acidified environment) and do not have an important effect in the cloud microstructure.

Finally, the pair 6 is similar to pair 3 except that here the contact angle is distributed according a normal PDF. Following the same argumentation used for pair 3, the presence of contact aerosols contribute to reduce the tropospheric RH_i . Therefore the onset RH_i for deposition ice nucleation is not reached as often as in aerosol scenario AC3. The cloud liquid droplet concentration is not related to either temperature or RH_i but is related to the Bergeron effect, which is reduced at the presence of contact INs in the AC3 aerosol scenario due to the smaller ice crystal concentration. The activation of the contact INs in the AC3 aerosol scenario has a very small impact on the liquid water content and liquid drop number concentration. It increases them slightly in the presence of the contact INs throughout the troposphere especially between 900 and 940 hPa where the mixed-phase clouds are mostly found.

Based on the dependency of the cloud forcing at the surface and at the TOA to the hydrometeors concentration, the smaller ice water path due to the addition of

contact INs in the AC3 scenario the clouds are more transparent towards the IR radiation and produce a negative the CRF anomaly at the surface and at the TOA. However, a much less stronger relationship is obtained with the liquid water path since the co-variation of CRF at the TOA with the liquid water concentration shows that the small liquid water anomaly does not have an effect on the CRF at the TOA.

Based on the direct dependency between the temperature anomaly and the CRF anomaly the temperature anomaly can be regionally relatively important; however when averaged over the whole Arctic the mean temperature vertical profiles in both AC3 and NAT3 in the pair 6 are very close together suggesting a negligible temperature anomaly throughout the troposphere.

In conclusion, according to the results of this research, the contact ice nucleation has a very small effect on the wintertime (January, February, March) Arctic cloud microstructure in a non-polluted environment and an even more negligible effect in an acid polluted environment. Also, the decrease of the ice crystals concentration in the PDF parameterization decreases slightly the cloud forcing and leads to a very slight decrease of the temperature. Therefore the PDF parameterization does not have a great effect of the cloud microstructure and the energy budget. Finally, the results obtained in this work should be investigated further using different climate models and different microphysics schemes to confirm this hypothesis and to better understand the mechanisms involved in contact nucleation and its effect on the wintertime arctic clouds.

APPENDIX A

The difference of geopotential height at 500 hPa, MSLP and temperature at 850 hPa between the ECMWF analysis and the model output averaged over January 2007 for aerosol scenarios NAT2, NAT3, AC1, AC2 and AC3

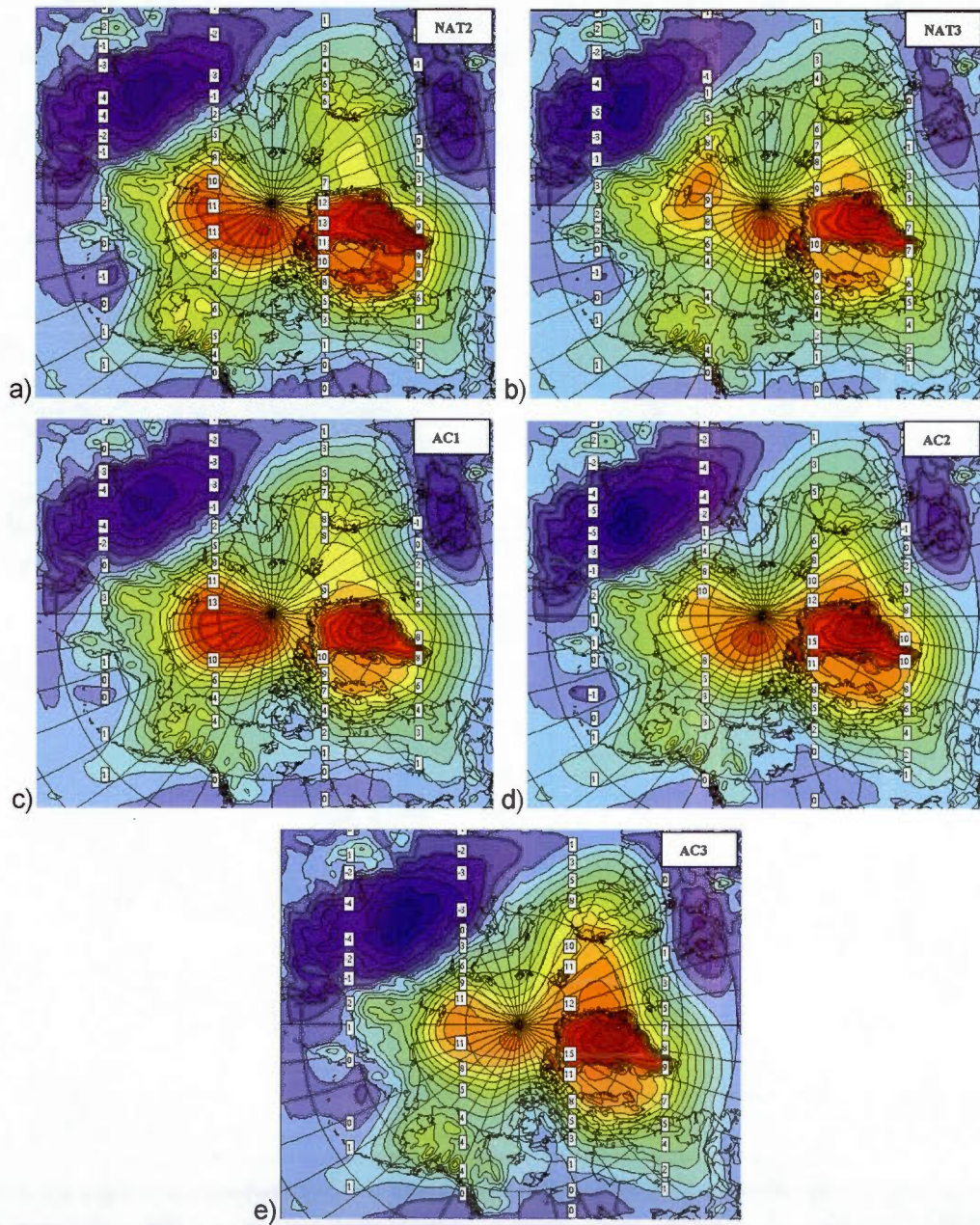


Figure A.1: The difference of geopotential height at 500 hPa between the ECMWF analysis and the model output averaged over January 2007 for aerosol scenarios (a) NAT2, (b) NAT3, (c) AC1, (d) AC2 and (e) AC3 averaged on January 2007.

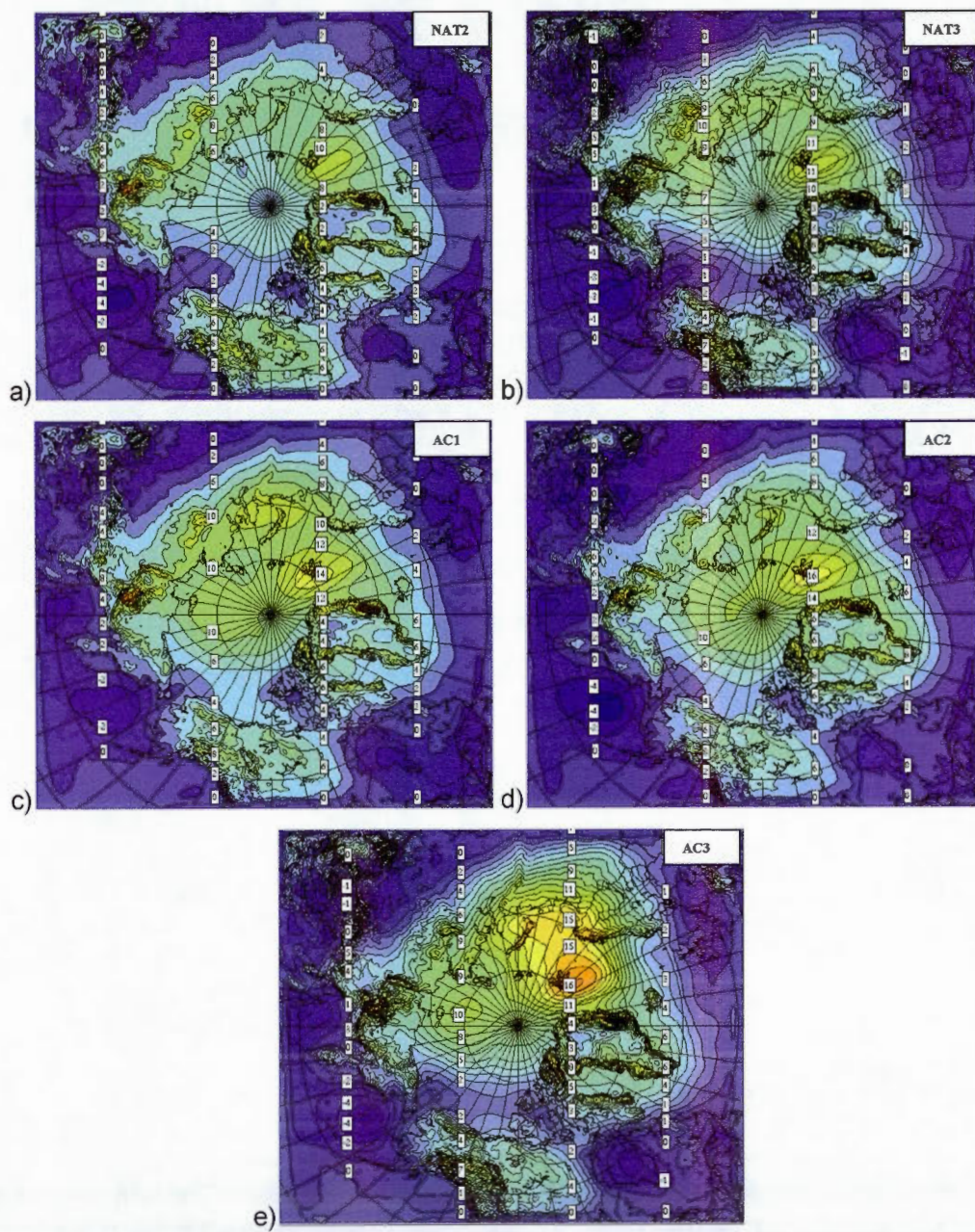


Figure A.2: The difference of MSLP between the observations from ECMWF and the model output for scenarios (a) NAT2, (b) NAT3, (c) AC1, (d) AC2 and (e) AC3 averaged on January 2007.

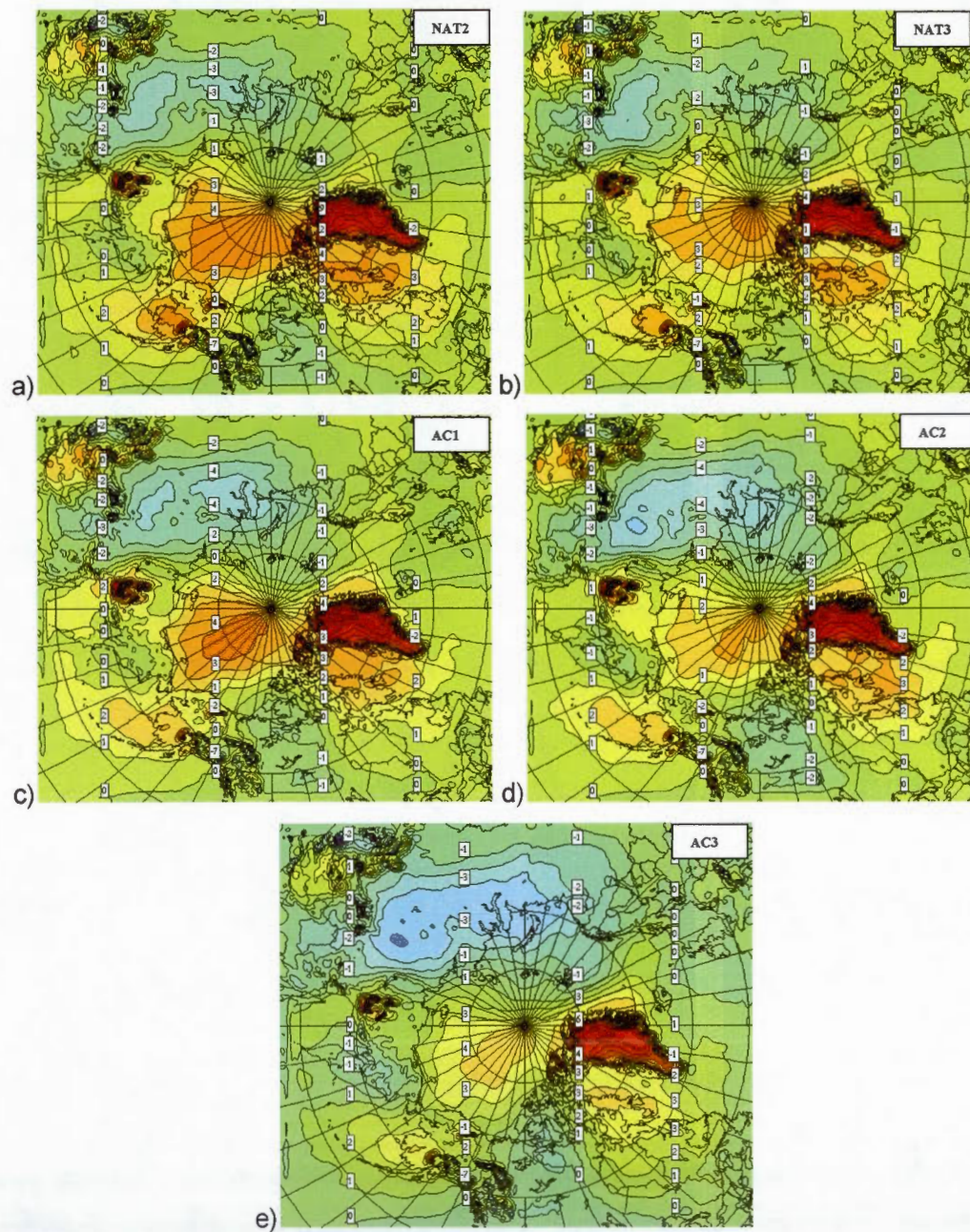


Figure A.3: The difference of temperature at 850 hPa between the observations from ECMWF and the model output averaged over January 2007 for aerosol scenarios (a) NAT2, (b) NAT3, (c) AC1, (d) AC2 and (e) AC3 averaged on January 2007.

APPENDIX B

Student t-test

The statistical test t_s which determines the value of the Student's t distribution for a desired confidence level is given by the following equation (Bélisle and Desrosiers, 1983):

$$t_s = \frac{(\overline{X}_{ptb} - \overline{X}_{ref}) - (\mu_{ptb} - \mu_{ref})}{\sqrt{\frac{1}{n_{ref}} + \frac{1}{n_{ptb}}} \sqrt{\frac{(n_{ref} - 1)s_{ref}^2 + (n_{ptb} - 1)s_{ptb}^2}{n_{ref} + n_{ptb} - 2}}} = T_{n_{ref} + n_{ptb} - 2; \gamma} \quad (\text{B.1})$$

The indices ref and prt means the reference and perturbed cases, respectively. μ_{ptb} and μ_{ref} are the real population means, s_{ptb}^2 and s_{ref}^2 represents the variances of the ensemble of respectively n_{ptb} and n_{ref} elements. These variances are unknown but are assumed to be equal; finally, \overline{X}_{ptb} and \overline{X}_{ref} are the spatial sample means of variable X defined by the following equation:

$$\overline{X} = \frac{\sum_{i=1}^{N_x} \sum_{j=1}^{N_y} \overline{X}_{i,j}}{N_x \cdot N_y} \quad (\text{B.2})$$

in which N_x and N_y are respectively the number of grid points in x and y directions.

Since $n_{ref} = n_{ptb} = n$, equation (B.1) can be rewritten as :

$$t_s = \frac{(\overline{X}_{ptb} - \overline{X}_{ref}) - (\mu_{ptb} - \mu_{ref})}{\left(\frac{s_{ptb}^2 + s_{ref}^2}{n} \right)^{\frac{1}{2}}} \quad (\text{B.3})$$

B.2 Hypothesis test and determining significant area

The statistical test of the hypothesis is a formal process which uses the information from the samples to decide which of the two hypotheses, null hypothesis or alternative hypothesis is true. The alternative hypothesis H_a , generally describes the range of possibilities that can be true if H_0 is rejected.

The first step would be to identify and formulate the null and alternative hypotheses:

- Null hypothesis (H_0) assumes that the difference between two ensemble means is equal to zero: $\mu_{prb} - \mu_{ref} = 0$
- Alternative hypothesis (H_a) supposes that the difference between two ensemble means is not zero: $\mu_{prb} - \mu_{ref} \neq 0$

These assumptions help to identify the areas where the anomaly, the difference of the given variable between perturbed and reference ensemble, is statistically significant.

At this step it is assumed that the difference between the mean of the two ensembles is zero or in other words, the null hypothesis is true. Therefore the t-test is redefined according to equation (B.3) in the context of the null hypothesis to check the validity of the H_0 hypothesis.

$$t_s = \frac{(\overline{X}_{ptb} - \overline{X}_{ref})}{\left(\frac{S_{ptb}^2 + S_{ref}^2}{n}\right)^{1/2}} \quad (\text{B.4})$$

Assuming $T_{n_{ref}+n_{ptb}-2;\gamma}$ to be the critical Student distribution value associated with degree of freedom of $n_{ref}+n_{dst}-2$ in table B.1, H_0 is rejected if:

$$t_s > T_{n_{ref}+n_{ptb}-2;\gamma/2} \text{ or } t_s < -T_{n_{ref}+n_{ptb}-2;\gamma/2}$$

So for all the grid points for which the condition $t_s > T_{n_{ref}+n_{ptb}-2;\gamma/2}$ or $t_s < -T_{n_{ref}+n_{ptb}-2;\gamma/2}$ is satisfied, the difference between two samples mean values is statistically significant with a confidence level of $1-\gamma$.

In this work, the level of statistical confidence is 95% ($1-\gamma=0.95$). According to table B.1, for two ensembles of ten simulations and a confidence level of 95%, the critical student test value equals 2.201. Thus the null hypothesis is true when the following condition is satisfied: $H_0: \{-2.201 \leq t_s \leq 2.201\}$

When the value of the distribution (t_s) is outside the range satisfying the null hypothesis, i.e. $t_s > T_{n_{ref}+n_{ptb}-2;\gamma/2}$ or $t_s < -T_{n_{ref}+n_{ptb}-2;\gamma/2}$, the null hypothesis is rejected and therefore the alternative hypothesis (H_a) is true. i.e. the anomaly is non-zero and is significant with a confidence level of $1-\gamma = 0.95$.

These criteria for determining critical regions allow distinguishing the regions where the anomaly is significant. Figure 2.2 illustrates an example of the Student t-test applied to the field of the RH_i at 850 hPa for NAT1 and AC1 aerosol scenarios over the integration domain during January 2007 (see Appendix B for student t-test results applied to other variable during January 2007).

The significant regions are showed by grid points for which the ratio of the absolute value of the statistic test over the critical value at a 95% confidence is

smaller than 1 or $\left| \frac{T_{n_{ref}+n_{ptb}-2, \gamma/2}}{t_s} \right| < 1$ (gray areas) and the non-significant regions are

represented by grid points for which this ratio is greater than 1 or $\left| \frac{T_{n_{ref}+n_{ptb}-2, \gamma/2}}{t_s} \right| > 1$

(white areas).

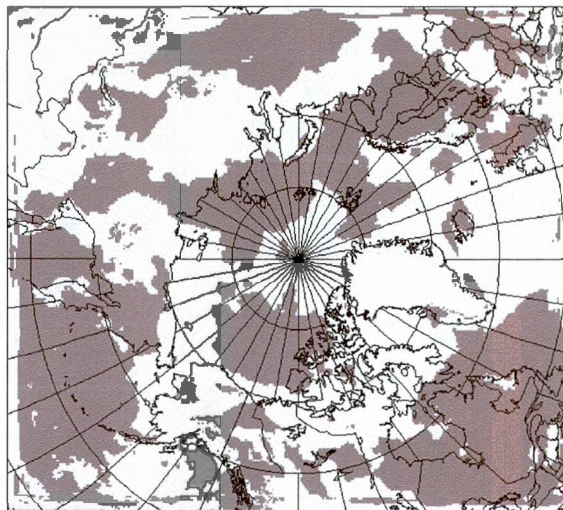


Figure B.1: Statistically significant area (gray) for RH_i at 850 hPa for January 2007 for aerosol scenario NAT1 and AC1 where results are valid with a confidence level of 95%.

This is seen in this figure that the some sectors of the Arctic including Kara Sea, Barents Sea, Labrador Sea, the Arctic Ocean at the North of Canada and North Atlantic Ocean at the East of Canada are significant areas and we are able to study the RH_i anomaly over these regions.

APPENDIX C

Student t table

Table C.1: Student t table

Degree of freedom $n_{\text{ref}}+n_{\text{dst}}-2$	$\gamma/2$					
	0.1	0.05	0.025	0.01	0.005	0.0025
1	3.078	6.314	12.706	31.821	63.657	636.619
2	1.886	2.920	4.303	6.965	9.925	31.598
3	1.638	2.353	3.182	4.541	5.841	12.941
4	1.533	2.132	2.776	3.747	4.604	8.610
5	1.476	2.015	2.571	3.365	4.032	4.032
6	1.440	1.943	2.447	3.143	3.707	5.959
7	1.415	1.895	2.365	2.998	3.499	5.405
8	1.397	1.860	2.306	2.896	3.355	5.041
9	1.383	1.833	2.262	2.821	3.250	4.781
10	1.372	1.812	2.228	2.764	3.169	4.587
11	1.363	1.796	2.201	2.718	3.106	4.437
12	1.356	1.782	2.179	2.681	3.055	4.318
13	1.350	1.771	2.160	2.650	3.012	4.221
14	1.345	1.761	2.145	2.624	2.977	4.140
15	1.341	1.753	2.131	2.602	2.947	4.073
16	1.337	1.746	2.120	2.583	2.921	4.015
17	1.333	1.740	2.110	2.567	2.898	3.965
18	1.330	1.734	2.101	2.552	2.878	3.922
19	1.328	1.729	2.093	2.539	2.861	3.883
20	1.325	1.725	2.086	2.528	2.845	3.850
21	1.323	1.721	2.080	2.518	2.831	3.819
22	1.321	1.717	2.074	2.508	2.819	3.792
23	1.319	1.714	2.069	2.500	2.807	3.767
24	1.318	1.711	2.064	2.492	2.797	3.745
25	1.316	1.708	2.060	2.485	2.787	3.725
26	1.315	1.706	2.056	2.479	2.779	3.707
27	1.314	1.703	2.052	2.473	2.771	3.690
28	1.313	1.701	2.048	2.467	2.763	3.674
29	1.311	1.699	2.045	2.462	2.756	3.659
30	1.310	1.697	2.042	2.457	2.750	3.646
40	1.303	1.684	2.021	2.423	2.704	3.551
60	1.296	1.671	2.000	2.390	2.660	3.460
120	1.289	1.658	1.980	2.358	2.617	3.373
x	1.282	1.645	1.960	2.326	2.576	3.291

APPENDIX D

Maps of significant zones for temperature anomaly, relative humidity with respect to ice anomaly, ice water content anomaly, liquid water content anomaly, ice crystal concentration anomaly, liquid drop concentration anomaly and cloud forcing at the TOA for all six pairs of study

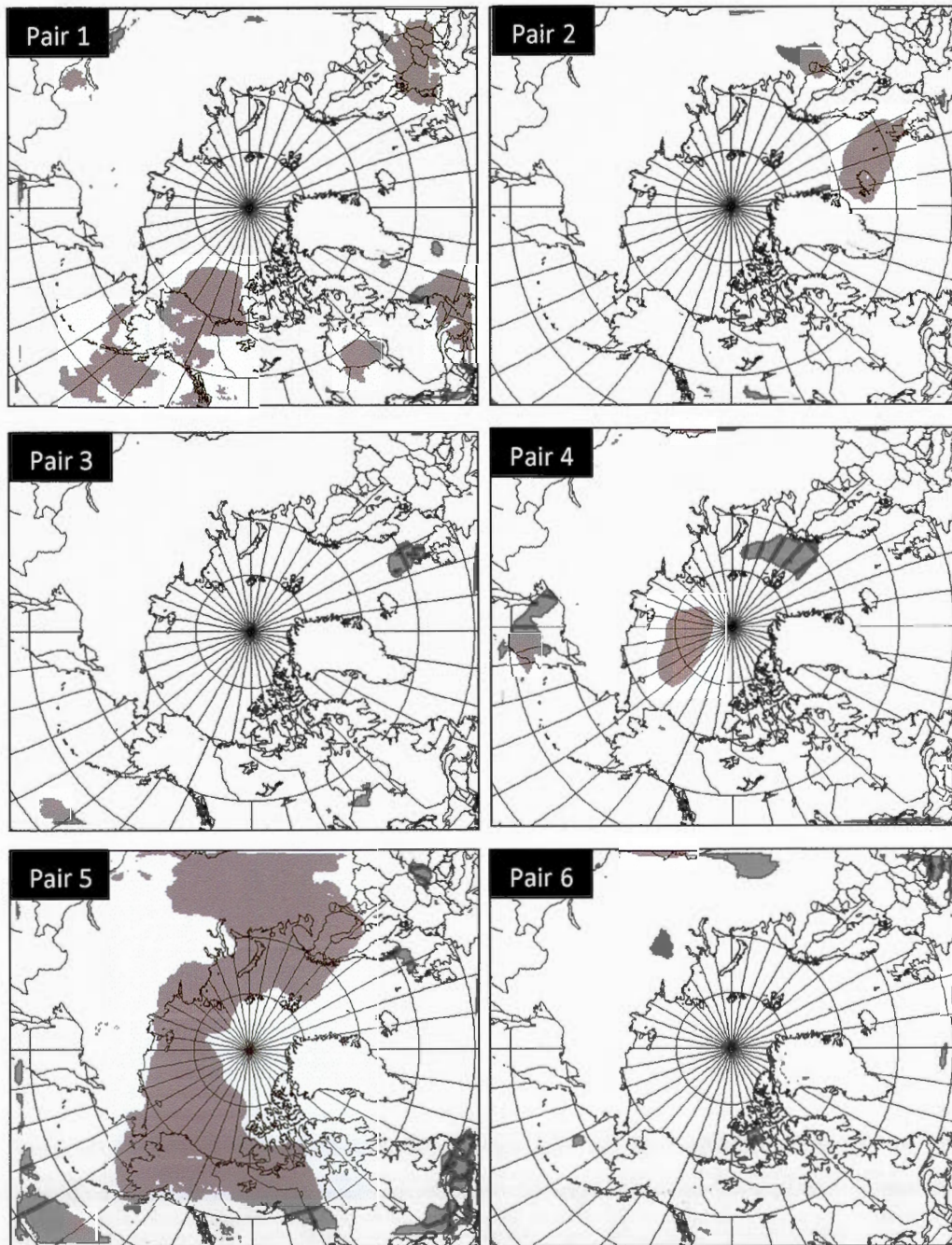


Figure D.1: Significant area for temperature anomaly for January 2007 for all six pairs calculated using the Student t-test. The gray areas indicate significant zone with a confidence level of 95%.

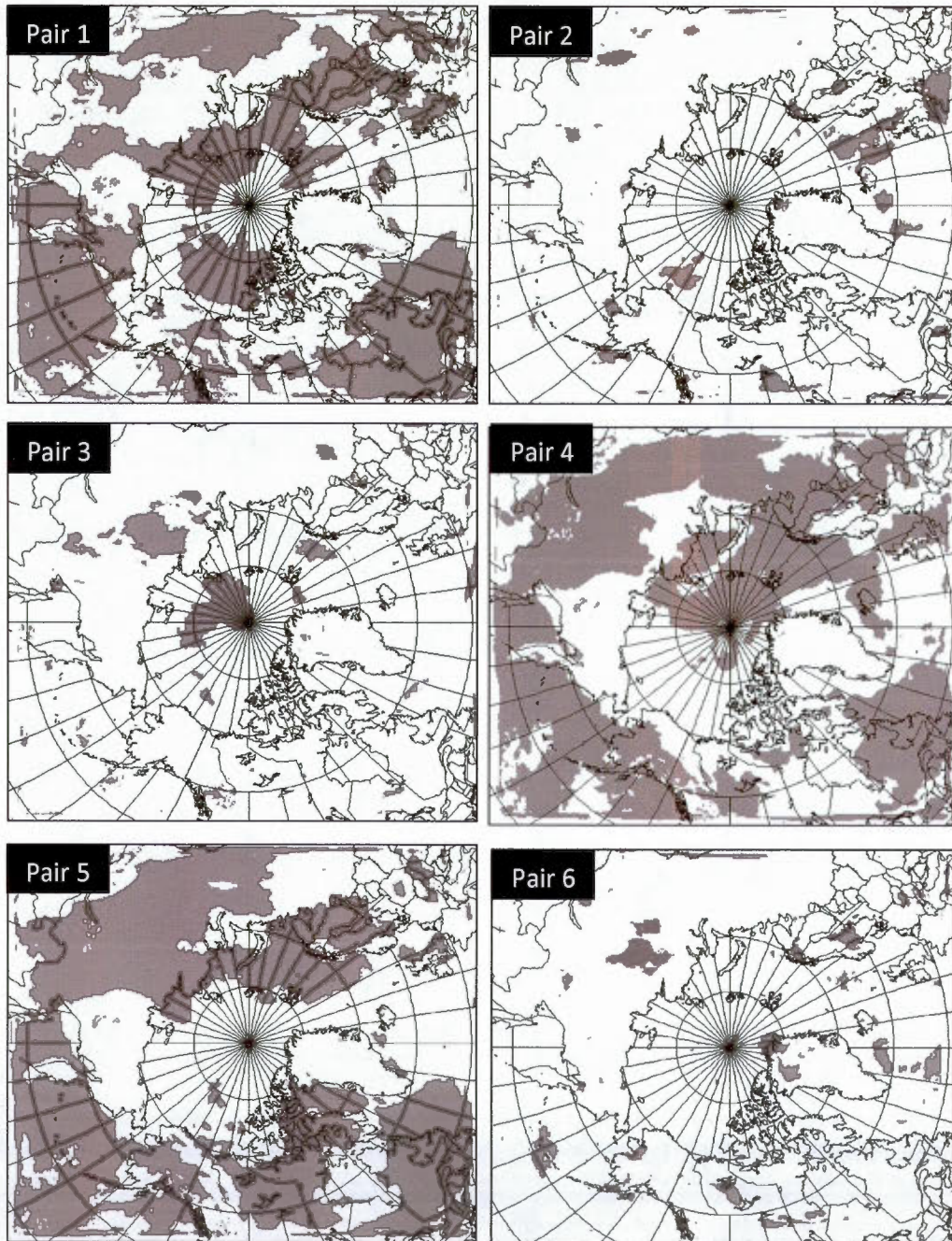


Figure D.2: Significant area for anomaly of relative humidity with respect to ice for January 2007 for all six pairs calculated using the Student t-test. The gray areas indicate significant zone with a confidence level of 95%.

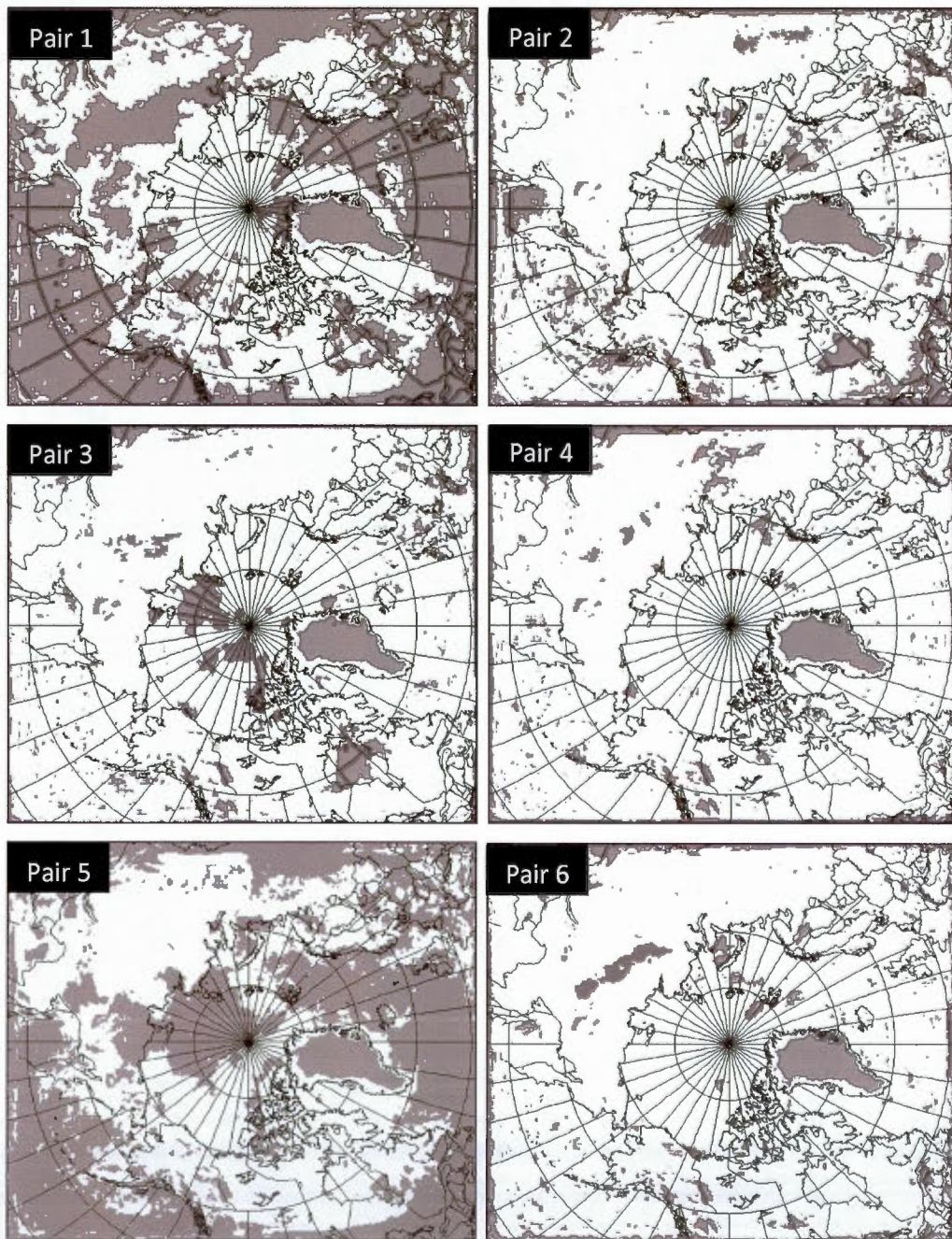


Figure D.3: Significant area for anomaly of ice water content for January 2007 for all six pairs calculated using the Student t-test. The gray areas indicate significant zone with a confidence level of 95%.

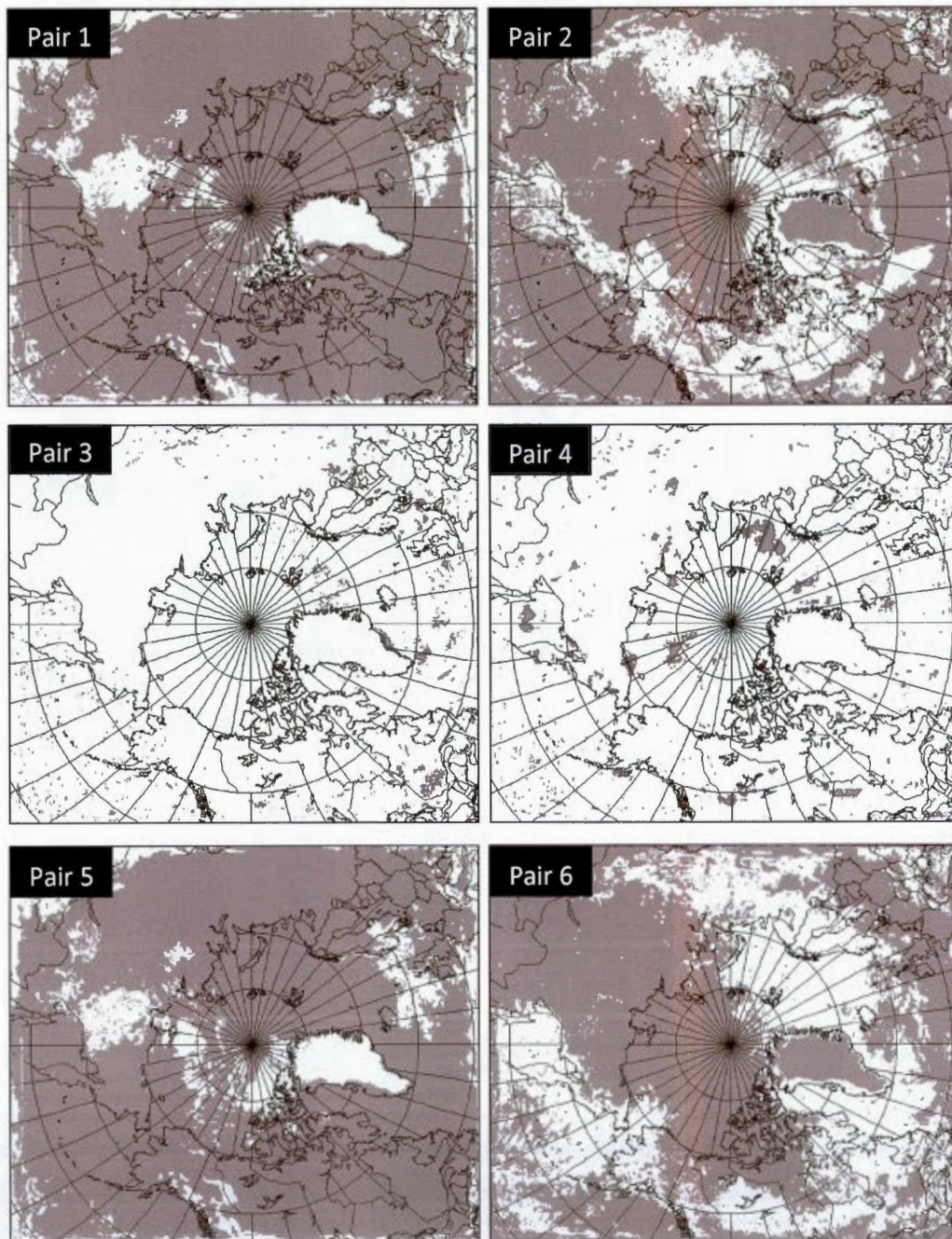


Figure D.4: Significant area for anomaly of liquid water content for January 2007 for all six pairs calculated using the Student t-test. The gray areas indicate significant zone with a confidence level of 95%.

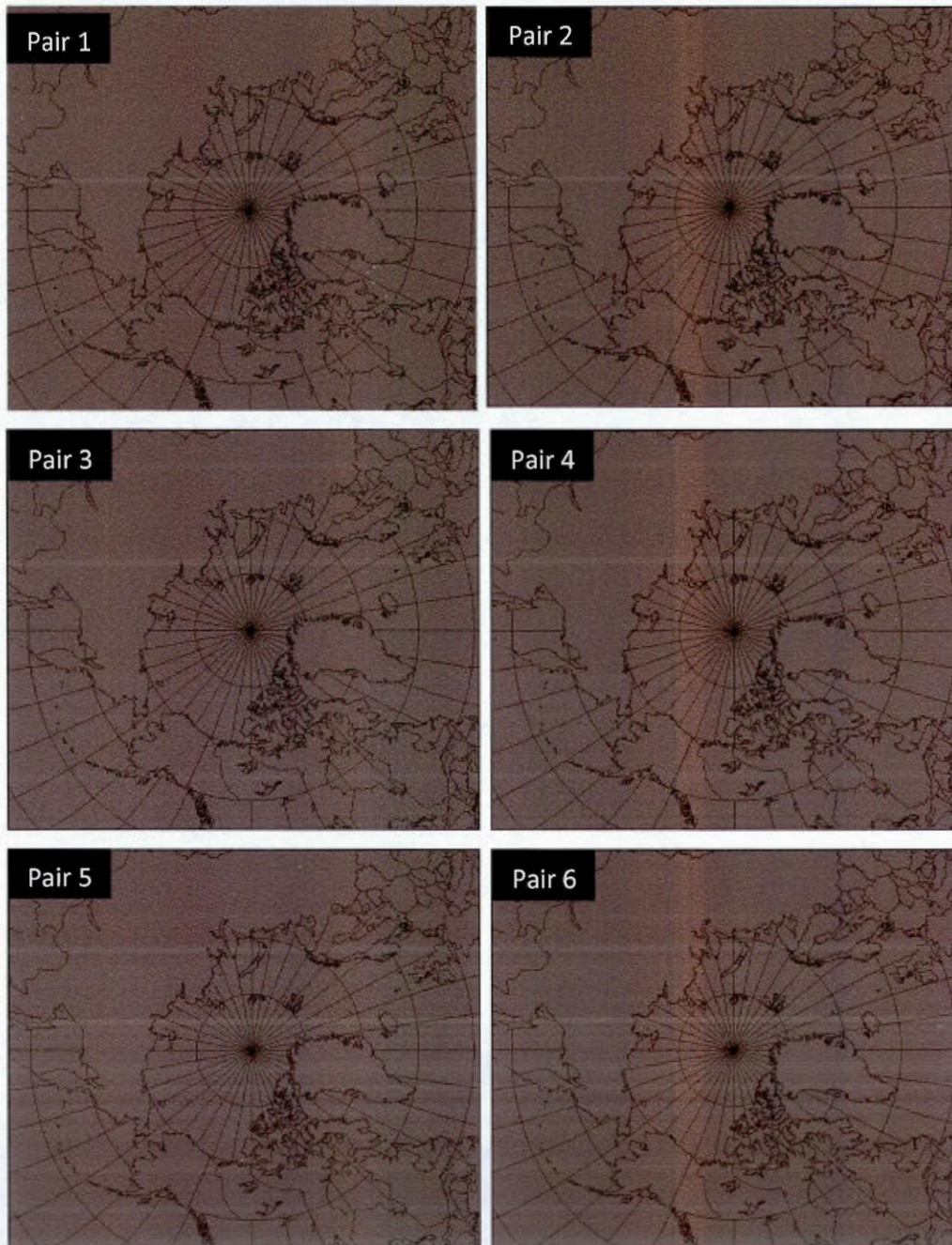


Figure D.5: Significant area for anomaly of ice crystal concentration for January 2007 for all six pairs calculated using the Student t-test. The gray areas indicate significant zone with a confidence level of 95%.

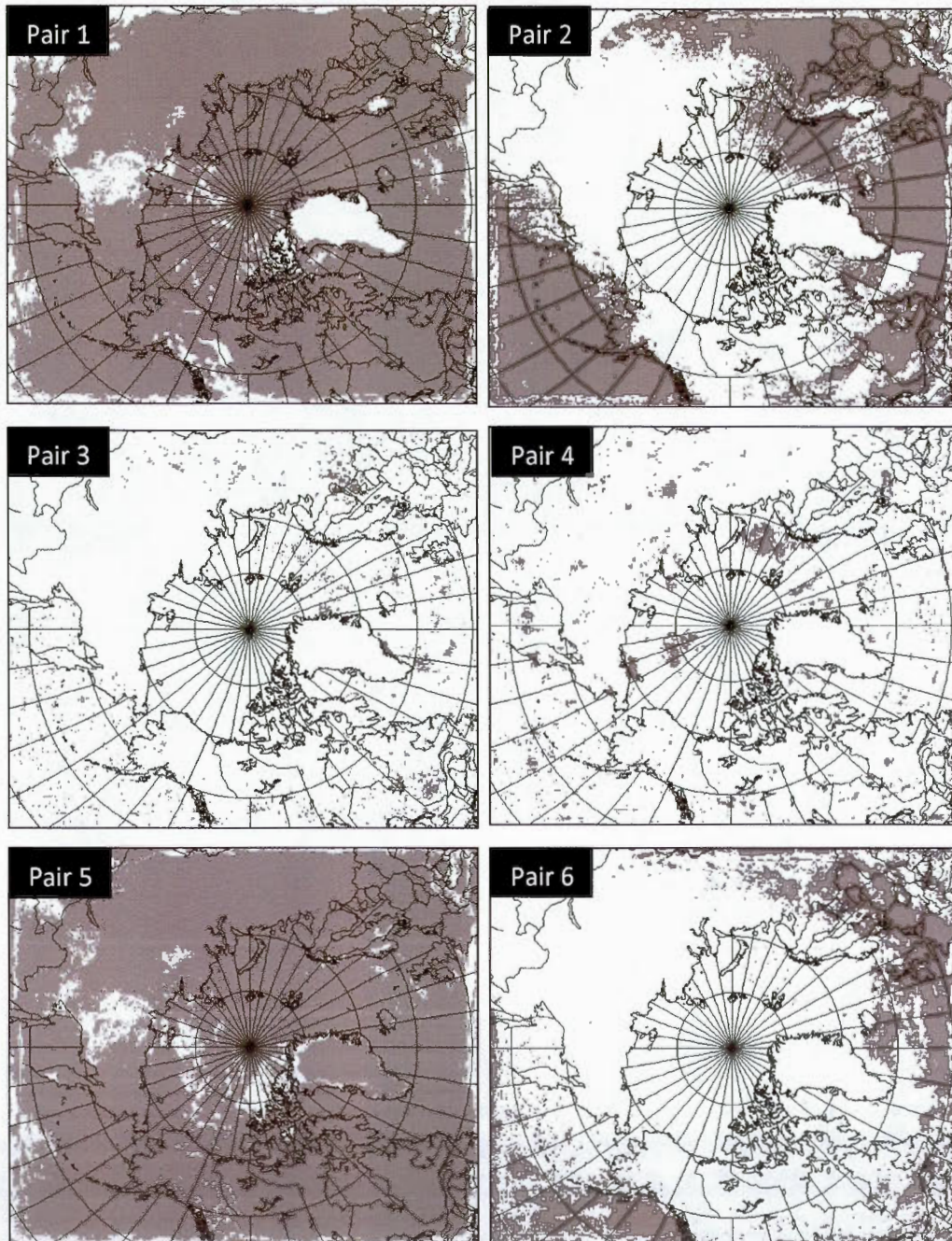


Figure D.6: Significant area for anomaly of liquid drop concentration for January 2007 for all six pairs calculated using the Student t-test. The gray areas indicate significant zone with a confidence level of 95%.

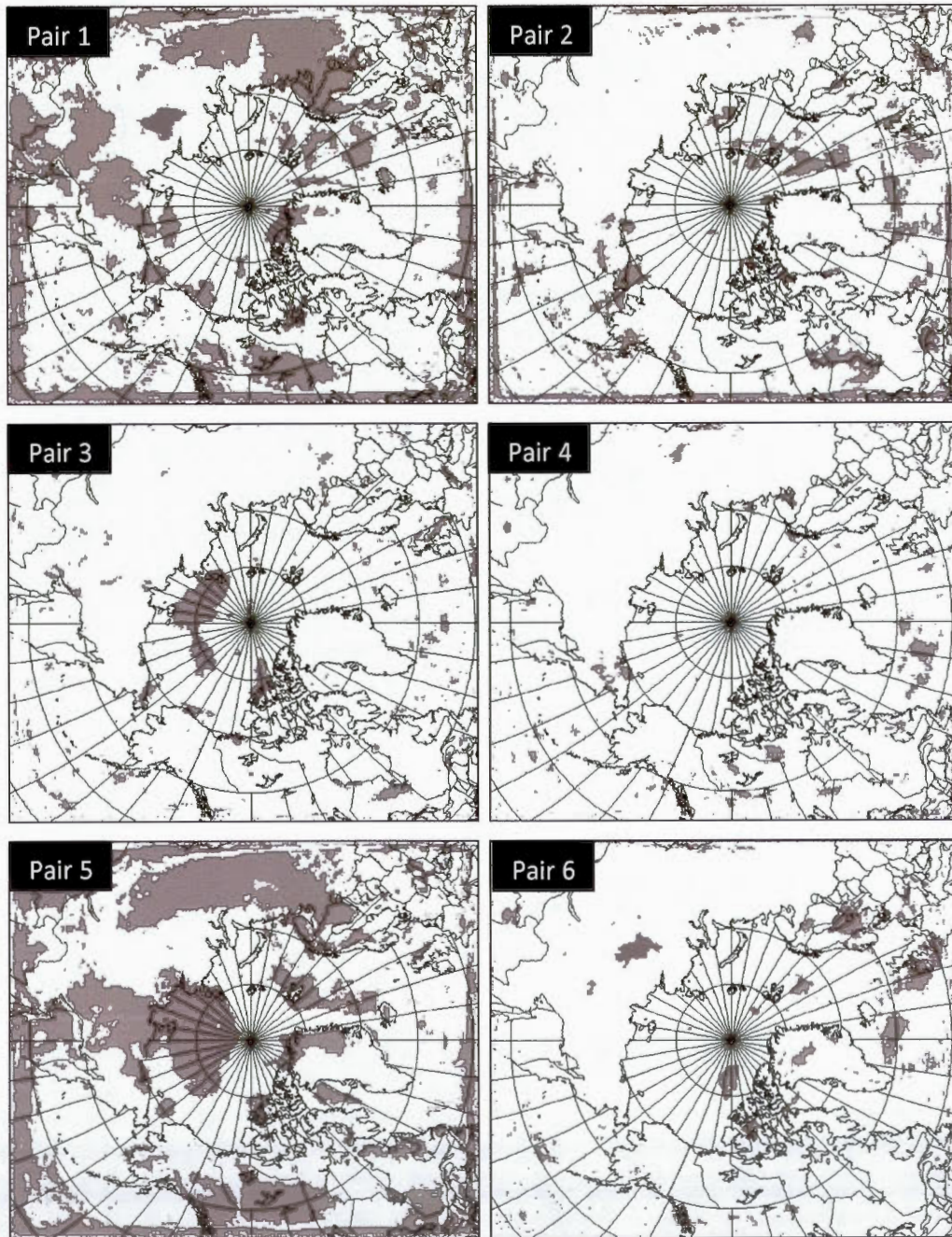


Figure D.7: Significant area for anomaly of cloud forcing at the surface for January 2007 for all six pairs calculated using the Student t-test. The gray areas indicate significant zone with a confidence level of 95%.

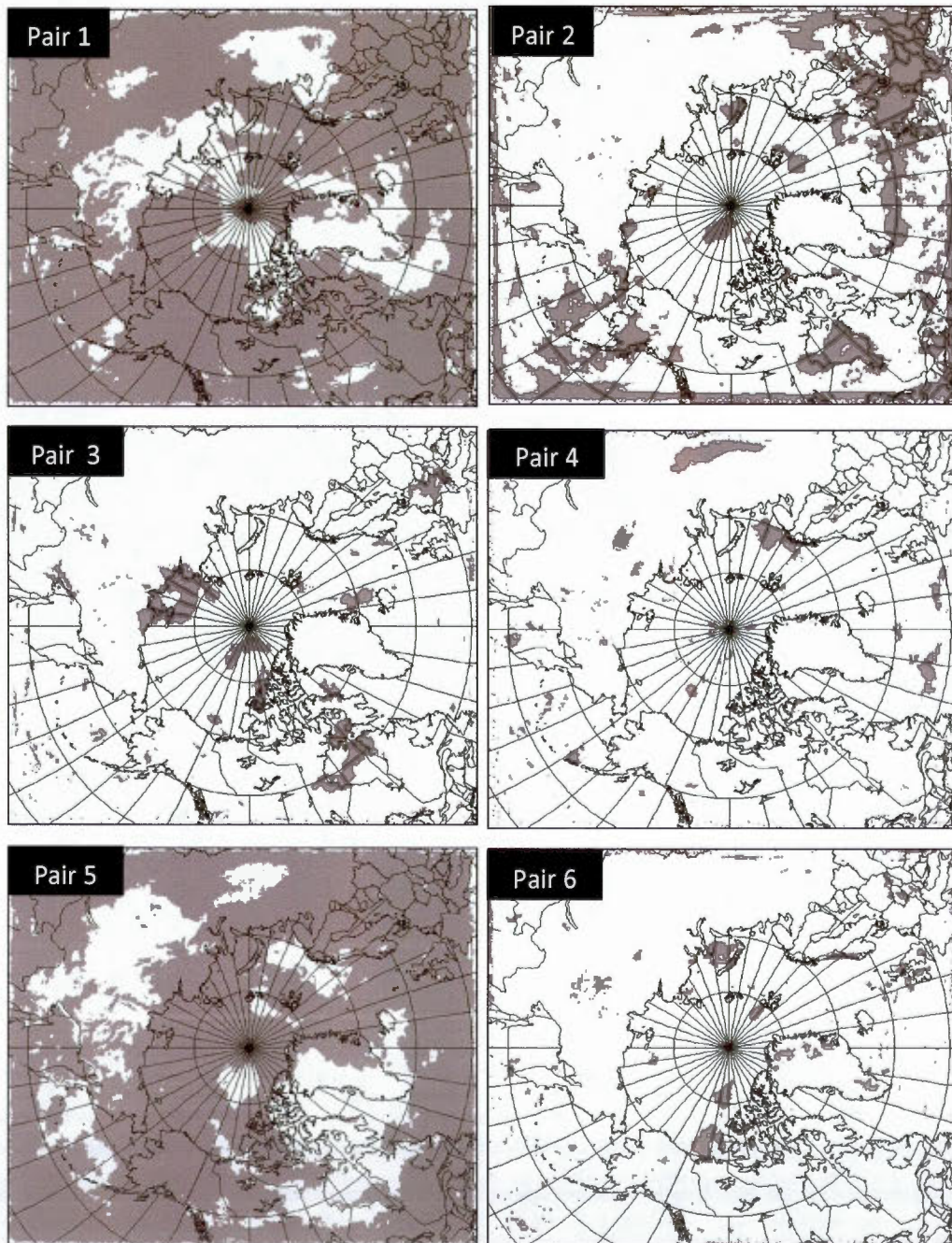


Figure D.8: Significant area for anomaly of cloud forcing at the top of the atmosphere for January 2007 for all six pairs calculated using the Student t-test. The gray areas indicate significant zone with a confidence level of 95%.

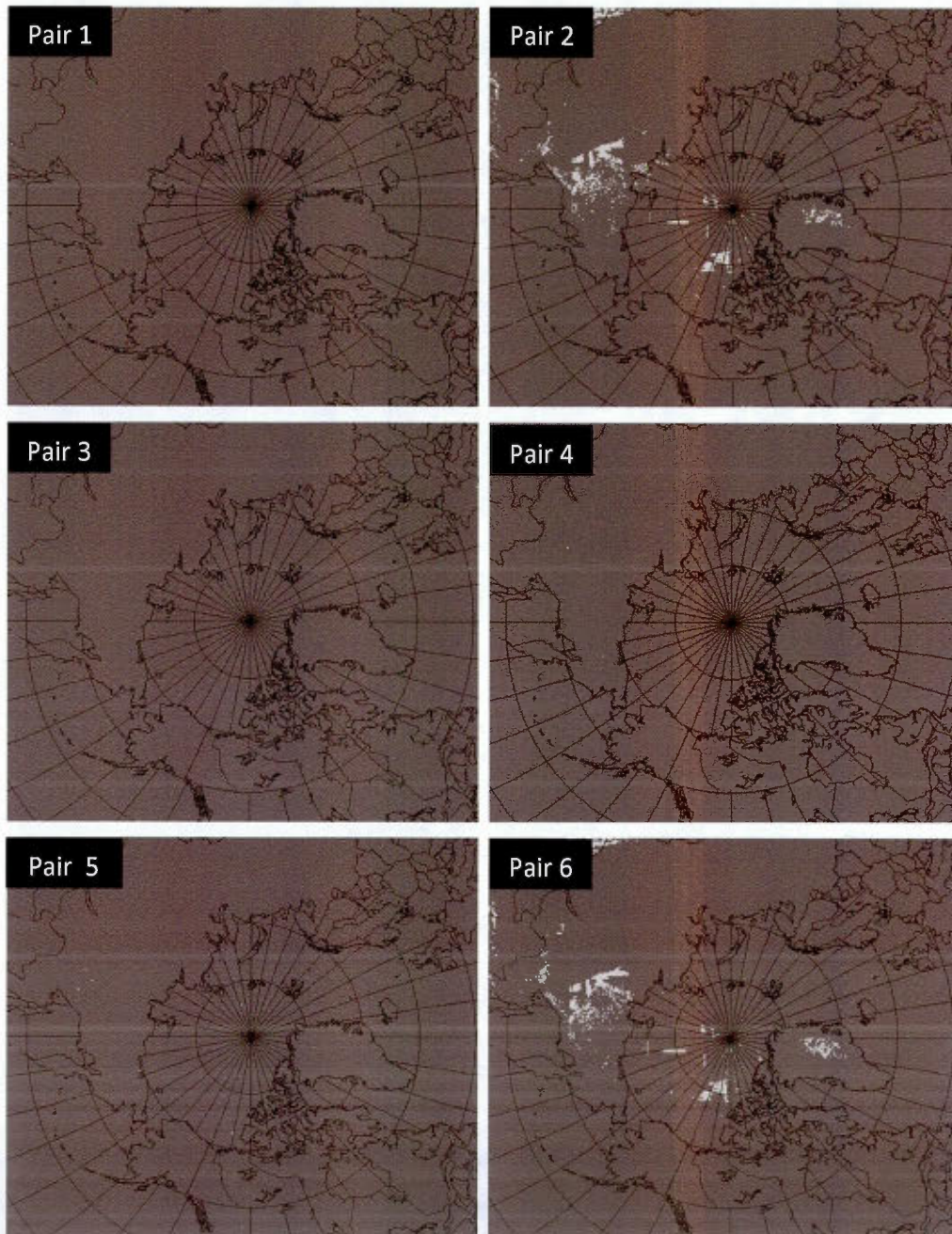


Figure D.9: Significant area for anomaly of liquid water path for January 2007 for all six pairs calculated using the Student t-test. The gray areas indicate significant zone with a confidence level of 95%.

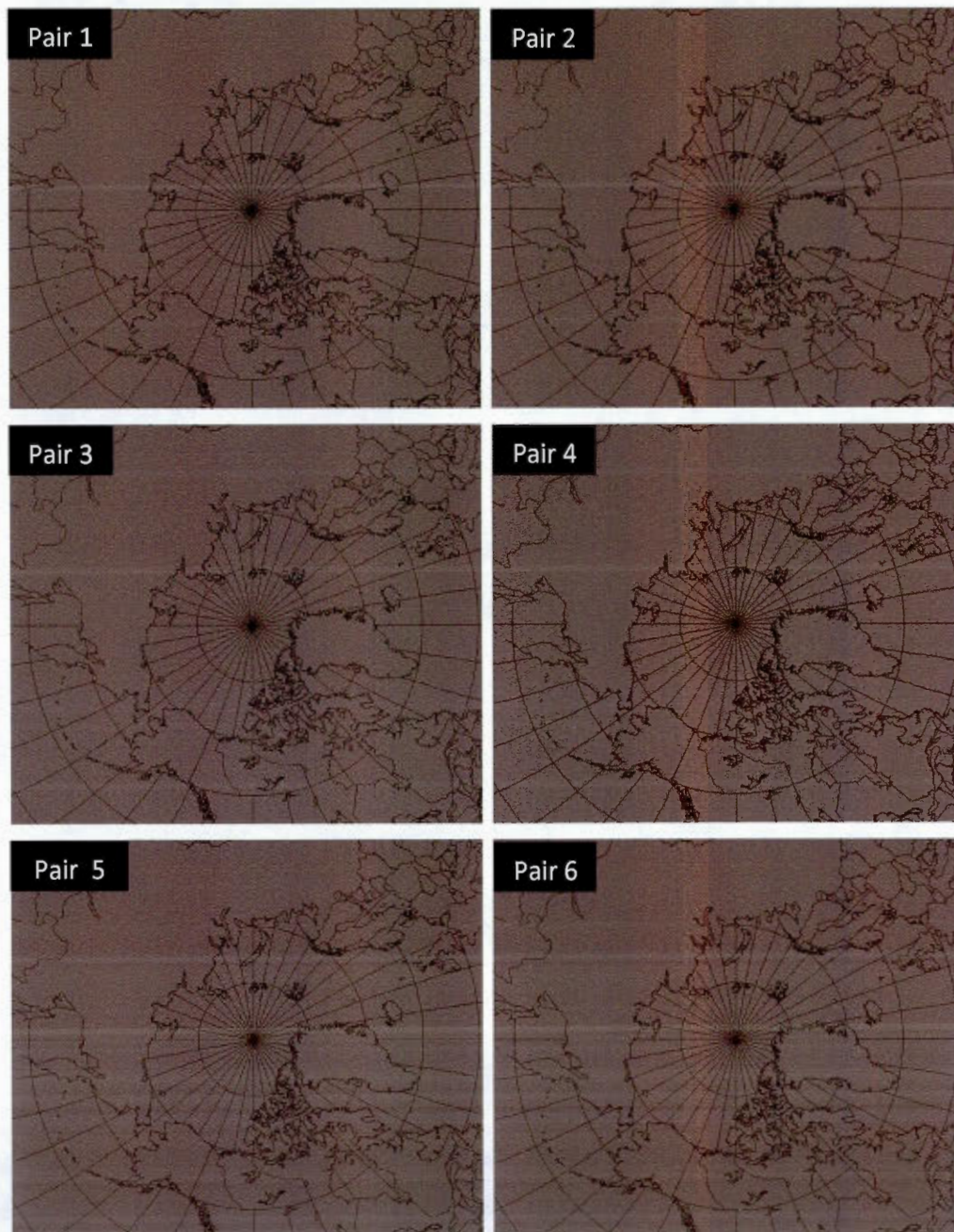


Figure D.10: Significant area for anomaly of ice water path for January 2007 for all six pairs calculated using the Student t-test. The gray areas indicate significant zone with a confidence level of 95.

RÉFÉRENCES

- Archuleta, C. M., P. J. DeMott et S. M. Kreidenweis. 2005. Ice nucleation by surrogates for atmospheric mineral dusts and mineral dust/sulfate particles at cirrus temperatures. *Atmos. Chem. Phys. Discuss.*
- Avramov, A and J. Y. Harrington. 2006. The influence of ice nucleation mode and ice vapor growth on simulatoin of Arctic mixed-phase clouds.
- Bélisle, J.-P. et J. Desrosiers. 1985. Introduction à la statistique. Gaétan Morin édition, collection Gaétan Morin
- Borys, R. D. 1989. Studies of Ice Nucleation by Arctic Aerosol on AGASP-II. *J. Atm. Chem.*
- Champigny, M. P. 2009. Etude de sensibilité du climat arctique à l'effet rétroaction déshydratation-effet de serre: étude selon deux types de circulation atmosphérique. Mémoire de maîtrise, Montréal, Université du Québec à Montréal
- Chernoff, D. I. et A. K. Bertram. 2010. Effects of sulfate coatings on the ice nucleation properties of a biological ice nucleus and several types of minerals. *J. Geophys. Res.* doi:10.1029/2010JD014254.
- Cohard, J.-M. et J.-P. Pinty. 2000a. A comprehensive two-moments warm microphysical bulk scheme. 1: Description and tests. *Quart. J Roy. Meteor. Soc.*
- Côté, J., S. Gravel, A. Méthot, A. Patoine , M. Roch et A. Staniforth. 1998. The operational CMC-MRB Global Environmental Multiscale (GEM) model. Part I: Design considerations and formulation. *Monthly Weather Review*
- Cotton, W. R., G. J. Tripoli, R. M. Rauber et E. A. Mulvihill. 1986. Numerical simulation of the effects of varying ice crystal nucleation rates and aggregation processes on orographic snowfall. *J. Climate Appl. Meteor.*
- Claquin, T., M. Schulz et Y. J. Balkanski. 1999. Modeling the mineralogy of atmospheric dust sources. *J. Geophys. Res.*
- DeMott, P. J., K. Sassen, M. R. Poellot, D. Baumgardner, D. C. Rogers, S. D. Brooks, A. J. Prenni et S. M. Kreidenweis. 2003a. African dust aerosols as atmospheric ice nuclei. *Geophys. Res. Lett.*

Demott, P. J., D. J. Cziczo, A. J. Prenni, D. M. Murphy, S. M. Kreidenweis, D. S. Thomson, R. Borys et D. C. Rogers. 2003b. Measurements of the concentration and composition of nuclei for cirrus formation. *Proc. Natl. Acad. Sci. U.S.A.*

Dorais, J. G. 2010. Évaluation de la performance de quatre schémas microphysique pour la simulation des nuages arctique en phase mixte avec le modèle GEMLAM. Mémoire de maîtrise, Montréal, Université du Québec à Montréal

Du, P., Girard, E., Bertram, A.K., Shupe, M.D., 2011. Modeling of the cloud andradiation processes observed during SHEBA. *Atmospheric Research*.

Eastwood, M. L. Ice nucleation on uncoated and coated atmosphere mineral dust particles. 2008. Mémoire de maîtrise, Vancouver, Université de British Columbia

Eastwood, M. L., S. Cremel, C. Gehrke, E. Girard et A. K. Bertram. 2008. Ice nucleation on mineral dust particles: Onset conditions, nucleation rates and contact angles. *J. Geophys. Res.*, doi:10.1029/2008JD010639.

Eastwood, M. L., S. Cremel, M. Wheeler, B. J. Murray, E. Girard et A. K. Bertram. 2009. Effect of sulphuric acid and ammonium sulfate coatings on the ice nucleation properties of kaolinite particles. *Geophys. Res. Lett.*, vol. doi:10.1029/2008GL035997.

Blanchet, J.-P. et E. Girard. 1994. Arctic greenhouse cooling. *Nature*, 383.

Girard, E. et B. Bekcic. 2005. Sensitivity of an Arctic Regional Climate Model to the horizontal resolution during winter: Implications for aerosol simulation. *Int. J. Climatol.*

Girard, E. et A. Stefanof. 2007. Assessment of the dehydration-greenhouse feedback over the Arctic during February 1990. *Int. J. Climatol.*

Girard, E., G. Dueymes et P. Du. 2013. Assessment of the Effects of Acid-Coated Ice Nuclei on the Arctic Cloud Microstructure, Atmospheric Dehydration, Radiation and Temperature during Winter. *Int. J. Climatol.*

Hurrell, J. W., J. J. Hack, D. Shea, J. M. Caron and J. Rosinski. 2008. A New Sea Surface Temperature and Sea Ice Boundary Dataset for the Community Atmosphere Model. *J. Climate*. doi: 10.1175/2008JCLI2292.1.

Hobbs, P. V. et Rangno A. L. 1985. Ice particle concentrations in clouds. *J. Atmo.Sci.*

Hoose, C.,U. Lohmann, R. Erdin et I. Tegen. 2008. The global influence of dust mineralogical composition on heterogeneous ice nucleation in mixed-phase clouds. *Environ. Res. Letts*. doi:10.1088/1748-9326/3/2/025003

Kulkarni, G., J. Fin, J. M. Comstock, X. Liu et M. Ovchinnikov. 2012. Laboratory measurements and model sensitivity studies of dust deposition ice nucleation. *Atmos. Chem. Phys. Discuss.*

Kumai, M. 1961. Snow crystals and the identification of the nuclei in the northern United States of America, *J. Meteorol.*

IPCC, 2001. *Climate Change 2001: The Scientific Basis.*

Iversen, T. 1996. Atmospheric transport pathways for the Arctic. In *Chemical Exchange Between the Atmosphere and Polar Snow, Global Environmental Change, NAO ASI series 1*, vol. 43, Wolff E, Bales RC (eds). Springer-Verlag: Berlin and Heidelberg

Li, J. et W. Barker. 2005. A radiation algorithm with correlated-K distribution. Part I: Local thermal equilibrium. *J. Atmos. Sci.*

Marcilli, C., S. Gedamke, T. Peter et B. Zobrist. 2007. Efficiency of immersion mode ice nucleation on surrogates of mineral dust. *Atmos. Chem. Phys.*, vol. 7, p. 5081–5091, doi:10.5194/acp-7- 5081-2007.

Meyers, M. P., Demott, P. J., Cotton, R. W., (1991). New primary ice-nucleation parameterization in an explicit cloud model. *J. Appl. Meteor.*

Milbrandt, J. A. et M. K. Yau. 2005. A multi-moment bulk microphysics parameterization. Part 1: Analysis of the role of the spectral shape parameter. *J. Atmos. Sci.*

Milbrandt, J. A. et M. K. Yau. 2005. A multi-moment bulk microphysics parameterization. Part II: A Proposed Three-Moment Closure and Scheme Description. *J. Atmos. Sci.*

Milbrandt, J. A. et M. K. Yau. 2006. A multi-moment bulk microphysics parameterization. Part III: Control Simulation of a Hailstorm. *J. Atmos. Sci.*

Milbrandt, J. A. et M. K. Yau. 2006. A multi-moment bulk microphysics parameterization. Part IV: Sensitivity Experiments. *J. Atmos. Sci.*

Noilhan, J. et S. Planton. 1989. A simple parameterization of land surface processes for meteorological models. *Mon. Wea. Rev.*

Pitter, R. L. et H. R. Pruppacher. 1973. A wind tunnel investigation of freezing of small water drops falling at terminal velocity in air. *Quart. J. Roy. Meteor. Soc.*

Pruppacher, H. R. et J. D. Klett. 1998. *Microphysics of Clouds and Precipitation*. Kluwer Academic

Pruppacher, H. R. 1995. A new look at homogeneous ice nucleation in supercooled water drops. *J. Atmos. Sci.*

Richardson, M. S., P. J. DeMott, S. M. Kreidenweis, D. J. Cziczo, E. J. Dunlea, J. L. Jimenez, D. S. Thomson, L. L. Ashbaugh, R. D. Borys, D. L. Westphal, G. S. Casuccio et T. L. Lersch. 2007. Measurements of heterogeneous ice nuclei in the western United States in springtime and their relation to aerosol characteristics, *J. Geophys. Res.* doi:10.1029/2006JD007500.

Rinke, A. et K. Dethloff. 2000. on the sensitivity of a regional Arctic climate model to initial and boundary conditions. *Clim. Res.*

Rinke, A, P. Marbaix et K. Dethloff. 2004. Internal variability in arctic regional climate simulations: Case study for the SHEBA year. *Clim. Res.*

Salam, A., U. Lohman, B. Crenna, G. Lesins, P. Klages, D. Rogers, R. Irani, A. MacGillivray et M. Coffin. 2006. Ice Nucleation Studies of Mineral Dust Particles with a New Continuous Flow Diffusion Chamber, *Aerosol Sci. Tech.* doi:10.1080/02786820500444853.

Shaw, G. E. 1995. The Arctic haze phenomenon. *Bulletin of the American Meteorological Society*.

Seinfeld, J. H. 1986. *Atmosphere chemistry and physics of air pollution*. John Wiley et Sons Eds., New York.

Stefanof, A. 2007. Étude 3D de la sensibilité du climat Arctique à la rétroaction déshydratation-effet de serre. Mémoire de maîtrise, Montréal, Université du Québec à Montréal.

Sullivan R. C., M. D. Petters, P. J. DeMott, S. M. Kreidenweis, H. Wex, D. Niedermeier, S. Hartmann, T. Clauss, F. Stratmann, P. Reitz, J. Schneider et B. Sierau. 2010. Irreversible loss of ice nucleation active sites in mineral dust particles caused by sulphuric acid condensation. *Atmos. Chem. Phys.*

Svensson, E., A. C. Delval, P. Hessberg, M. S. Johnson et J. B. C. Pettersson. 2009. Freezing of water droplets colliding with kaolinite particles. *Atmos. Chem. Phys.* doi:10.5194/acp-9-4295-2009

Walko, R. L., W. R. Cotton, M. P. Meyers et J. Y. Harrington. 1995. New RAMS cloud microphysics parameterization. Part 1: The single-moment scheme. *Atmos. Res.*

Wheeler, M. J. et A. K. Bertram. 2011. Deposition freezing on mineral dust particles: A case against standard classical nucleation theory with the assumption of a single contact angle. *Atmos. Chem. Phys. Discuss.* doi:10.5194/acpd-11-21171-2011.

Young, K. C. 1974. A numerical simulation of wintertime, orographic precipitation. Part I: Description of model microphysics and numerical technique. *J. Atmos. Sci.*